FACULTY
OF MATHEMATICS
AND PHYSICS
Charles University

DOCTORAL THESIS

Mgr. Xianxian Xie

Research and development of platinum-based cathode catalysts for proton exchange membrane fuel cells

Department of Surface and Plasma Science

Supervisor of the doctoral thesis: doc. Mgr. Ivan Khalakhan, Ph.D.

Study program: Physics

Study branch: F5 - Physics of Surfaces and Interfaces

Prague 2024

I declare that I carried out this doctoral thesis independently, and only with the cited sources, literature and other professional sources. It has not been used to obtain another or the same degree.

I understand that my work relates to the rights and obligations under the Act No. 121/2000 Sb., the Copyright Act, as amended, in particular the fact that the Charles University has the right to conclude a license agreement on the use of this work as a school work pursuant to Section 60 subsection 1 of the Copyright Act.

In Prague date..... signature

Acknowledgments

I am sincerely grateful to my supervisor, Dr. Ivan Khalakhan, for his invaluable guidance, unwavering patience, and support throughout my academic study. Under his mentorship, I have not only acquired profound knowledge but also learned how to organize my thoughts and represent my work. Special appreciation is extended to my pre-supervisor, prof. Iva Matolínová, whose kindness and advice during my first year of study.

Furthermore, I wish to express my heartfelt thanks to Dr. Yurii Yakovlev and Dr. Peter Kúš, who have taught me how to use basic equipment and always helped with many technical problems. In addition, I would like thanks to my colleagues who played a crucial role in the collaborative efforts of this work: Dr. Kateřina Veltruská, Dr. Michael Vorochta, Dr. Tomáš Skála, Dr. Jaroslava Nováková, Mgr. Thu Ngan Dinhová and Mr. Miquel Gamón Rodríguez. Moreover, I wish to express my sincere gratitude to Dr. Serhiy Cherevko and Dr. Valentín Briega-Martos from the Electrocatalysis group at the Helmholtz Institute Erlangen-Nürnberg for Renewable Energy (Erlangen, Germany) for their invaluable contribution in conducting the SFC-ICP-MS measurements.

Lastly, I would like to thank my colleagues in the Department of Surface and Plasma, where I found a welcoming community of colleagues. Their warm acceptance has enhanced my experience and fostered a collaborative environment that has been instrumental in the progress of my research.

Title: Research and development of platinum-based cathode catalysts for proton exchange membrane fuel cells

Author: Mgr. Xianxian Xie

Department: Department of Surface and Plasma Science, Faculty of Mathematics and Physics, Charles University

Supervisor: doc. Mgr. Ivan Khalakhan, Ph.D., Department of Surface and Plasma Science, Faculty of Mathematics and Physics, Charles University

Abstract

Widespread adoption of advanced energy technologies, such as proton-exchange membrane fuel cells (PEMFCs), relies on the development of efficient and durable catalysts for oxygen reduction reaction (ORR). Given its unique properties, platinum has been the primary choice for meeting activity demands, either in its pure form or as various Pt-based alloys. The challenge yet persists with catalyst degradation in the hostile environment of the PEMFC cathode. The thesis aims to explore efficient and durable Pt-based ORR catalysts prepared by the magnetron sputtering technique.

In the first chapter, Pt–Au alloys with various compositions (5, 10, 20 at.% of Au) were systematically studied to understand their composition-activity-stability relationship. It was found that $Pt_{90}Au_{10}$ exhibits the most optimal alloying, retaining the activity of Pt while effectively suppressing Pt dissolution. The stability of Pt–Au alloys was further evaluated under different simulated PEMFC operating conditions, demonstrating their higher stability compared to monometallic Pt catalyst.

In the second chapter, the composition-activity-stability relationship of ternary PtNi–Au alloys with various compositions (3, 7, 15 at.% of Au, Pt:Ni = 50:50) was investigated. It was revealed that while Au incorporation negatively impacts activity, it enhances stability. Among tested catalysts, PtNi–Au alloy with 15 at.% of gold showed the highest stability and still higher activity than monometallic Pt.

The third chapter explores the synthesis of highly porous Pt–C catalyst by electrochemical dealloying of Pt–C–CeO_x ternary compound. Pt–C catalysts exhibited significantly increased electrochemically active surface area (ECSA), enhanced ORR activity, and improved stability compared to monometallic Pt.

Keywords: PEMFCs, ORR, Pt-based catalyst, stability, activity

Preface

This doctoral thesis presents the experimental research at the Department of Surface and Plasma Science, Charles University done from 2018 to 2023. The work aims to develop new efficient and at the same time durable cathode catalysts for PEMFCs.

The main parts of this doctoral thesis are based on results published in the following articles, as well as yet unpublished results:

1. **Xie, X**.; Briega-Martos, V.; Farris, R.; Dopita, M.; Vorokhta, M.; Skála, T.; Matolínová, I.; Neyman, K. M.; Cherevko, S.; Khalakhan, I., Optimal Pt–Au Alloying for Efficient and Stable Oxygen Reduction Reaction Catalysts. *ACS Appl. Mater. Interfaces*, 2023, 15 (1), 1192-1200.

2. **Xie, X.;** Khalakhan, I.; Vorokhta, M.; Yakovlev, Y.; Dinhová, T. N.; Nováková, J.; Kúš, P.; Dopita, M.; Veltruská, K.; Matolínová, I., A Facile Way for Acquisition of a Nanoporous Pt–C Catalyst for Oxygen Reduction Reaction. *Adv. Mater. Interfaces*, 2021, 8 (12), 2100122.

Contents

1. Introduction

Due to continuous growth in global energy consumption, the demand for energy sources is continuously increasing. Most of them are still based on burning fossil fuels, which is on the other hand the main factor for air pollution and climate change. The former is responsible for a variety of human illnesses, such as stroke, lung cancer, pneumonia, and neonatal disorders. The latter causes global warming, which leads to more frequent heat waves, droughts and wildfires, rising sea levels, and melting glaciers. Moreover, due to global warming, one-third of the animal and plant species will likely become extinct by 2050 [1]. With regard to those issues, as well as the expected depletion of fossil fuels, in the last several decades, humanity has stimulated an intense transition from fossil fuel to a renewable-based economy in many countries. Particularly, the EU has pledged to achieve climate neutrality by 2050 and cut net greenhouse gas emissions in the EU by at least 55 % by 2030, compared to 1990 levels [2].

The production of energy from renewable energy sources, such as solar cells, hydropower, and wind power stations, faces a significant challenge, which is unstable in time energy production. During periods of shortage, these sources must be supplemented by other energy sources, which are nowadays mostly of a nuclear and fossil nature. On the contrary, during surplus periods, there is not enough demand for excess energy. Electrochemical energy conversion technologies like fuel cells and water electrolyzers are considered to smooth out the variability of wind or solar electricity production in synergy with more established batteries. The excess electric energy generated by renewable sources can be used in an electrolyzer to split water and store the energy in the form of hydrogen, which can be stored. This hydrogen can then be used as fuel in fuel cells to generate energy during periods of shortage (see Fig. 1.1). The so-called “hydrogen cycle” plays a pivotal role in the transition towards zero emissions. Indeed, according to the aforementioned Green Deal, hydrogen is seen as the main future energy carrier.

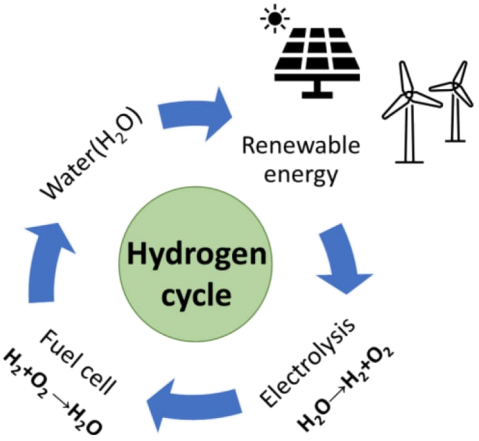

Fig. 1.1. *Schematic illustration of hydrogen cycle.*

While renewable energy sources are already well-established and successfully functioning worldwide, state-of-the-art technologies like fuel cells and water electrolyzers have just started reaching commercialization not so long time ago. There are several types of fuel cells available for providing electric power, including alkaline fuel cells (AFC), solid oxide fuel cells (SOFC), microbial fuel cells (MFC), and hydrogen-fueled proton exchange membrane fuel cells (PEMFCs). Among those options, PEMFCs stand out as the most promising and versatile choice due to their environmental sustainability, low operation temperatures, high energy density, and energy conversion efficiency [3]. Moreover, hydrogen is the most abundant element in the universe. It can be considered as the predominant energy resource to replace fossil fuel and other renewable energy resources in the future. Due to those advantages, PEMFCs show a promising potential to be employed in small fleets of passenger cars, trucks, and trains, as well as stationary power stations [4].

1.1. Proton-exchange membrane fuel cell

A proton exchange membrane fuel cell (PEMFC) is an electrochemical setup that converts the chemical energy of a fuel (hydrogen) and oxidizer (oxygen or air) into electrical energy. The simplified schematic illustration of PEMFC is depicted in Fig. 1.2. The core of such a fuel cell is a so-called membrane electrode assembly (MEA), which consists of an anode electrode, polymer electrolyte membrane (PEM), and cathode electrode. The PEM is a special electrically insulating but conducive to protons polymer membrane (typically Nafion). Both anode and cathode electrodes consist of a mixture of Pt nanoparticles, polymer, and carbon black, which can be either

deposited on a microporous gas diffusion electrode (GDL) or directly onto PEM. The carbon black facilitates electron movement within the electrode, providing electrical conductivity. The polymer allows the proton transfer within the electrode, providing the proton conductivity. The GDL is a carbon-based material with a highly porous structure, contributing to the uniform distribution of reactant gases and the removal of water formed at the cathode side. The MEA is further sandwiched between two bipolar plates, which are directly connected to the supply of reactants.

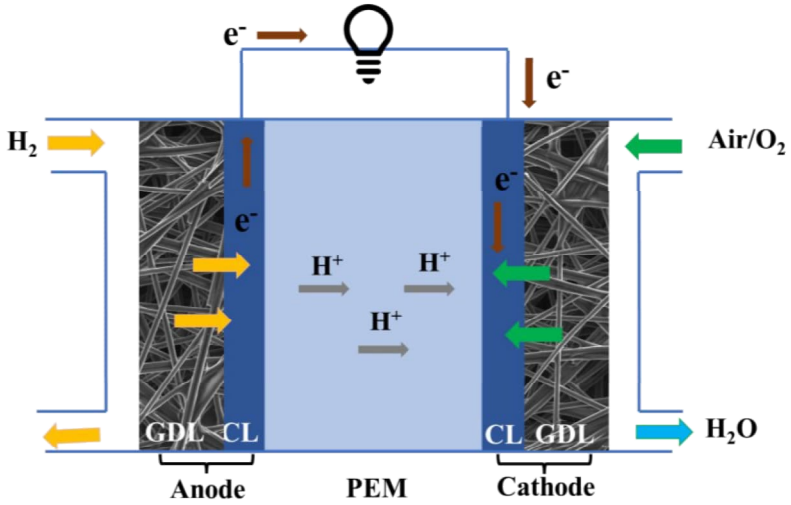

Fig. 1.2. *A simplified scheme of a PEMFC.*

The main electrochemical reactions running inside a PEMFC are hydrogen oxidation reaction (HOR) and oxygen reduction reaction (ORR). At the anode side, the catalyst facilitates HOR, breaking down hydrogen molecules into electrons and protons (H^+). The proton then migrates through the PEM, while electrons transfer through the external circuit to the cathode side, producing electric power. On the cathode side, the ORR occurs, involving the recombination of the protons and electrons, which immigrate from the anode side with the oxygen that is supplied to the cathode. The overall reaction, as well as half-cell reactions occurring on the anode and cathode sides at room temperature, are provided below:

$$(1) \quad H_2 = 2H^+ + 2e^- \qquad E°_{anode} = 0\ V$$

$$(2) \quad O_2 + 4H^+ + 4e^- = 2H_2O \qquad E°_{cathode} = 1.23\ V$$

$$(3) \quad 2H_2 + O_2 = 2H_2O \qquad E°_{cell} = 1.23\ V$$

It is worth noting that although the theoretical potential of a single PEMFC is 1.23 V, the actual voltage is within approximately 0.6 - 1 V. This deviation from the theoretical potential is caused by various factors, including the activation overpotential of the reactions (mainly ORR), the cell ohmic resistance, and mass transport limitations.

Nevertheless, the requirement of power output is diverse in the different applications. For example, portable electronic devices like laptops and smartphones require from a few watts to ten watts [4]. The power output of automotive applications typically ranges from tens to hundreds of kilowatts [5]. The residential and industrial power supply requires even more power. In order to meet the requirements of specific applications, multiple PEMFCs are assembled into the so-called stack, which scales up the power output and voltage. The schematic illustration of the PEMFC stack is shown in Fig. 1.3.

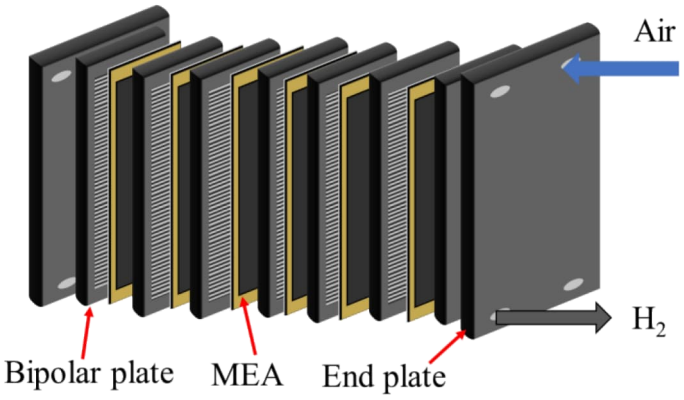

Fig. 1.3. *A simplified scheme of a PEMFC stack.*

1.2. Current status and challenges of PEMFCs

Nowadays, PEMFCs are undergoing intensive development and are expected to enter the global market in the near future. Thanks to their modular design, fuel cells can be applied in various applications ranging from large stationary power plants to compact portable power systems as well as transportation [6]. The versatile stationary fuel cell systems, spanning a power range from a few kilowatts to multiple megawatts, find applications in both backup power for vital infrastructure and in providing electricity and heat for commercial and residential use through combined heat and power (CHP) configuration [7]. Among the notable examples are FCgen®-H2PM and FCwaveTM by Ballard, offering power capacities of 1 kW-60 kW and 200 kW-1.2

MW, respectively, and 200 kW VLS II fuel cell stack by Horizon fuel cell technologies [8, 9]. In contrast, portable fuel cells are compact and lightweight power generation devices with power output in the range of 1 to 200 W that are used in various applications like military applications, Auxiliary Power Units, small and large personal electronics, etc. In recent years, many fuel cell companies, such as SFC Energy AG, Toshiba, and Sanyo, have started focusing on portable fuel cells [10]. More importantly, PEMFCs are receiving significant attention in transportation, particularly in applications such as fuel-cell buses, cars, heavy-duty trucks, ships, and trains [11, 12]. In 2014, Toyota initiated the commercial production of the Mirai, the first commercially produced hydrogen-powered fuel cell vehicle (FCV) [13]. Since then, several FCVs have been available, such as the Hyundai Nexo, Honda Clarity, Hyundai ix35, and Mercedes-Benz GLC F-CELL. Beyond FCVs, the world's 1st hydrogen-power passenger train, Coradia iLint, was launched in Germany by Alstom company in 2018 [14].

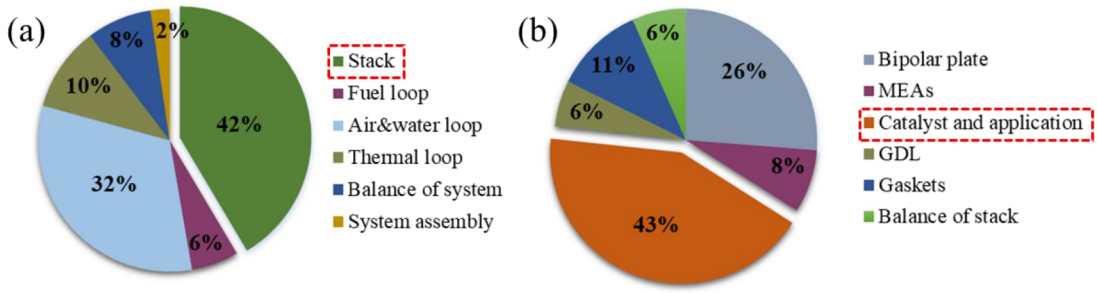

Fig. 1.4. *Cost of 80 kW_{net} PEM Fuel cell system based on 500 000 units/year for 2018: (a) system cost; (b) stack cost distribution. Data from reference [15].*

However, commercializing such fuel cells encounters significant obstacles due to various shortcomings, including hydrogen production, hydrogen infrastructure, the relatively high cost of PEMFCs, etc. Among them, the high cost of PEMFCs is one of the primary challenges that needs to be addressed. Fig. 1.4 illustrates the cost of an 80 kW_{net} PEMFC system, with a production volume of 500,000 units per year, and a breakdown of its stack cost. It can be seen in Fig. 1.4a that the FC stack cost accounts for ca. 42 % of the total system cost, indicating the importance of reducing stack costs to achieve overall fuel cell system cost targets ($ 40/kWnet, DOE 2025 target) [15]. Moreover, Fig. 1.4b reveals that the catalyst and its application reach up to ca. 43 % of the total cost of the FC stack. This cost prominence is attributed to the expensive

catalyst material on FC electrodes and its substantial loading requirement, especially on the cathode side.

Since the 1960s, platinum has been the only catalyst that more or less meets the requirements for the activity and stability of PEMFC. The price of platinum has increased significantly over the years, reaching eight times higher compared to its value in the 1960s, as shown in Fig. 1.5. Moreover, despite a global production of 78 million vehicles (electricity, hydrogen, petrol, diesel, and others) in 2020, there are only about 35 000 hydrogen-powered FCVs sold [16]. The state-of-the-art Pt/C catalysts used in FCs nowadays require a Pt-specific-stack power density of about $0.3 g_{Pt} \cdot kW^{-1}$ in an automotive fuel cell system to attain the desired operational lifetime without a significant compromise in efficiency [17]. Considering the possibility of let's say ten million FCVs production with a given 70 kW fuel cell stack, it would require 210 tons of platinum per year, which is even higher than the annual platinum mining rate of approximately 190 tons in 2022 [18]. Therefore, due to the low abundance of platinum and the projected escalating demand resulting from widespread PEMFC applications, the price of platinum is expected to increase steeply resulting in an increase in the fuel cells cost.

Based on the above, reducing the Pt loading on fuel cell electrodes is the primary approach for reducing the FC stack cost. The U.S. Department of Energy (DOE) has set the Pt loading target in both the anode and cathode sides to be lower than $0.1\ mg_{Pt} \cdot cm^{-2}$ by 2025 to enhance the economic viability and sustainability of PEMFCs [19]. In recent years, Pt loading on the anode has been effectively reduced to $0.05\ mg_{Pt} \cdot cm^{-2}$ without compromising PEMFC performance requirements [20]. However, due to the sluggish kinetics of the ORR, the cathode side generally requires approximately ten times higher Pt loading than the anode [21]. The current commercial cathode catalyst platinum loading ranges from 0.2 to $0.5\ mg_{Pt} \cdot cm^{-2}$ to meet the mass activity (MA) target of $0.44\ A \cdot g^{-1}$ at 0.9 V, which is still higher than the DOE target [22, 23]. However, decreasing platinum loading below $0.2\ mg_{Pt} \cdot cm^{-2}$ results in insufficient performance for long-term application [24]. For example, Gazdzicki et al. observed significant performance limitations of MEA when cathode Pt loading below $0.2\ mg_{Pt} \cdot cm^{-2}$ and strong voltage drops during long-term operation when cathode Pt loading below $0.4\ mg_{Pt} \cdot cm^{-2}$ [25]. Based on the above, decreasing Pt loading at the cathode is thus still an urgent issue.

Fig. 1.5. *The evolution of platinum price from 1970 to 2022.*

As was hinted above, the decrease in Pt loading to achieve the Department of Energy (DOE) cost target at the same time should not compromise the long-term performance of PEMFCs. The approach to enhancing durability involves identifying the variables that influence the lifespan of a PEMFC and creating strategies to mitigate any adverse consequences. In PEMFC, reliability and durability are impacted by the degradation mechanisms of fuel cell components such as the catalyst layer, PEM, gas diffusion layer, bipolar plates, etc. However, the longevity of a fuel cell is intrinsically linked to the deterioration processes taking place at the electrodes, and thus catalyst degradation itself significantly influences the overall durability of fuel cells. This is especially valid for the cathode side, where catalyst/support assemblies are subjected to a corrosive environment experiencing low pH levels and relatively high potentials ranging from 0.6 to even 1.5 V_{RHE} [26]. These operational conditions are further compounded by the intermittent and cyclical nature of PEMFC operations, particularly in the context of automotive applications. This makes the stability of PEMFCs another challenge that needs to be addressed in the race to speed up the widespread commercialization of PEMFCs.

The same as for cost-efficiency, the U.S. DOE has established durability targets for the year 2050 regarding different applications, including 5,000 h for portable devices, 8,000 h (equivalent to about 250,000 km) for FCVs, and 25,000 h for fuel cell buses (FCBs) with permissible < 40 % loss of mass activity [6]. However, it is worth noting that most achievements nowadays still fall short of the previously mentioned benchmarks. The durability of fuel cells may thus present an even more substantial hurdle than its cost-effectiveness, particularly within the automotive sector.

1.3. Catalysts for ORR

In order to increase the cost-efficiency and stability of PEMFCs, it is necessary to take a closer look at the ORR reaction mechanism running on the cathode. The ORR mainly includes two pathways, each containing a few discrete steps. One is a more efficient direct or four-electron pathway. Another is the less efficient indirect or two-electron pathway. In the direct ORR pathway, oxygen molecules (O_2) are directly reduced to water (H_2O) through a four-electron transfer process. The reaction under standard conditions is as follows:

$$(4) \quad O_2 + 4H^+ + 4e^- = 2H_2O \qquad E^o = 1.23\ V$$

The indirect ORR pathway consists of two steps with the formation of hydrogen peroxide (H_2O_2) intermediate species:

$$(5) \quad O_2 + 2H^+ + 2e^- = H_2O_2 \qquad E^o = 0.7\ V$$

$$(6) \quad H_2O_2 + 2H^+ + 2e^- = 2H_2O \qquad E^o = 1.76\ V$$

The direct four-electron pathway is more desirable for ORR. However, the two-electron pathway or the mixture of four- and two-electron pathways is easier to occur on the surface of electrodes [27]. The reason for this is that the O-O bond dissociation energy (~494 $kJ \cdot mol^{-1}$) for oxygen molecules is higher than the formation energy (~146 $kJ \cdot mol^{-1}$) of H_2O_2 or HO_2^- during two electrons pathway [28]. Consequently, the indirect pathway forms a by-product of H_2O_2, leading to low energy conversion efficiency and producing reactive intermediates that can further convert to harmful free radical species (OOH, OH, O) [29, 30].

Therefore, in order to enhance ORR kinetics, the catalyst with appropriate oxygen adsorption energy with reaction intermediates (O, OH) can encourage the desired four-electron pathway. In addition, these adsorption energies can serve as predictive indicators for the ORR activity of the catalyst. For example, the adsorption of oxygen and formation of the HOO* group (* denoted as absorbed on the catalyst sites) must occur on the surface, which requires the catalyst to bind oxygen strongly [21]. On the other hand, part of the process involves the reduction of the HO* group, which requires a weak bond with this group [21]. However, the catalyst to which

HOO* strongly binds also exhibits strong binding to HO* and to oxygen. If oxygen binds too strongly, the surface will be filled with adsorbed OH groups. Thus, both too-strong and too-weak bonding energy will cause low catalytic activity.

The theoretically predicted relationship between ORR activity and the binding energy of O* and OH* to the catalyst, together with the one for selected elements, is illustrated in Figs. 1.6a and b, respectively. It can be observed that those two binding energies are linearly correlated for metal surfaces. Such plots, known as the volcano plot, are based on the Sabatier principle and are commonly used to predict the optimal binding energy of catalysts with reaction intermediates for the highest ORR activity. For instance, in Fig. 1.6a, elements on the left side of the peak have stronger adsorption energy with O*, and those on the right side have weaker adsorption energy. Platinum is near the top of the peak, representing the most suitable binding energy with O*, among other elements, and thus it has higher ORR activity compared to other elements on the graph. However, according to the theoretically predicted volcano plot, we can still increase the ORR activity by decreasing its oxygen binding energy by about 0.2 eV with respect to that for platinum [21]. Therefore, appropriate O* and OH* binding energy on the catalyst surface is a key factor for the ORR activity enhancement.

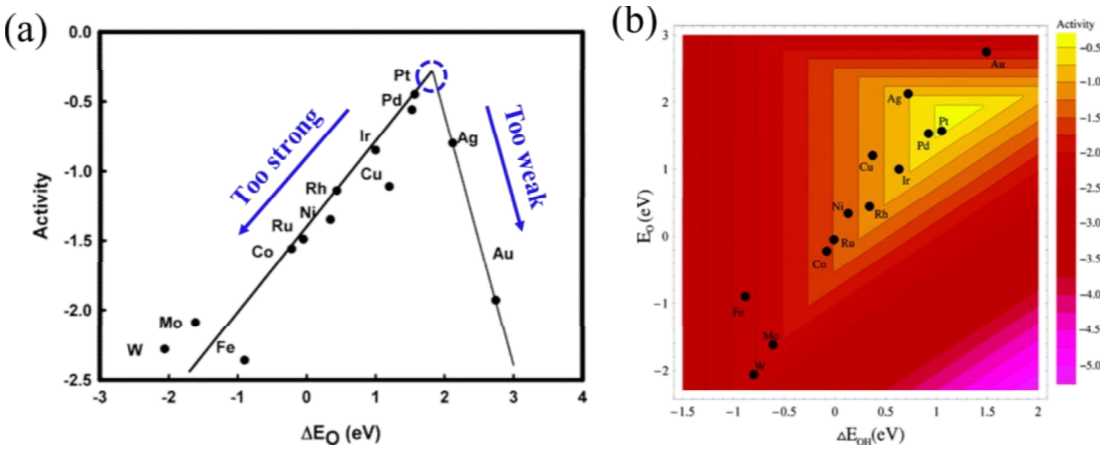

Fig. 1.6. *(a) ORR activity as a function of the oxygen binding energy; (b) ORR activity as a function of both O and OH binding energy. Adopted from [21].*

Many studies have been carried out to find suitable binding energy (ΔE_O and E_{OH}) by modifying platinum, including structural control [31], particle size modulation [32], doping [33], and the synergistic combinations of multiple methods [34]. Among other methods, introducing foreign elements into Pt is one of the most promising ways

to enhance the ORR activity of Pt. Nørskov and coworkers introduced a d-band model that elucidates the primary mechanism behind the enhancement of Pt ORR activity [35]. It states that the d-band center (energy level of the d orbitals) of the platinum surface relative to the Fermi level is inversely related to the strength of the binding energy between the metal and adsorbates (such as O*, OH*, etc.). In other words, the lower d-band center results in weaker binding energy, leading to higher ORR activity and vice versa the higher d-band center results in stronger binding energy and, in turn, lower ORR activity. The position of the d-band can be adjusted by its alloying with other elements, as shown in Figs. 1.7a and b and thus the ORR activity of platinum can be improved.

The d-band position is governed by electronic and geometrical modifications of platinum caused by alloying. For Pt-based bimetallic catalysts, the electron from the foreign element can be either donated to or withdrawn from the d-state of Pt, leading to a change in the Fermi level and corresponding downshift or upshift of the d-band center of Pt, respectively. The geometrical effect, in turn, is caused by the smaller or bigger atomic radius of the foreign atoms, which exert compressive or tensile strain on the Pt lattice, contributing to the downshift or upshift of the d-band center of Pt, respectively [36]. These combined electronic and geometrical synergistic effects play a pivotal role in influencing the catalytic properties of bimetallic catalysts.

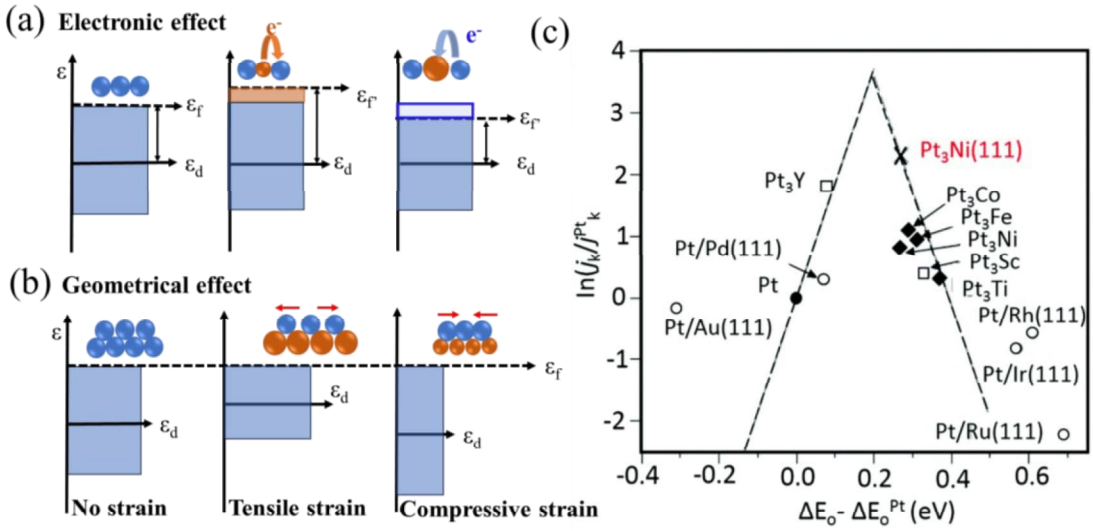

Fig. 1.7. *Schematic visualization of d-band shift caused by (a) electronic effect; (b) geometrical effect in bimetallic catalyst; (c) The experimental kinetic current density for Pt alloys as a function of oxygen adsorption energy. Adopted from [37].*

Fig. 1.7c presents the ORR activity expressed in measured kinetic current density of Pt-based alloy as a function of theoretically calculated oxygen adsorption energy (data are shown relative to pure platinum). It reveals that the Pt_3M (Ni, Fe, Co, Y, Sc, Ti) bimetallic alloys show lower oxygen binding energies and thus higher ORR activity than monometallic Pt. It is also worth mentioning that, at the same time, applying cheaper and more abundant alloying elements lowers the overall cost of the ORR catalyst. To date, various Pt-based bimetallic systems have been developed, which showed higher ORR activity than platinum and even exceeded the DOE target of 0.44 $A \cdot g^{-1}$ at 0.9 V_{RHE}. For example, Stamenkovic et al. reported that the Pt_3Ni (111) surface facet exhibited 10-fold higher ORR activity than Pt (111) [38]. Xie et al. synthesized the face-centered tetragonal Pt-Co core over the Pt shell, which exhibits 29.5 times higher specific activity than commercial Pt/C catalysts [39]. Multiple highly active Pt-based catalysts in the form of nanosphere [40], nanocube [41], nanowire [42], nanorods [43], nanocage [44], and nanoplates [45] have also been reported.

Nevertheless, despite many advantages and reaching performance targets, such alloys were found to be more prone to degradation in comparison to monometallic platinum due to the non-noble metal leaching. The long-term stability of Pt-based catalysts has become the most important challenge to be addressed.

1.4. Catalyst stability

To date, various degradation mechanisms of the benchmark Pt/C nanoparticle catalysts at the cathode side of PEMFCs have been identified. There are two main types of degradation mechanisms: primary and secondary, as shown in Fig. 1.8. The primary ones include the corrosion of the carbon support and platinum dissolution.

Although carbon as catalyst support is relatively stable, it is thermodynamically unstable and undergoes electrochemical oxidation with rising potential in real operation.

（7） $C + 2H_2O = CO_2 + 4H^+ + 4e^-$ *(0.207 V, 25 °C)*

（8） $C + 2H_2O = CO + 2H^+ + 2e^-$ *(0.518 V, 25 °C)*

From equations 7-8, carbon corrosion can theoretically occur when the potential is higher than 0.207 V_{RHE} [46]. In real PEMFC applications, the rate of carbon corrosion can be influenced by the temperature, potential, and time of operation. Makharia et al. found that the carbon corrosion rate can be accelerated at a potential

above 1 V_{RHE} by about one order of magnitude for every 0.1 V [47]. For example, during the start-up and shut-down processes, which are unavoidable in PEMFC operation, potential jumps up to even 1.5 V_{RHE} can occur on the cathode side. This can significantly increase carbon corrosion [48]. Moreover, carbon corrosion triggers secondary degradation mechanisms. It weakens the interaction between Pt particles and carbon, which may result in complete detachment of Pt catalyst particles or their migration on the carbon support with subsequent agglomeration (coalescence) into larger particles as shown in Fig. 1.8. This causes a decrease in electrochemically active surface area (ECSA) of platinum and corresponding PEMFC performance loss.

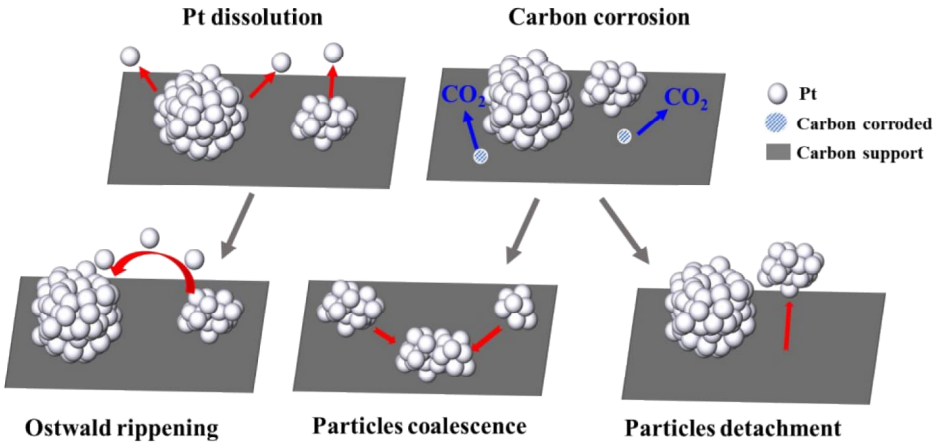

Fig. 1.8. *Simplified illustration of Pt/C degradation mechanisms in fuel cells.*

Platinum dissolution represents another primary mechanism of degradation for ORR catalysts. Based on the Pt-water Pourbaix diagram [49], Pt is thermodynamically unstable in an acidic environment and elevated potentials which are typical for a PEMFC cathode environment. Platinum atoms on the surface of the catalyst can be oxidized at potentials above 0.85 V_{RHE} and form soluble $Pt^{\delta+}$ ions according to equations 9-12.

(9) $Pt + H_2O = PtO + 2H^+ + 2e^-$ $\quad E^0 = 0.98\ V - 0.591\ pH$

(10) $PtO + H_2O = PtO_2 + 2H^+ + 2e^-$ $\quad E^0 = 1.045\ V - 0.0591\ pH$

(11) $Pt = Pt^{2+} + 2e^-$ $\quad E^0 = 1.188\ V + 0.0295\ log(Pt^{2+})$

(12) $Pt^{2+} + 2H_2O = PtO_2 + 4H^+ + 2e^-$ $E^0 = 0.837\ V - 0.1182\ pH - 0.0295\ log(Pt^{2+})$

Another Pt dissolution mechanism is explained by the so-called place-exchange mechanism. During oxidation at higher potentials (above 1.15 V_{RHE}) absorbed oxygen atoms can penetrate the Pt lattice, forming bulk Pt-oxide [50]. Those oxygen atoms occupy the lattice site of the Pt crystal structure and displace Pt atoms on the surface sites, leading to the break of the Pt-Pt bond [51, 52]. Thus, during the reduction process, massive Pt dissolution occurs [53].

Some of these dissolved Pt ions can migrate to the polymer membrane and redeposit there, blocking transport pathways for ions [54], and some can redeposit back on the catalyst. Due to thermodynamic and surface energy considerations, Pt atoms have a tendency to dissolve from smaller Pt nanoparticles and redeposit onto larger Pt nanoparticles. This leads to an increase in the size of larger Pt nanoparticles while the smaller ones continue to dissolve unless they disappear [55-57]. This effect is called Ostwald ripening [26]. Both Ostwald ripening and platinum accumulation in the ionomer lead to a decrease in the platinum catalyst ECSA.

The aforementioned degradation mechanisms are multifaceted processes impacted by various parameters. Complexity is further given by the fact that all degradation phenomena occur simultaneously. Additionally, the degradation of Pt-based alloys discussed in the previous chapter is an even more complex process given by the preferential dissolution of non-noble metals, which can further impact all the described degradation mechanisms.

To study degradation processes so-called accelerated degradation tests (ADTs) were designed to accurately simulate and replicate the degradation conditions experienced by cathode catalysts inside a real PEMFC device and obtain reliable information about their degradation. ADTs can be performed in an electrochemical cell and offer the advantage of shortening the study duration and reducing experiment costs, as they eliminate the need to employ expensive materials in real fuel cell devices. Typically, ADT includes multiple potential cycles from low to different high upper potentials [58]

Intensive studies have been conducted to develop corresponding mitigation strategies. To overcome the carbon corrosion issue, carbon materials with more graphite components showed improved corrosion resistance capability [59-61]. Li et al. prepared Pt on reduced graphene oxide well-mixed with carbon black showed less than 5 % ECSA loss, much lower than commercial Pt/C catalyst with almost 50 % ECSA loss after the durability test [60]. Furthermore, the graphitized carbon with

structure control, such as nanotube [62], nanocage [63], and nanofibre [64], restrict the mobility of Pt nanoparticles by strength the adhesion between Pt particles and support, resulting in higher electrochemical stability toward carbon corrosion.

Nevertheless, an increasing number of studies into the degradation mechanisms of ORR catalysts have emphasized the utmost importance of mitigating Pt dissolution as the primary mechanism in preventing catalyst deterioration. To suppress Pt dissolution, several strategies were proposed, such as shape control, protective layer coating, and alloying with other elements [65-67]. Among them, alloying has been identified to be favorable to suppressing Pt dissolution. It's worth noting that, in contrast to the previous case to enhance cost-efficiency through Pt alloying, the selection of foreign elements to improve platinum stability is generally limited to noble metals. For instance, a general strategy to stabilize the Pt catalysts by incorporation of a small amount of Rh was also proposed. An et al. showed that PtRh alloy catalyst forms a Pt-rich surface at the initial stage of the accelerated degradation test by a "self-healing" effect and then withstands 90,000 ADT cycles with only a 12 % decrease in mass activity [68]. It was found that the degradation occurs mainly because of Pt atom diffusion during dynamic potential cycling, and Rh suppresses this diffusion. Lu et al. also reported PtPd nanorods that showed only 5.8 % ECSA loss in comparison to commercial Pt/C catalysts with 40 % ECSA loss [69]. Gold has been demonstrated as one of the most promising ones to suppress Pt dissolution so far due to its chemical inertness. For example, a nanoparticle catalyst consisting of an Au core surrounded by a 1 nm thick mixed Pt–Au shell with a Pt-rich surface exhibited 30 times greater durability than Pt/C [70]. Zhang et al. showed no obvious performance degradation after 30,000 ADT cycles in a case of Pt nanoparticles decorated with Au clusters [71]. The addition of noble metals was also reported to have an impact on stabilizing Pt-based bimetallic alloys. For example, Strasser et al. reported that ternary Pt–Rh–Ni catalyst showed significantly improved stability in comparison to bimetallic Pt–Ni catalyst [72]. Liu et al. prepared a Pt-Ni-Au/C catalyst that showed only 16.8 % mass activity (MA) loss higher than Pt/C with 59.1 % mass activity loss [73]. Wang et al. reported Pt-Au-Cu/C catalyst presented only 7.5 % mass activity loss, superior to Pt/C with 49 % loss after 3,000 cycles [74].

2. Experimental

2.1. Materials

Different materials for sample preparation and testing have been used in this thesis.

Magnetron sputtering targets:

- Cerium dioxide (CeO_2, Kurt J. Lesker, 99.99 %, 4.00" Dia. × 0.125" thickness)
- Platinum (Pt, Safina, 99.99 %, 4.00" Dia. × 0.250" thickness, and 2.00" Dia × 0.125" thickness)
- Carbon (C, Kurt J. Lesker, 99.99 %, 4.00" Dia. × 0.250" thickness)
- Gold (Au, Kurt J. Lesker, 99.99 %, 2.00" Dia × 0.250" thickness)
- Nickel (Ni, Kurt J. Lesker, 99.99 %, 2.00" Dia × 0.250" thickness)

Substrates:

- (111) Oriented silicon wafer (Semiconductor, Boron doped, 1×1 cm, 0.2 mm thickness)
- Glassy carbon (GC, Pine Research, 5 mm Dia × 4 mm thickness)
- Microporous gas diffusion layer (GDL, Fuel Cell Store, 2.5×2.5 cm, 0.4 mm thickness)
- Nafion Membrane (Nafion212, Fuel cell store, 2.5×2.5 cm, 50.8 μm thickness)

Single-cell station test:

- Commercial electrode – 40 % Platinum on Vulcan - Carbon Cloth (Pt/C, 0.3 mg/cm², Fuel Cell Store)
- H_2 gas (Messer Technogas s.r.o, 99.99 %)
- O_2 gas (Messer Technogas s.r.o, 99.99 %)
- N_2 gas (Messer Technogas s.r.o, 99.99 %)

Half-cell station test - rotating disk electrode (RDE):

- Electrochemical cell (Pine Research, 150 ml)
- Platinum counter electrode (Pine Research OD=0.5mm, 4.7 cm^2)
- Leak-Free Reference Electrodes (Ag/AgCl, LF-5 mm OD, Alvatek)
- Perchloric acid ($HClO_4$, 67-72 %, TraceSELECT™ Ultra, Honeywell)

2.2. Sample preparation - Magnetron sputtering

Magnetron sputtering is a physical vapor deposition method used to prepare thin film layers. It is quite a simple and fast method for the scalable preparation of surfactant-free catalytic materials. Moreover, its further undisputed advantage is the capability to reproducibly prepare catalysts with well-defined chemical and structural composition – ranging from multimetallic alloys and oxides/nitrides to strained and disordered systems.

The system consists of five essential components: vacuum chamber, target as material to be deposited, substrate, power supply, and magnet. The schematic illustration of the magnetron sputtering process is shown in Fig. 2.1.

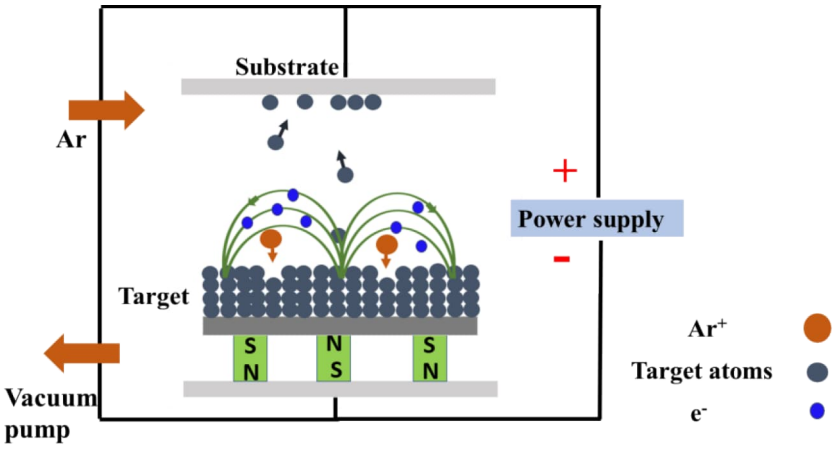

Fig. 2.1. *Schematic illustration of the magnetron sputtering process.*

For sample preparation, the chamber is first evacuated to a high vacuum, which is usually below a pressure of 1 Pa. The vacuum condition allows ejected atoms from the target to move freely toward the substrate and also minimizes sample contamination. After evacuation, the chamber is filled with working gas, which is typically Ar. The reactive O_2 or N_2 can also be used to prepare oxides or nitride coatings, respectively. A high voltage is then applied between the target (cathode) and anode, which leads to the ionization of the working gas near the target. The positively charged working gas ions are accelerated toward a negatively charged target and collide with the target. Those collisions cause the ejection of the surface atoms and further deposit on the substrate. In addition, magnets are placed below the target to increase the deposition rate. The electromagnetic field traps primary and secondary

electrons in cycloids over the surface of the target and increases the amount of ionized working gas, which results in a higher deposition rate.

Based on the target material, direct current (DC) and radiofrequency (RF) power supplies can be used. The conductive materials, like metals, can be sputtered using the DC power supply. The RF power supply with an alternating current at a high frequency (13.56 MHz) was used for non-conductive or semi-conductive materials to eliminate the surface charging of the target.

In this work, all samples were prepared using the magnetron sputtering technique. The multielement samples were simultaneously sputtered from two or three targets. The schematic illustration and the image of the instruments are shown in Fig. 2.2.

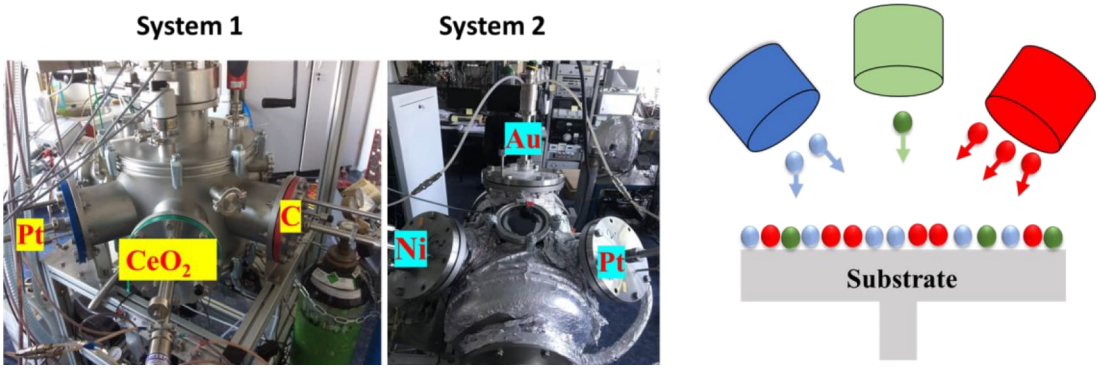

Fig. 2.2. *Images of magnetron sputtering instruments and schematic illustration of the deposition process.*

Both systems contain three individual magnetrons mounted toward the substrate, as illustrated in Fig. 2.2, and were used for fabricating single-, bi-, and ternary-compound catalyst layers. System 1 was used for the preparation of the Pt-C-CeO_2 catalyst. It consists of three 4″ circular TORUS magnetrons (Kurt J. Lesker) placed under the angle of 45° to the substrate. Three targets: Pt (99.99 %, Safina), C (99.99 %, Kurt J. Lesker), and CeO_2 (99.99 %, Kurt J. Lesker), were used in System 1. The distance between the target and substrate was 15.5 cm. RF power of 80 W was applied to the CeO_2 target, and DC power of 20 and 300 W was applied to the Pt and C targets, respectively. The working pressure was 0.15 Pa of Ar + O_2 mixture gas with a 4:1 ratio. The Si wafer, GDL, glassy carbon, and Nafion@212 were used as substrates for diverse experimental purposes.

System 2 was used for the preparation of Pt-Au and PtNi-Au catalysts, respectively. It consists of three 2″ circular TORUS magnetrons (Kurt J. Lesker)

placed under the angle of 45° to the substrate. Three targets: Pt (99.99 %, Safina), Au (99.99 %, Kurt J. Lesker), and Ni (99.99 %, Kurt J. Lesker), were used. The distance between the target and substrate was 12 cm. DC power was applied to all targets. The composition of Pt-Au and PtNi-Au layers varied by changing the DC power applied to the targets. The sputtering was carried out in 0.5 Pa of an Ar atmosphere.

2.3. Sample characterization

2.3.1. Atomic force microscopy

Atomic force microscopy (AFM) is one of the scanning probe microscopy techniques that generate 3D images of a surface by measuring the interaction between the sharp tip (<10 nm) and the surface of a sample. Fig. 2.3 depicts the photo and schematic illustration of the AFM instrument. The main components of AFM include a photodiode, laser, cantilever, piezoelectric scanner, and feedback loop, as shown in Fig. 2.3a.

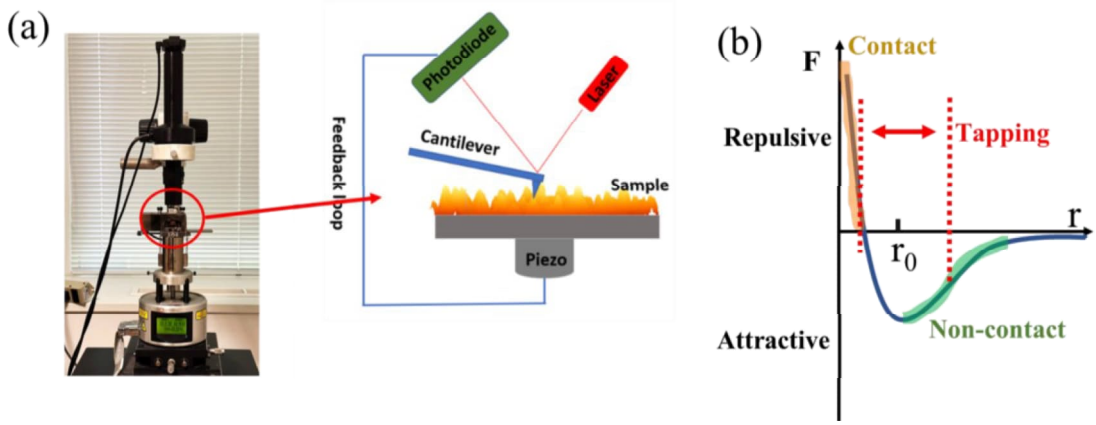

***Fig. 2.3**. (a) Image of Bruker MultiMode 8 AFM together with a simplified illustration of the main parts of the AFM system; (b) Force versus tip-sample distance curve.*

The principle of AFM is based on the interaction force between the sample surface and the sharp silicon probe supported on a flexible cantilever. As shown in Fig. 2.3b, the overall interaction force can be divided into repulsive and attractive forces based on the distance between the tip and the surface. The force most commonly associated with AFM is an interatomic van der Waals and electrostatic force. Nevertheless, other forces, such as magnetic, capillary, and steric forces, also play significant roles in tip-surface interactions in various experimental scenarios.

The AFM utilizes an optical detection system that involves a laser focused onto the backside of the cantilever, which has a reflective surface. The laser deflects towards the center of a quadrant photodiode (see Fig. 2.3a). As the tip scans over the surface of a sample, a deflected laser beam deviates from the center of the photodiode. The signal on different photodetector segments is converted to voltage and then applied through a feedback loop to the piezoelectric scanner to maintain a constant probe-sample force. Consequently, a topographic image of the sample is generated based on the voltage applied to the scanner.

There are three main AFM operation modes: contact mode, non-contact mode, and intermediate (tapping) mode, corresponding to the tip-surface interactions shown in Fig. 2.3b. In contact mode, the tip comes in direct contact with the sample surface, and the tip-sample interaction is governed by the repulsive force only. However, using the contact mode for measurements may potentially cause damage to both the sample surface and the tip. In non-contact mode, the tip oscillates at resonance frequency with an amplitude of about 1 nm several nanometres above the sample surface. The tip-sample interaction here is governed by the attractive force only. During measurements, the tip-sample interaction causes the resonant frequency of the cantilever to change, and this information is then used through a feedback loop to generate a topographic image of the sample. In tapping mode, the cantilever oscillates between the repulsive and attractive force regions at/or near its resonant frequency with an amplitude of 10 - 100 nm, allowing the tip to touch the surface periodically. During measurements, the amplitude of the cantilever changes, and this information is used through a feedback loop to generate a topographic image of the sample. Tapping mode remains widely employed because it minimizes the force applied to the sample, thus reducing the likelihood of sample or tip damage.

In this work, a MultiMode 8 AFM (Bruker), shown in Fig. 2.3a, was used to measure the surface topography of the catalyst layers and their thickness. All measurements were performed in tapping mode under ambient conditions. Silicon nitride SCANASYST-AIR probes (Bruker) with 70 kHz resonant frequency and a nominal tip radius of 2 nm were used. Acquired images were processed using the NanoScope 1.9 software (Bruker).

To measure the thickness of the catalyst layer, a droplet of varnish was first deposited on the Si wafer as a mask. The catalyst layer was then deposited by magnetron sputtering. Subsequently, the varnish was removed, leaving a sharp edge

between the masked and unmasked areas. Given the high vertical resolution of the AFM, this sharp edge representing the thickness of the catalyst layer can be accurately measured, as illustrated in Fig. 2.4.

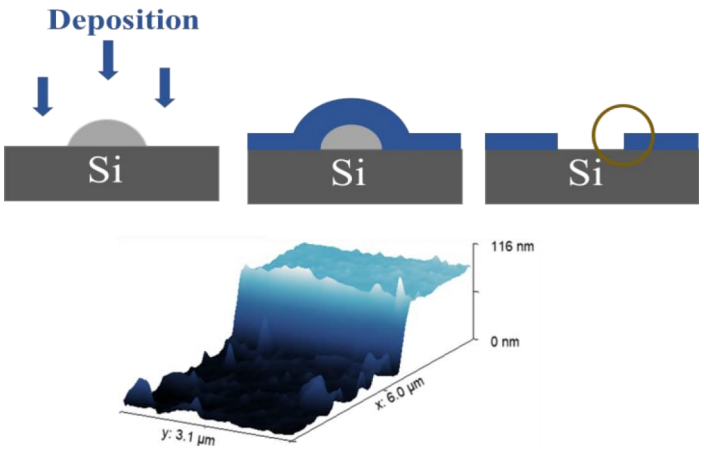

Fig. 2.4. *Thickness measurement of a catalyst layer deposited by magnetron sputtering using AFM.*

2.3.2. Scanning electron microscopy

A scanning electron microscope (SEM) is a type of electron microscope that provides a detailed image of a sample surface by scanning it with a focused beam of electrons in a raster scan pattern. The electron beam is emitted from a cathode through either thermal or field emission mechanisms and subsequently focused using a series of electromagnetic lenses. Typically, the electron beam has an energy range of 0.1 keV to 30 keV, and a spot size from 1 to 5 nm in diameter.

As illustrated in Fig. 2.5, when a focused electron beam interacts with the surface of a sample, distinct signals can be obtained based on the interaction volume within the sample, such as Auger electrons (AE), secondary electrons (SE), backscattered electrons (BSE), and X-rays (characteristic, continuum, fluorescence). The first three can be used to generate the image of the surface, while the latter can provide information about the sample composition via Energy-dispersive X-ray spectroscopy (EDX).

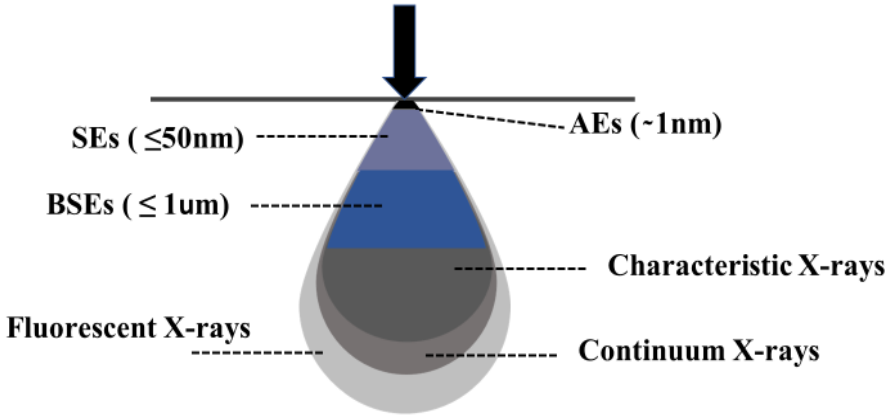

Fig. 2.5. *Electron–sample interaction volume and types of generated signal.*

The most common imaging mode is to collect SE that are ejected from conduction or valence bands of atoms at the sample surface. SE emission is a result of inelastic interactions between primary electron and atom. Such electrons have relatively low energies (≤ 50 eV) and thus a short mean free path within the sample. Hence, SE can only transfer from a few nanometers (around 50 nm) below the surface of a sample. In addition, the SE signal is highly localized at the point of interaction, which allows for obtaining high-resolution images of less than 1 nm.

Another image mode is the collection of BSE, which originates from elastic scattering between the primary electron beam and atoms within the sample. Because of significantly higher energy compared to SEs, BSEs originate from deeper regions within the sample. As a result, the resolution of BSE is lower than that of SE. The intensity of BSE, however, strongly depends on the atomic number (Z) of the element. Therefore, it can be used to analyze the distribution of different elements on the surface of a sample.

The AE and characteristic X-ray emission result from inelastic interaction. When the inner shell of an atom appears with a vacancy, the electron from a higher level will transit downward to fill the vacancy, resulting in the release of energy. This energy can be released through the ejection of an electron (AE) or in the form of an X-ray. This phenomenon is the so-called Auger effect. However, SEM imaging using Auger electrons is not widely utilized due to the low AE energies, which requires a specialized instrument such as a hemispherical analyzer. On the other hand, the characteristic X-ray can be detected and provide useful information about sample bulk composition. Characteristic X-ray is unique for each element because of their different electronic structures.

Fig. 2.6. *Image of a Tescan MIRA 3 scanning electron microscope.*

The morphology of the samples in this work was examined by means of a Mira 3 SEM (Tescan) shown in Fig. 2.6 operating at 30 keV electron beam energy using an SE detector. The bulk composition of the samples was determined by EDX using an XFlash 6|10 detector (Bruker) integrated into the SEM operating at 20 keV electron beam energy.

2.3.3. Photoelectron spectroscopy

Photoelectron spectroscopy (PES) or X-ray photoelectron spectroscopy (XPS) is a surface characterization tool that allows to measure the kinetic energy E_k of emitted photoelectrons from a solid and thus the characterization of both the material composition and chemical states of the constituent elements. The schematic illustration of PES is shown in Fig. 2.7. The photon source with an energy hv, where h is Plank constant, v is the frequency of the primary photon, hits the surface of a sample. This results in the emission of electrons from the surface of a sample. This phenomenon is called the photoelectric effect. The emitted electrons overcome the work function of the spectrometer Φ and enter a detector. The detector converts the photoelectrons into the current, plotting the photoelectron spectrum. Each element possesses a distinct collection of electrons with specific binding energies E_b associated with its core levels. Consequently, every element exhibits a series of peaks in the photoelectron spectrum at certain binding energies, determined by the photon energy and measured kinetic energies of electrons. The equation that describes the binding energy of emitted electrons is as follows:

（13） $E_b = h\nu - E_k - \Phi$

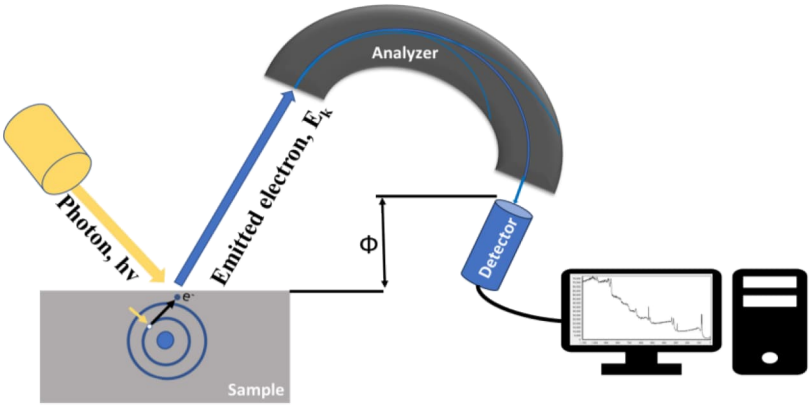

Fig. 2.7. *Illustration of basic principles of photoelectron spectroscopy.*

The analyzed photoelectrons are elastically scattered without losing kinetic energy as they travel through the sample bulk. The average travel path (probing depth) is associated with inelastic mean free path (IMFP) λ_m which varies with the E_k of photoelectrons and the primary photon energy (equation 13) [75]. For example, the typical X-ray sources like Mg Kα (1253.6 eV) or Al Kα (1486.6 eV) lines ensure up to 5 nm probing depth (depending on analyzed samples). In order to detect the very top surface information only, the lower energy primary photon sources can be applied. This can be realized by using synchrotron radiation, which provides photons with tunable energies ranging from 10 eV to several keV. PES also allows quantifying the sample composition from the acquired photoelectron spectra. The intensity of the PES peak (I_x) can be written as

(14) $I_x = I_0 \cos(\beta) A\, \delta x(h\nu)\, T(E_x)\, D(E_x) \int_0^\infty Nx(z) e^{-z/\lambda m(Ex)\cos(\theta)} dz$

Where individual components can be divided depending on

Photon sources:

- I_0, primary photon beam intensity
- β, primary photon beam incident angle
- A, analysis area

Measured samples:

- x, analyzed element

- $\delta_x(h\nu)$, photoionization cross-section
- $N_x(z)$, the concentration profile of an element at the depth z in the sample
- $\lambda_m(E_x)$, inelastic mean free path of emitted photoelectrons
- θ, photoelectron emitted angle

Analyzer:

- $T(E_x)$, analyzer transmission function
- $D(E_x)$, detector sensitivity

Based on equation 14, the XPS peak intensity depends on the measured elements, analyzer, and photon source. Knowing all the above-mentioned constants related to the photon source analyzer, and experiment geometry allows to calculate the concentration profile of the x-element. However, this is usually a very complicated mathematical task. The situation is much easier if the analyzed sample is homogeneous with constant concentration profiles of the elements. In such a case, the integration of equation 14 transforms it into a relatively simple equation:

$$(15) \quad I_{i,c} = N_x \cdot \sigma_{x,c} \cdot \lambda \cdot cos\theta \cdot I_0 \cdot T \cdot D \cdot A$$

In this equation, all the constants are combined into the so-called relative sensitivity factors (RSFs). The RSF value differs for different PES instruments and elements and is used to normalize the detected elements' XPS peaks [76]. A general expression for determining the atom fraction C_x of any constituent in a sample can be written as:

$$(16) \quad C_x = (I_x/S_x) / (\Sigma I_i/S_i)$$

where I is the specific spectra peak area, and S is RSF.

In this work, both XPS and synchrotron radiation-PES (SRPES) techniques were used. XPS measurements were performed using a conventional XPS instrument in an ultrahigh vacuum (UHV) chamber (base pressure 10^{-8} Pa) equipped with a multichannel electron energy analyzer (Phoibos 150, SPECS) and a monochromatized Al Kα X-ray source (photon energy −1486.6 eV). In turn, SRPES measurements were performed at the Materials Science Beamline at the Elettra synchrotron light source in Trieste, Italy. In contrast to the conventional XPS instrument with fixed X-ray energy, the beamline uses a plane grating monochromator which allows tuning synchrotron

light energy from 20 to 1000 eV. As a result, the excitation energy of photons can be set to a value ensuring the highest surface sensitivity (typically the top few atomic layers). Similarly to conventional XPS instruments, the end station consists of a UHV chamber (base pressure 10^{-8} Pa) equipped with a Phoibos 150 electron energy analyzer (Specs). For SRPES measurement, the sample was pre-cleaned by exposing it to a hydrogen atmosphere (5 mbar, room temperature) followed by gentle Ar^+ ion bombardment (1000 eV for 5 min). Conventional XPS analysis was conducted within the same setup using an Al Kα X-ray source with fixed energy of 1486.6 eV.

2.3.4. X-ray diffraction

X-ray Diffraction (XRD) is an analytical technique used to study the crystallographic structure of materials. XRD provides valuable insights into the crystal structure, lattice parameters, and phase composition of investigated materials. XRD instrument consists of an X-ray source, a sample holder, and a detector, as shown in Fig. 2.8. The technique is based on Bragg's law. The equation is as follows:

$$n\lambda = 2dsin\theta \quad (17)$$

where n is an integer representing the order of the diffraction peak (n = 1, 2, 3, ...), λ is the wavelength of the incident X-rays, d is the spacing between adjacent crystal planes in the lattice and θ is the angle of incidence of the X-rays with respect to the crystal lattice planes (see Fig. 2.8). When a monochromatic X-ray with wavelengths λ comparable to the spacing between the crystal planes (d) hits a crystalline material, the elastic scattering between the X-ray and crystal lattice takes place.

The scattered X-rays containing information about the arrangement of atoms in the crystal lattice are collected by the detector. The sample and/or the detector can be rotated, thus allowing data collection over a wide range of angles for a complete analysis of the sample crystal structure. The information about crystal structure, lattice parameters, and crystalline orientation of the sample with multiple elements can be determined by analyzing the position, shape, and intensity of the diffraction pattern.

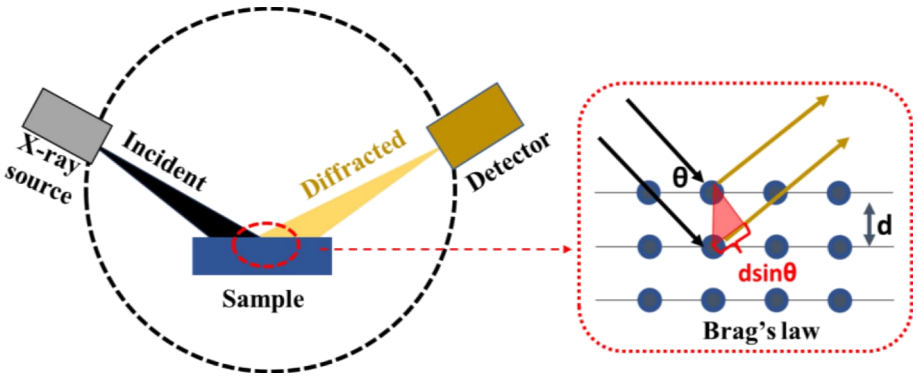

Fig. 2.8. Illustration of the basic principle of X-ray diffraction.

In this work, XRD measurements were performed using a SmartLab diffractometer (Rigaku). The diffractometer was equipped with a 9 kW rotating anode X-ray source (Cu Kα radiation with wavelength λ = 0.15418 nm) and a HighPix-3000 2D hybrid pixel single-photon counting detector. The XRD measurements were done in the parallel beam glancing angle X-ray diffraction (GAXRD) geometry with a parallel beam Soller slit collimator (acceptance 0.5°) in the diffracted beam. The constant angle of the incidence beam of 0.6° was used for all measurements. The catalyst layers were deposited on a Si wafer (1×1 cm) with a 10 nm carbon interlayer.

2.4. Activity and stability measurements

Electrochemical measurements play a pivotal role in understanding and characterizing electrochemical systems such as fuel cells. Typically, electrochemical measurements are performed in two different configurations: half-cell and single-cell. Half-cell measurements serve as a fundamental technique in electrochemistry for investigating individual electrode reactions and electrode materials under well-defined conditions. They allow isolating one electrode and studying its electrochemical behavior independently. However, the half-cell system is unable to replicate the actual operating conditions of a real PEMFC device, which is relatively complicated, and multiple factors, such as solid electrolyte, operation temperature, catalyst support, gas pressure, humidity, etc., can significantly impact the obtained results. Single-cell electrochemical measurements provide a complete view of device-level performance by examining the behavior of a complete electrochemical device, including both anode and cathode compartments separated by polymer electrolyte operating under real conditions.

2.4.1. Rotating disc electrode

The rotating disc electrode (RDE) is an electrochemical setup for studying the kinetics and mechanism of electrochemical reactions at the surface of a rotating electrode in the half-cell configuration. The system consists of a rotating component, an electrochemical cell, a potentiostat, electrolyte, and gas inserts, as illustrated in Fig. 2.9. The electrochemical cell is configured in a typical 3-electrode setup including a working electrode (WE), which refers to an investigated catalyst, a reference electrode (RE) that allows accurate control of the potential between WE and RE and a counter electrode (CE) which is used to complete the electrical circuit by allowing the flow of current to and from the WE. The rotator is used to perform the rotation of the WE at a controlled speed (400 to 10, 000 rpm) to provide controlled conditions for studying various electrochemical processes. This rotation creates a hydrodynamic flow of the electrolyte solution near the surface of WE, which enhances the mass transport of reactants and products to and from the electrode, as illustrated in Fig. 2.9. By measuring the current response at the rotating electrode as a function of time and potential it is possible to determine various important parameters of an electrochemical reaction.

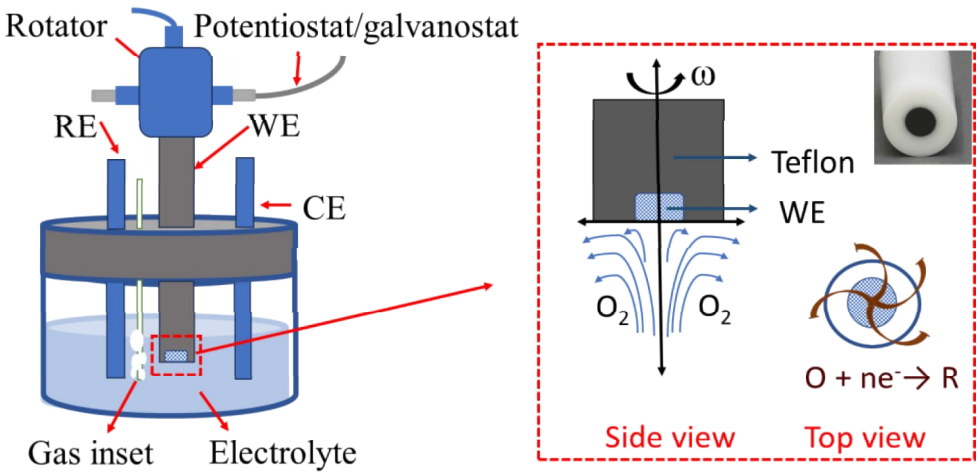

Fig. 2.9. *The schematic illustration of the RDE system.*

For example, when investigating ORR kinetics, the electrolyte is saturated with O_2 gas, and the working electrode (WE) is set to rotate at a specific angular velocity (ω) while applying a linear potential ranging from the open circuit potential to a negative potential. The resulting current response, known as the ORR polarization

curve, can be divided into three key regions: the kinetic-controlled (KC) region, the diffusion-limited (DL) region, and the mixed kinetic and diffusion (MKD) region. These regions are illustrated for a polycrystalline Pt catalyst in Fig. 2.10.

In the KC region (pink region in Fig. 2.10), the current density is very low due to insufficient overpotential to overcome the electrochemical reaction barrier. Hence, the overall ORR rate at this region is primarily determined by the surface reaction kinetics.

In the DL region (yellow), the current density reaches saturation, where the reaction rate is no longer limited by the surface reaction kinetics due to sufficient overpotential but by the mass transport of reactants.

In the MKD region (green), the current density sharply increases as the surface reaction kinetics accelerate with rising overpotential. Moreover, the rate of dissolved oxygen at the electrode closely correlates with the ORR rate. As a result, the overall ORR rate is co-dominated by both the surface reaction kinetics and the mass transport of reactants.

By analyzing ORR polarization curves, several key parameters can be obtained:

- The half-wave potential ($E_{1/2}$) denotes the potential at which the current density achieves half of its maximum value, which provides valuable insights into the activity of the investigated catalyst [77].
- The limiting current density (j_L) is the maximum achievable current density in the DL region [53]. According to the Levich equation, the j_L can be expressed as follows:

$$j_L = 0.620 n_e F D_{O2}^{2/3} V^{-1/6} C_{O2}^{\infty} \omega^{1/2} \quad (18)$$

  where n_e is the number of ORR transferred electrons (≤ 4), F is Farady constant (96485 C $\cdot mol^{-1}$), D_{O2} is the oxygen diffusion cofficient (1.93×10^{-5} $cm^2 \cdot s^{-1}$), V is the viscosity of the electrolyte (1.01×10^{-2} $cm^2 \cdot s^{-1}$), C_{O2} is the concentration of dissolved oxygen (1.26×10^{-6} $mol \cdot cm^{-3}$).
- The kinetic current density (J_k), generally measured at 0.9 V_{RHE}, directly represents the kinetic rate at which the electrochemical reaction occurs at the electrode interface and can be calculated using the Koutechky-Levich equation:

(19) $\frac{1}{j} = \frac{1}{j_k} + \frac{1}{j_L}$

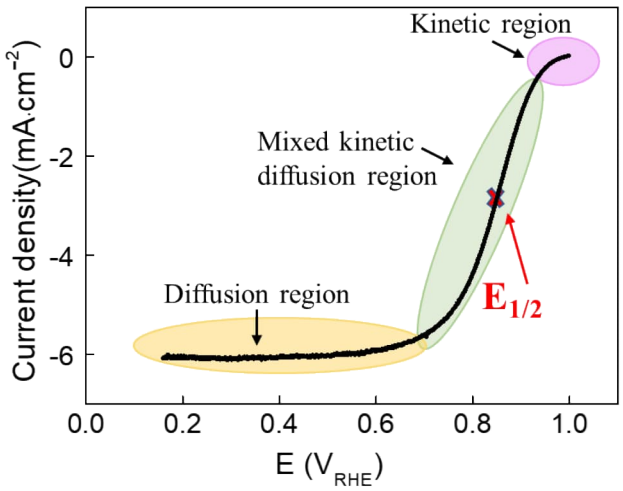

Fig. 2.10. *ORR polarization curve of polycrystalline Pt captured in O_2-saturated 0.1 M $HClO_4$ at 1600 rpm.*

In this work, the ORR activity of catalysts was evaluated using an RDE setup (Pine Research) connected to an SP-150 potentiostat (Bio-Logic). An electrochemical cell (Pine Research) contained three electrodes: a catalyst deposited onto GC (Pine Research, 5 mm diameter, 0.196 cm^2 surface area) as a WE, platinum wire (99.99 %, Pine Research) as a CE, and Ag/AgCl (OD = 5mm, Alvatek) in saturated KCl as a RE. All measurements were performed at room temperature. All potentials refer to a reversible hydrogen electrode (RHE). The ORR polarization curves were acquired in O_2-saturated electrolytes (0.5 M H_2SO_4 and 0.1 M $HClO_4$) by applying linear potential on the WE with a scan rate of 20 $mV \cdot s^{-1}$ and a rotation speed of 1600 rpm.

2.4.2. Cyclic voltammetry

Cyclic voltammetry (CV) is a widely used electrochemical technique that allows gathering information about the redox behavior, electrochemical kinetics, and other electrochemical properties of the investigated system. It employs cycling the potential applied to the sample in a controlled manner while capturing the current response, known as a cyclic voltammogram. CV is typically performed in a standard 3-electrode electrochemical half-cell described in the previous chapter. During the experiment, a linear potential is applied to the WE across a predetermined range in forward (anodic) and backward (cathodic) directions. This process induces

electrochemical reactions on the catalyst surface, causing the resultant change in current. Cyclic voltammograms exhibit characteristic features, including oxidation and reduction peaks, which provide valuable information about the investigated system.

Fig. 2.11 shows a typical CV curve of polycrystalline Pt thin film acquired in N_2 purged 0.5 M H_2SO_4 solution. It consists of three characteristic features: the hydrogen adsorption/desorption region (blue) at 0.05 $V_{RHE} < E < 0.4$ $V_{RHE,}$ also known as known as the hydrogen underpotential deposition (H_{UPD}) region, the platinum oxidation/reduction region (grey) at $E > 0.7$ V_{RHE}, and the double layer region (orange) at 0.4 $V_{RHE} < E < 0.7$ V_{RHE} which represents a capacitive-like current due to charging/discharging at the platinum-electrolyte interface.

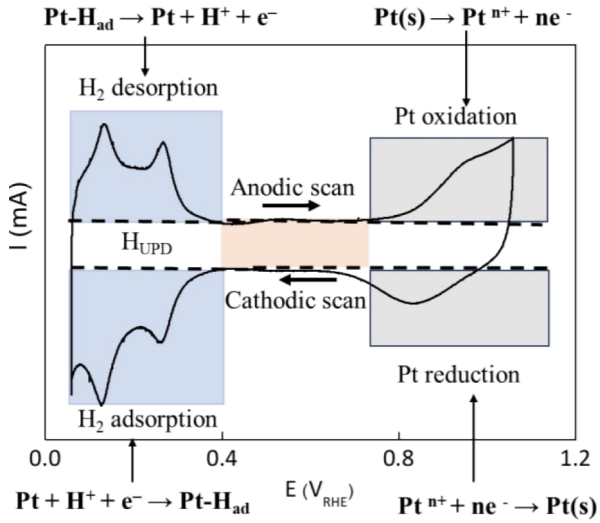

Fig. 2.11. *Typical cyclic voltammogram of polycrystalline Pt acquired in N_2-saturated 0.5 M H_2SO_4.*

In this work, CV was mainly used to perform accelerated degradation tests (ADTs) by applying multiple CV cycles to different upper potential limits and calculating electrochemically surface active area (ECSA). Specifically, ADTs were performed in N_2-saturated electrolyte by applying 2000 CV cycles from 0.05 to 1.0, 1.2, and 1.5 V_{RHE} at 500 $mV \cdot s^{-1}$ scan rate. The ECSA was calculated by integrating the double-layer corrected charge of the hydrogen desorption peak in the H_{UPD} region and dividing it by a value of 210 $\mu C \cdot cm^{-2,}$ which corresponds to a theoretical value of a monolayer of adsorbed hydrogen atoms on platinum with a smooth surface [58] and platinum loading. The total charge (Q) can be obtained:

$$(20) \quad Q = \frac{1}{v} \int i(E)dE$$

where i is current, E is potential and v is the scan rate.

The ECSA of Pt can be calculated through normalization as follows:

$$(21) \quad ECSA = Q/(Q_m \cdot m_{Pt})$$

where m_{Pt} is Pt loading.

Another CV-based technique used in the thesis to calculate ECSA is CO stripping. During the experiment, the catalyst was deliberately poisoned with a monolayer of adsorbed CO (CO*) by purging CO into an electrolyte (under a potential 0.15 V_{RHE} for 3 mins). Subsequently, the system was purged with N_2 for 20 minutes to remove residual CO from the electrolyte. A linear anodic potential scan with a 20 $mV \cdot s^{-1}$ scan rate is then applied to the WE. As the potential increases, the oxidation of CO occurs, resulting in the formation of a well-defined CO oxidation peak (orange) on the voltammogram, as shown in Fig. 2.12. By integrating the CO-oxidation peak, the ECSA of Pt was estimated through equation 21. In contrast to the previous case, a value of 420 $\mu C \cdot cm^{-2}$ which corresponds to a theoretical value of a monolayer of adsorbed CO on platinum with a smooth surface was used.

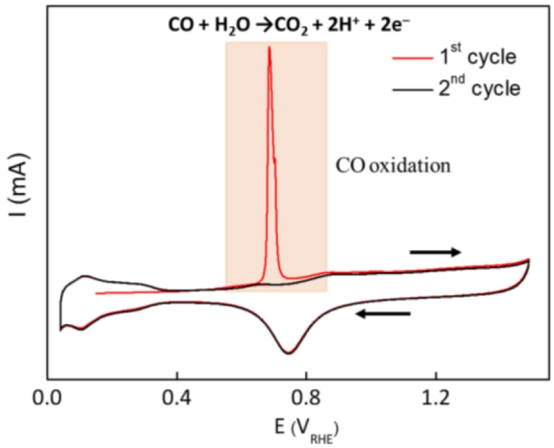

Fig. 2.12. *CO-stripping voltammogram of polycrystalline Pt acquired in N_2-saturated 0.1 M $HClO_4$.*

2.4.3. PEMFC test station

The activity of the investigated catalyst in a single-cell configuration was performed using the real fuel cell device (see scheme in Fig. 1.2) by measuring polarization and power density curves illustrated in Fig. 2.13.

Typically, the polarization curve is characterized by a drop in voltage when the current is increased. It is divided into activation, ohmic, and mass transport losses. At low currents, the main reason for the voltage drop is activation polarization, when it is necessary to overcome the activation energy of the reaction. This part of the curve is affected by the catalyst properties. When the current is further increased, the voltage drops more slowly due to ohmic losses associated with the electronic and ionic resistance of individual cell components. As the current increases continuously, losses are predominantly attributed to the mass transfer of reactants, causing a steep drop in the voltage across the fuel cell.

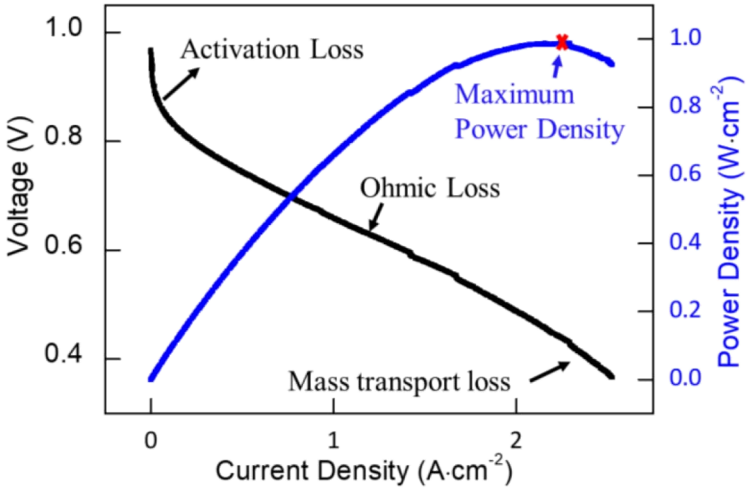

Fig. 2.13. *Polarization and power density characteristics of a single cell.*

Another important characteristic of single-cell measurement is the maximum power density (see Fig. 2.13). For evaluating the performance of catalysts, the specific power density can be calculated by normalizing the maximum power density with respect to the Pt loading (M_{Pt}). This normalization allows for the comparison of the various catalysts, considering their loading and the size of the active electrode surface.

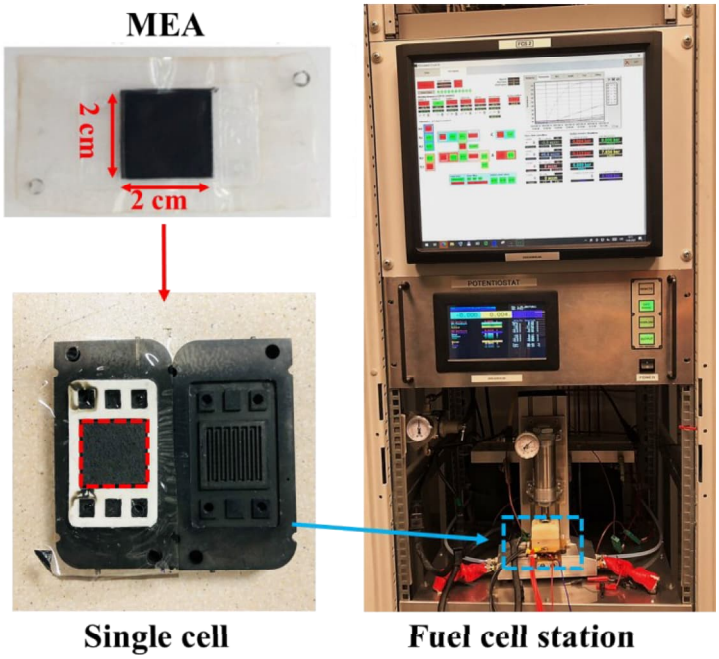

Fig. 2.14. *Image of the single-cell assembly in fuel cell test station.*

A single cell was constructed with MEA, gasket, and bipolar plates with gas flow channels, as shown in Fig. 2.14. MEA was assembled with an active area of 4 cm^2 of a gas diffusion layer (GDL, Sigracet 29 BC) with a deposited catalyst as a cathode and commercial 0.3 $mg \cdot cm^{-2}$ 40 % platinum on Vulcan - Carbon Paper Electrode as an anode separated by a Nafion 212 membrane (Fuel cell store). The cell was sealed by sandwiching MEA between two bipolar plates and compressed by a piston to a pressure of 8 bars. Before measurement, the cell was flushed with N_2 for 10 minutes to eliminate residual gases from previous measurements. Measurements were performed at 80 °C, 50 kPa gas backpressure using H_2/O_2 feed with constant gas/current stoichiometry ratios of 1.2/2. The polarization curves were obtained following the US Fuel Cell Council Single test protocol [78].

2.4.4. Scanning flow cell combined with an inductively coupled mass spectrometer

A scanning flow cell (SFC) combined with an inductively coupled mass spectrometer (ICP-MS) allows in situ online detection of electrochemically dissolved metals. The instrument consists of three main parts: SFC, movable stage, and ICP-MS, as shown in the schematic illustration in Fig. 2.15. The investigated sample is mounted on a movable stage, which allows to set off a precise position of interest using both top

and side view cameras and ease of moving from one location on the sample to another, as illustrated in Fig. 2.15. When the specially designed micro-SFC is brought in contact with the working electrode (WE) surface through its opening (the applied force is adjusted using a force sensor and regulated through a feedback loop), it forms a miniaturized three-electrode electrochemical cell, together with a reference electrode and a counter electrode, which allows performing various electrochemical measurements. During an electrochemical measurement, the dissolved metals (if any) are transported downstream to the ICP-MS under a controlled flow rate provided by a peristaltic pump and the purged gas. The electrolyte containing dissolved metals enters the nebulizer, which allows to generate of a fine electrolyte mist in the spray chamber. A fraction of this mist then enters the ICP torch plasma, where it ionizes and enters a quadrupole mass spectrometer. As a result, detected ions form a time-resolved signal of metal dissolution, which is directly correlated to the applied electrochemical protocol in the SFC.

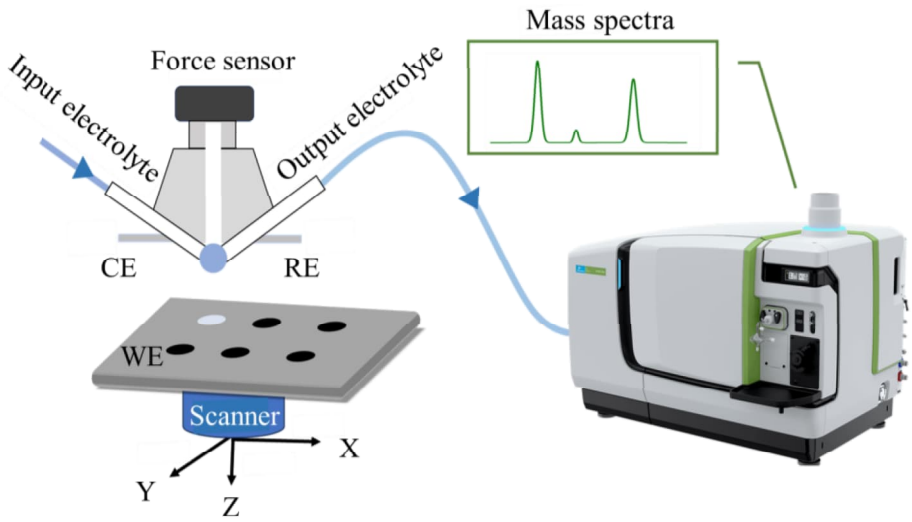

Fig. 2.15. *Schematic illustration of the SFC-ICP-MS setup.*

Electrochemical transient dissolution of ^{195}Pt, ^{197}Au, ^{60}Ni, and ^{140}Ce in this work was monitored employing the SFC-ICP-MS system at the Helmholtz Institute Erlangen-Nürnberg (HI-ERN). More details about this setup can be found elsewhere [79, 80]. The sample in the form of magnetron sputtered layers deposited on a glassy carbon plate (Alfa Aesar) served as a working electrode, saturated Ag/AgCl (Metrohm) was used as a reference electrode, and a glassy carbon rod (HTW Sigradur G) was used as a counter electrode. The working electrode contact area was approximately 1.1 mm^2.

Freshly prepared 0.1 M $HClO_4$ from 70 % perchloric acid (Suprapur, Merck) and ultrapure water (Milli-Q IQ 7000, Merck) was used as an electrolyte with a flow rate from 197 to 205 µL min^{-1}. Continuous argon purging was used to deaerate the solution. The potential was controlled with a Reference 600 potentiostat (Gamry). Metal dissolution was monitored on a NexION 300 (PerkinElmer) ICP-MS via calibration from Pt Au, Ni, and Ce solutions (Certipur, Merck), while 10 µg L^{-1} ^{187}Re was used as the internal standard for ^{195}Pt and ^{197}Au, 10 µg L^{-1} ^{59}Co for ^{60}Ni and 10 µg L^{-1} ^{115}In for ^{140}Ce. Total quantities of dissolution were obtained via integration of the transient dissolution profiles.

3. Results

3.1. Bimetallic Pt–Au alloy catalysts

3.1.1. Introduction

As mentioned in the chapter of the introduction, gold has been demonstrated as one of the most promising alloying elements to suppress Pt dissolution due to its chemical inertness. As of now, it is generally recognized that the incorporation of an appropriate amount of Au can elevate the oxidation potential of Pt and protect the surface unstable atoms from dissolution.

For example, Zhang et al., using *in situ* X-ray absorption near-edge spectroscopy and voltammetry, showed that enhanced stability of Pt nanoparticles decorated with Au clusters is attributed to the increase of Pt oxidation potential [71]. On the other hand, Takahashi et al. demonstrated that the improved ORR durability of the Au_x/Pt_{100} system is attributed to the blocking of the coordinatively unsaturated sites on the Pt nanoparticles, as Au atoms preferentially occupy lower-coordinated sites, such as corners and edges, on the Pt NPs [81]. Similarly, in a recent paper, Stamenkovic et al. reported that Au on the surface selectively protects low-coordinated Pt atoms from dissolution [70]. In the case of the Pt/Au reverse system, authors concluded that the Au underlayer promotes the ordering of Pt surface atoms toward a more stable (111) structure, resulting in decreasing Pt dissolution. For instance, using an SFC coupled to ICP-MS, Cherevko et al. directly demonstrated that the Au underlayer effectively inhibits Pt dissolution [82].

Nevertheless, there are drawbacks to Pt–Au alloy catalysts. Although the addition of Au increases the stability of Pt, it has a detrimental effect on its activity. Since Au is not active for ORR, Au atoms on the surface block the active Pt atoms, thus reducing the overall electrochemically surface active area of the catalysts. Moreover, due to the larger atomic size of Au, alloying of Au with Pt leads to tensile strain modifications of the Pt lattice, which is unfavorable for ORR [83]. Consequently, the activity and stability of the Pt–Au alloy catalyst strongly depend on its structure and composition. Precise engineering of catalysts is thus required to counterbalance both their activity and stability.

Most of the aforementioned studies dealt with rather model Au/Pt or Pt/Au systems. In this chapter, we will investigate bulk Pt–Au alloy catalysts. The catalysts

were fabricated in the form of thin layers utilizing the magnetron co-sputtering technique. This method offers precise control over the composition of Pt–Au catalysts by adjusting the power supplied to the Au and Pt targets (for more details, see the experimental part).

As mentioned above, Au has a detrimental influence on Pt–Au activity. The study focused on Pt–Au alloys with a relatively small amount of Au. Overall, five samples were prepared, including $Pt_{95}Au_5$, $Pt_{90}Au_{10}$, and $Pt_{80}Au_{20}$, as well as reference monometallic Au and Pt (denoted hereafter as PtAu5, PtAu10, PtAu20, Au, and Pt) to investigate the composition-activity-stability relationship.

3.1.2. Characterization of Pt–Au alloy catalysts

The SEM and AFM images of the as-deposited layers are present in Fig. 3.1. The Pt–Au catalysts with different compositions show very similar morphology. Catalyst layers consist of evenly dispersed grains positioned close to each other, which is typical for the sample prepared by the magnetron sputtering technique. The grains themselves have high-angle boundaries similar to those found in actual catalyst nanoparticles used in PEMFC devices.

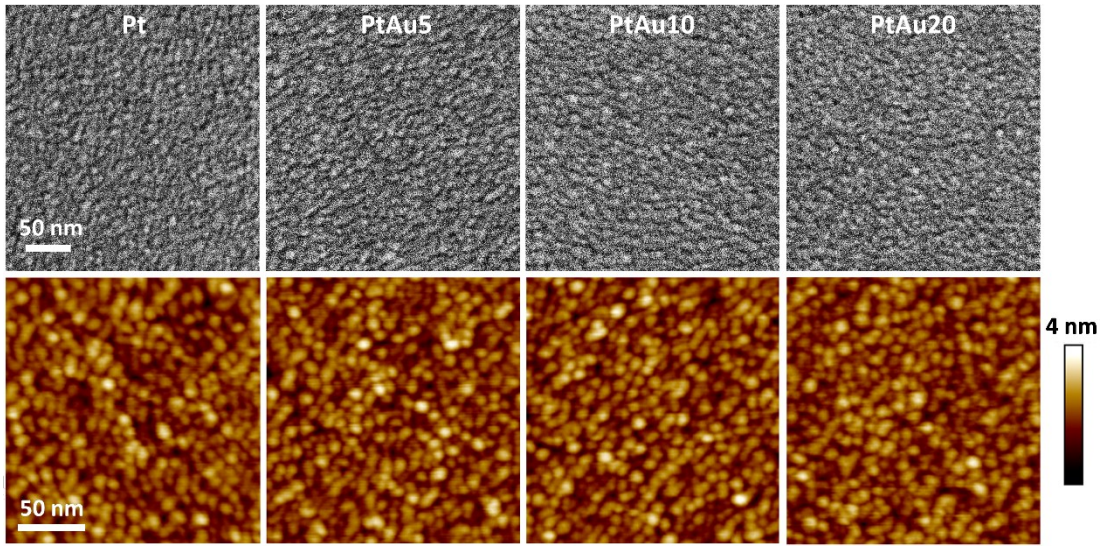

Fig. 3.1. *SEM (upper row) and AFM (bottom row) images of the as-deposited monometallic Pt and Pt–Au alloy catalysts.*

Based on the analysis of AFM images, the root mean square roughness (Rq, the vertical roughness of the surface) and correlation length ξ (the lateral roughness associated with the grain size) remain almost identical with negligible deviation

($\xi = 4.5 \pm 0.1$ nm, Rq = 0.5 ± 0.01 nm). Microscopic observations provide evidence of nearly identical morphology across the samples with different compositions, suggesting that morphology will not significantly impact the ORR activity and stability of the Pt–Au alloy catalyst. Instead, activity and stability are expected to depend solely on the Pt–Au composition. Thus, accurate composition control will be crucial for precise monitoring of the activity and stability of Pt–Au alloys.

The EDX and XPS spectra of the Pt–Au alloys are plotted in Fig. 3.2. Fig. 3.2a shows the EDX spectra, with deconvoluted peaks for Pt and Au corresponding to their respective Lα X-ray energies at 9.44 keV and 9.71 keV. The relative atomic composition of all investigated samples ($Pt_{95}Au_5$, $Pt_{88}Au_{12}$, and $Pt_{77}Au_{23}$), as quantified from their corresponding EDX spectra, match the intended composition. The XPS spectra in Fig. 3.2b are composed of two doublets at about 84 eV and about 71 eV corresponding to Au 4f and Pt 4f, respectively. The relative atomic compositions quantified from XPS spectra ($Pt_{96}Au_4$, $Pt_{90}Au_{10}$, and $Pt_{78}Au_{22}$) are also in good agreement with the intended compositions.

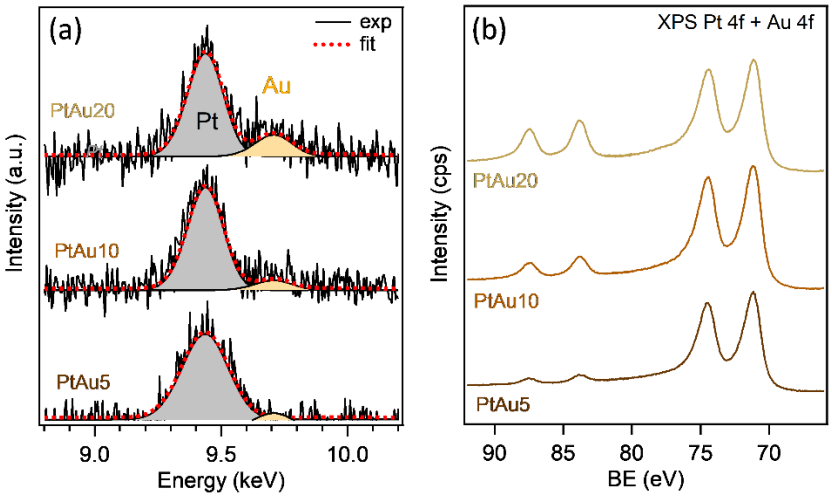

Fig. 3.2. *(a) EDX spectra and (b) XPS spectra acquired for as-deposited Pt–Au alloy catalysts.*

Since both EDX and XPS techniques are rather bulk-sensitive, as-deposited samples were then analyzed using the surface-sensitive SRPES technique. When using 180 eV excitation energy, it allows for the precise analysis of the composition of the outermost 2–3 monolayers of the catalyst, which is the most important part of the catalytic layer.

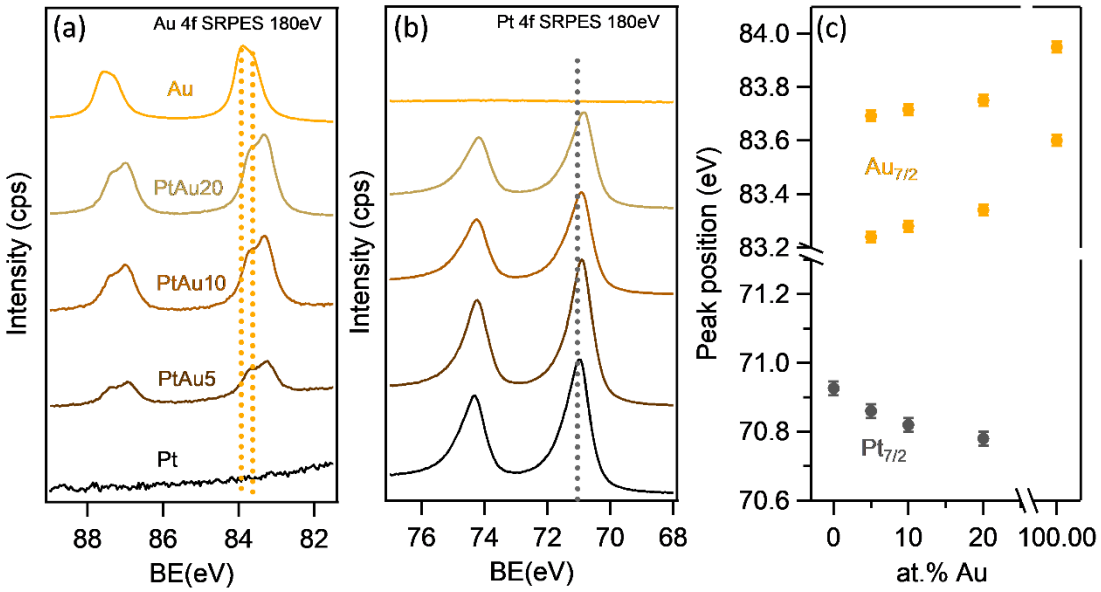

Fig. 3.3. *(a) SRPES Au 4f and (b) SRPES Pt 4f spectra obtained for as-deposited Pt–Au alloy catalysts at 180 eV excitation energy. (c) Evolution of Au* $4f_{7/2}$ *and Pt* $4f_{7/2}$ *peak positions with increasing Au content extracted from the spectra shown in (a) and (b).*

The Au 4f and Pt 4f SRPES spectra measured for all investigated samples are shown in Fig. 3.3a and b, respectively. The relative atomic compositions of Pt–Au alloys quantified from corresponding spectra taking into account sensitivity factors are $Pt_{94}Au_6$, $Pt_{88}Au_{12}$, and $Pt_{78}Au_{22}$, which nicely correlate with the composition obtained using more bulk-sensitive EDX and XPS results discussed above as well as nominal compositions. Fig. 3.4a additionally compares compositions of investigated Pt–Au catalysts calculated using multiple techniques with various probing depths, including CO stripping and XRD, which will be discussed below. The compositions measured by different techniques correlate nicely, with negligible deviations. This unambiguously confirms the uniform composition gradient in the Pt–Au catalyst deposited by magnetron co-sputtering. The ball model in Fig. 3.4b additionally schematically illustrates the outermost surface of investigated catalysts at specific Pt–Au compositions, depicting the corresponding overall distribution of Au and Pt atoms on the alloy surface.

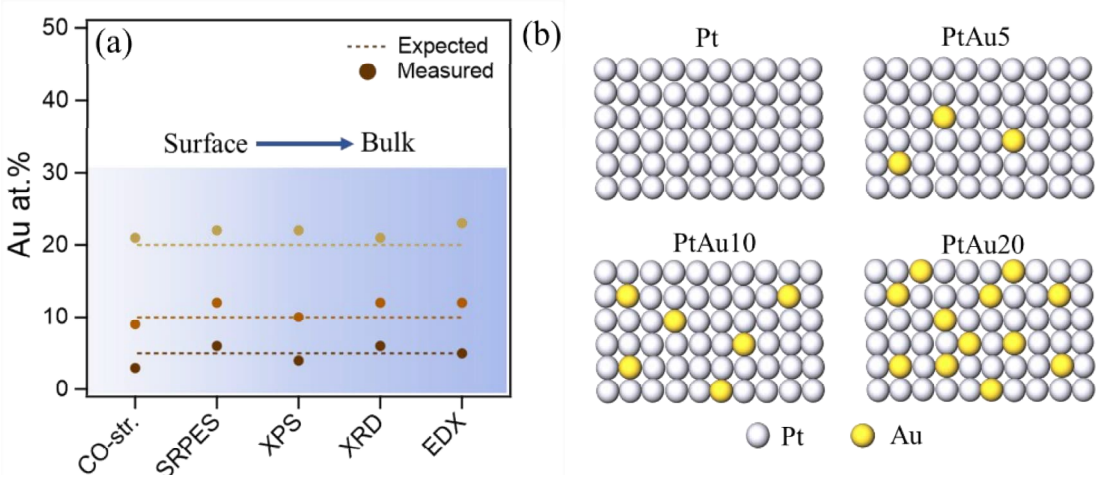

Fig. 3.4. *(a) Comparison of the Pt–Au alloys relative composition calculated using CO stripping (Fig. 3.6b), SRPES (Fig. 3.3a,b), XPS (Fig. 3.2b), XRD (Fig. 3.5a), and EDX (Fig. 3.2a) techniques (dashed lines represent nominal compositions); (b) Schematical illustration of the outermost surface at specific Pt–Au compositions.*

The resolution of the SRPES technique also allows for the accurate determination of the surface chemical state of constituent elements and thus provides information about the electronic structure of the alloy. The high-resolution Pt 4f spectrum of monometallic Pt (bottom spectrum in Fig. 3.3b) consists of a single doublet at 70.95/74.25 eV BE, which is a fingerprint feature of metallic platinum [98, 99]. In addition, the Au 4f of monometallic Au (upper spectrum Fig. 3.3a.) consists of two doublets at 83.95/87.69 eV and 83.6/87.36 eV, assigned to the Au atoms on the subsurface and surface, respectively [84, 85]. Compared with their monometallic spectra, the Pt 4f and Au 4f spectra of Pt–Au alloys are significantly shifted. The position of Au $4f_{7/2}$ and Pt $4f_{7/2}$ peaks are summarized for all investigated samples in Fig. 3.3c for better comparison. It can be observed that with increasing Au content in the Pt–Au alloy, the Pt 4f core levels are continuously shifting toward lower BEs while the Au 4f spectrum shifts to higher BEs. The detailed peak position, together with its deviation for alloys with respect to the one for monometallic constituents, are additionally summarized in Table. 3.1. Overall, such shifts in the case of bimetallic compounds represent clear evidence of the alloy formation and corresponding modification of Pt electronic structure due to its alloying with Au manifested in a charge transfer due to orbital overlap [86, 87]. The relative shift of Pt 4f core level for Pt–Au alloys with respect to its position for monometallic Pt calculated from

corresponding SRPES spectra is 0.1 %, 0.15 %, and 0.21 % for PtAu5, PtAu10, and PtAu20, respectively.

Table. 3.1. *Summarized Au $4f_{7/2}$, Pt $4f_{7/2}$ peaks position for Pt–Au catalysts together with its deviation for different alloys with respect to the one for monometallic Pt and Au.*

Samples	Subsurface		Surface			
	Au $4f_{7/2}$ (eV)	ΔBE	Au $4f_{7/2}$ (eV)	ΔBE	Pt $4f_{7/2}$ (eV)	ΔBE
Au	83.95	0	83.6	–	–	–
PtAu20	83.75	-0.2	83.34	-0.26	70.78	-0.15
PtAu10	83.72	-0.23	83.28	-0.32	70.82	-0.11
PtAu5	83.69	-0.26	83.24	-0.36	70.86	-0.07
Pt	–	–	–	–	70.93	0

XRD was further used for characterizing the crystal structure of the as-deposited catalyst layer, i.e. the influence of Au incorporation on the Pt lattice (geometrical effect). The acquired diffraction patterns for monometallic Pt and the investigated Pt–Au alloys are plotted in Fig. 3.5a. Four characteristic diffraction peaks of monometallic Pt (bottom diffractogram) are located at 2θ values of 41.1°, 46.7°, 67.9°, and 81.8° corresponding to the (111), (200), (220), and (311) planes of the face-centered-cubic (fcc) lattice of platinum (JCPDF 04-0802) [88]. Upon alloying with Au, the diffractograms do not change their shape, indicating that the fcc lattice remains for Pt–Au alloys. The crystallite size calculated from corresponding diffractograms is similar for all investigated samples and slightly variates within the range of 5–6 nm, as shown in Fig 3.5c. A continuous shift of all peaks toward a lower angle compared to the one for monometallic Pt can be observed with an increase in Au content, which is clearly evident in the inset of Fig. 3.5a for the (111) reflection. Two conclusions can be made from this observation. First, this shift highlights the overall alloy formation. Second, the negative shift specifically corresponds to the development of tensile strain within the Pt lattice [89]. Theoretically, the Au lattice constant (0.407Å) is slightly larger than the Pt lattice constant (0.391 Å) [90]. As a result, the mixture of Pt and Au atoms causes an increase in the Pt-Pt inter-atomic distances. The lattice constant for Pt–Au catalysts quantified from XRD patterns is shown in Fig. 3.5b together with the one for monometallic Pt and Au samples, to facilitate the comparison. It can be observed that as Au content increases, the lattice constant linearly increases, perfectly

following Vegard's law. The relative lattice expansion for Pt–Au alloys with respect to the one for monometallic Pt calculated from corresponding diffractograms is 0.25 %, 0.44 %, and 0.82 % for PtAu5, PtAu10, and PtAu20, respectively.

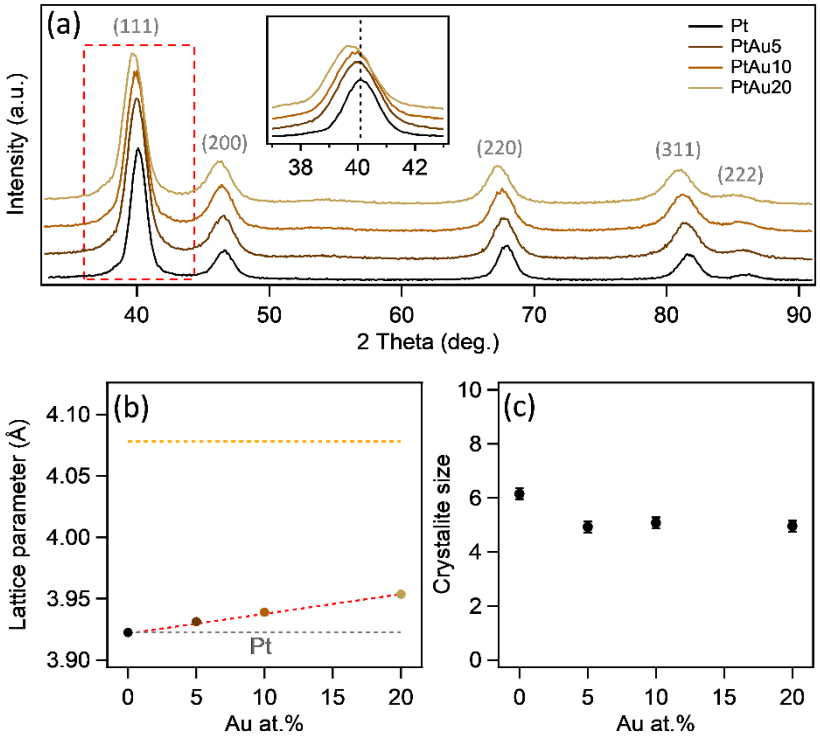

Fig. 3.5. *(a) XRD patterns of the as-deposited monometallic Pt and Pt–Au alloy catalysts (inset highlights the (111) reflections); (b) evolution of lattice parameter calculated from the corresponding diffractograms; (c) evolution crystallite size calculated from the corresponding diffractograms.*

Overall, the measured tensile strain should have a negative impact on the ORR activity in terms of increasing the oxygen binding energy, as highlighted in Chapter 1.3 of the Introduction section. On the other hand, considering the electronic structure modification obtained by SRPES, the addition of Au negatively shifts the binding energy of 4f electrons of Pt. This means that Pt takes electrons from Au, and according to the d-band theory, it is favorable for ORR. The interplay of these two effects should then dictate the ORR activity of Pt–Au alloys.

3.1.3. Effect of Au on the activity of Pt–Au alloy catalysts

The electrochemical properties of catalysts were further analyzed in the half-cell system. The CVs of the as-deposited Pt–Au catalyst captured in N_2-saturated 0.1 M $HClO_4$ are shown in Fig. 3.6a and compared with CVs of monometallic Pt and Au. CVs of monometallic Pt and Au exhibit electrochemical signatures typical for polycrystalline Pt (H_{UPD} and Pt oxidation/reduction) and polycrystalline Au (Au oxidation/reduction). The detailed description of Pt CV can be found in the experimental section. The CV of monometallic Au shows the oxidation and reduction peaks at 1.45 V_{RHE} and 1.15 V_{RHE}, respectively, which occur at significantly higher potentials than those for Pt. CVs for Pt–Au alloys preserve electrochemical features from both constituents. However, it can be observed that all peaks associated with Pt decrease while all peaks associated with Au increase with Au content increase. Two observations can be highlighted here. The decrease in the H_{UPD} area is linked to the decreased ECSA of Pt due to more Au atoms present on the alloy surface (see ball model in Fig. 3.4b). The continuous shift of the Pt reduction peak to the lower potentials and the Au reduction peak to higher potentials can be attributed to electronic and geometrical modifications of Pt due to its alloying with Au, described in detail in the previous section.

It has been reported that the calculation of electrochemically active surface area using H_{UPD} peaks is not accurate in the case of alloy surfaces [91, 92]. In order to accurately determine the ECSA of the Pt, the CO-stripping method was applied. The acquired CO-stripping voltammograms of the as-deposited catalysts acquired in CO-saturated 0.1 M $HClO_4$ are shown in Fig. 3.6b. The total charge evaluated from CO-oxidation peaks plotted in Fig. 3.6c is directly related to the ECSA of Pt on the outermost layer of catalysts. It can be seen that the charge value decreases as the Au content increases due to the presence of Au on the surface. CO desorption charge was then used to calculate the relative compositions of all investigated catalysts, considering that it is 100 % for monometallic platinum. The results are summarized in Fig. 3.4a and agree well with that measured by SRPES, XPS XRD, and EDX.

Additional information can be extracted by analyzing the position and shape of CO-stripping voltammograms. For the monometallic Pt, the center of the stripping peak is at 0.68 V_{RHE} and then continuously upshifts with Au content increase, reaching 0.74 V_{RHE} for the PtAu20 sample. It indicates that Pt-CO_{ad} binding energy increases

when alloyed with Au due to electronic and geometrical modification of Pt [87, 93]. In addition, a small tail in the CO-stripping voltammogram of monometallic Pt is observed at about 0.71 V_{RHE}, which is related to the lower coordinated Pt atoms according to the literature [94-97]. The corresponding tail becomes smaller for the PtAu5 sample and then vanishes for PtAu10 and PtAu20 samples which might indicate that Au atoms are preferably located at coordinatively-unsaturated sites [98-100].

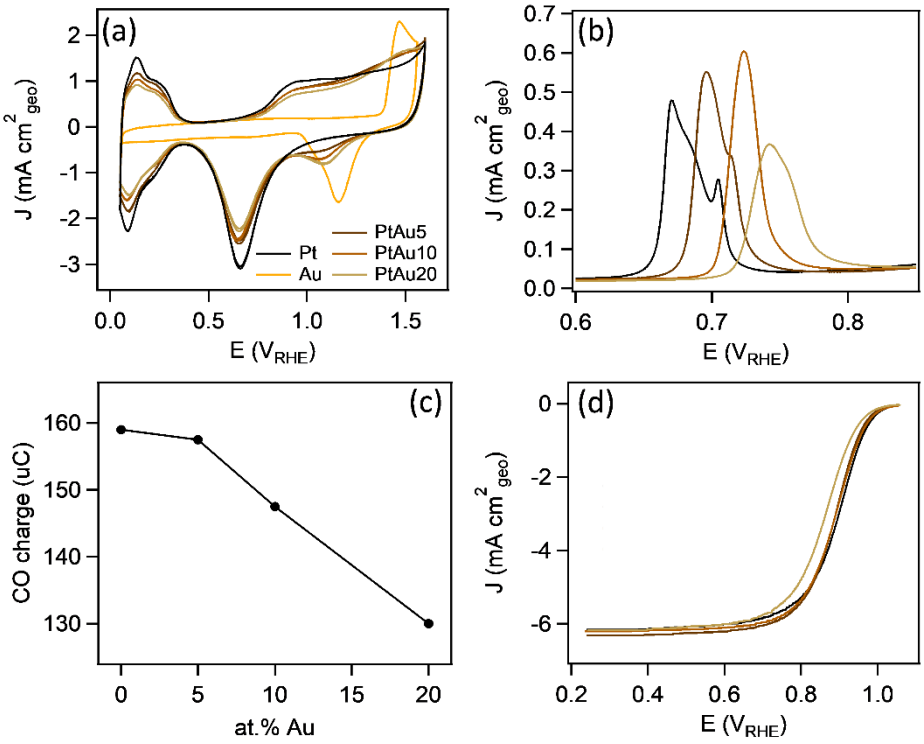

Fig. 3.6. *(a) Cyclic voltammograms of the as-deposited monometallic Pt and Au as well as Pt–Au alloy catalysts recorded in N_2-saturated 0.1 M $HClO_4$ solution; (b) CO-stripping voltammograms of the as-deposited monometallic Pt and Pt–Au alloy catalysts captured in CO-saturated 0.1 M $HClO_4$ solution; (c) Evolution of CO-stripping charge calculated from the voltammograms shown in (b); (d) ORR polarization curves of the as-deposited monometallic Pt and Pt–Au alloy catalysts recorded in O_2-saturated 0.1 M $HClO_4$ solution at 1600 rpm rotating speed and 20 mV s^{-1} scan rate.*

ORR polarization curves of Pt–Au catalysts, obtained in O_2-saturated 0.1M $HClO_4$ electrolyte, are depicted in Fig. 3.6d. The activity was first analyzed by calculating half-wave potential ($E_{1/2}$) from corresponding curves. The obtained values of $E_{1/2}$ for all investigated catalysts are summarized in Table. 3.2. It can be observed

that PtAu5 and PtAu10 catalysts show nearly similar ORR activity with monometallic Pt ($E_{1/2}$ ~ 0.9 V_{RHE}), indicating that 5 and 10 at.% of Au have a negligible impact on the ORR activity of Pt. In contrast, the ORR activity of the PtAu20 catalyst is significantly lower as its half-wave potential negatively shifts by about 40 mV ($E_{1/2}$ = 0.86 V_{RHE}).

Table. 3.2. *Kinetic parameters obtained from the ORR polarization curves.*

Samples	$E_{1/2}$ (V_{RHE})	J_k at 0.9 V_{RHE} ($mA \cdot cm^{-2}_{geo}$)	SA at 0.9 V_{RHE} ($mA \cdot cm^{-2}$)
Pt	0.90	5.6	2.9
PtAu5	0.89	4.7	2.5
PtAu10	0.89	4.6	2.6
PtAu20	0.86	2.4	1.5

To get more insights into the ORR activity of Pt–Au alloys, kinetic current density J_k values at 0.9 V_{RHE} were calculated using the Koutecky-Levich equation. The obtained values of J_k for all investigated catalysts are summarized in Table. 3.2. Again, it can be seen that no critical decrease of J_k occurs for PtAu5 and PtAu10 with respect to the one for monometallic Pt, while for PtAu20, it dropped by almost 50 %. The specific activity (SA) was further calculated using corresponding J_k normalized by the Pt surface area calculated from the CO stripping measurements in Fig. 3.6b and c. SA values are summarized in Table. 3.2 and follow the same trend as $E_{1/2}$ and J_k. Based on the above results we can conclude that Pt retains its activity when alloyed with 5 and 10 at.% of Au, while 20 at.% already has a detrimental effect on its ORR activity.

3.1.4. Effect of Au on the stability of Pt–Au alloy catalysts

After careful analysis of the ORR activity of Pt–Au alloys, their stability was tested. Particularly, *in situ* SFC coupled to ICP-MS was applied to examine the influence of alloying with Au on Pt dissolution during electrochemical cycling. The samples were cycled from 0.05 V_{RHE} to different upper potential limits (UPL): 1.2 and 1.5 V_{RHE} in N_2-saturated 0.1M $HClO_4$ electrolyte. More details can be found in the experimental section. Unfortunately, the resolution of ICP-MS did not allow us to use 1 V_{RHE} UPL. However, considering prior research on Pt@Au core-shell nanoparticles, which demonstrated the effect of Au in stabilizing Pt dissolution within the range of 1 to 1.2 V_{RHE}, we propose that our findings may be extended to lower upper potentials

as well [70]. Fig. 3.7 shows the applied electrochemical protocol and corresponding Pt and Au dissolution profiles for all investigated samples. For clarity, the cycle to 1.2 V_{RHE} is highlighted with a green background, while the cycle to 1.5 V_{RHE} is highlighted with a red background. It is important to specify that Pt and Au dissolution profiles here are normalized by the relative atomic ratio of Pt and Au on the outermost surface of catalysts calculated from CO-stripping voltammograms (see Fig. 3.6b and c).

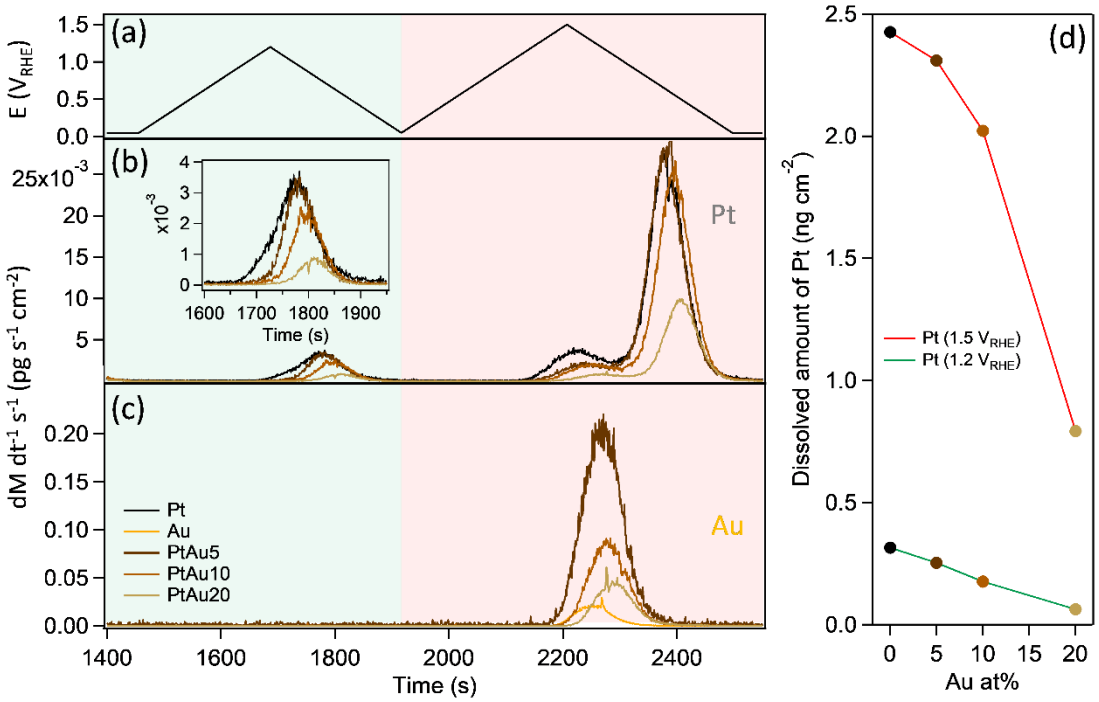

Fig. 3.7. *(a) The applied potential protocol; Corresponding Pt (b) and Au (c) dissolution mass-spectrogram acquired from Pt–Au alloy catalysts and monometallic (Pt, Au) electrodes; (d) Normalized Pt dissolution amount calculated by integration of corresponding mass-spectrogram shown in (b).*

When the UPL is set to 1.2 V_{RHE}, a single dissolution peak is observed in Pt dissolution profiles shown in Fig. 3.7b. This peak includes both anodic and cathodic scans, which are hard to resolve. The anodic Pt dissolution is explained by the formation of unstable surface Pt species in the oxide formation region, while cathodic dissolution is attributed to the dissolution of Pt in the oxide reduction region [101]. Nevertheless, a clear shoulder can be distinguished on the left side of the peak for monometallic Pt, which can be better observed in the inset of Fig. 3.7b. This shoulder can be assigned to the anodic dissolution of platinum. Interestingly, this shoulder vanishes for Pt–Au alloys, and the dissolution curves contain cathodic peaks only,

evidencing that the presence of Au suppresses Pt anodic dissolution. Furthermore, the intensity of the cathodic dissolution peak decreases as the Au concentration rises, suggesting that the addition of Au suppresses cathodic dissolution as well. The ratio between anodic and cathodic dissolution is calculated and summarised in Fig. 3.8 (black line).

Simultaneously with the above observation, the onset potential of Pt dissolution positively shifts with Au content increasing, which is another evidence that an increase in Au content results in inhibition of the Pt dissolution. The quantified total dissolution of Pt obtained by integrating corresponding dissolution profiles for all investigated samples is summarised in Fig. 3.7d (green line). It can be observed that it significantly decreases as Au concentration increases. Overall, Pt dissolution is suppressed by 20, 45, and 80 % for PtAu5, PtAu10, and PtAu20 samples, respectively, with respect to the monometallic Pt. Considering Au dissolution, the potential of 1.2 V_{RHE} is not sufficient to oxidize Au and initiate its dissolution, as can be seen in Fig. 3.7c [102].

When the UPL is set to 1.5 V_{RHE}, the Pt dissolution profile consists of well-resolved anodic (the lower peak) and cathodic (higher peak) peaks [103]. Similar trends can be observed here, as in the case of 1.2 V_{RHE} UPL. The onset potential of Pt dissolution positively shifts for both anodic and cathodic dissolution peaks with Au content increasing and Pt dissolution decreases in both anodic and cathodic scans with an increased Au content. In contrast to 1.2 V_{RHE} UPL, the anodic peak does not disappear completely. However, the nearly twofold decrease of the anodic peak with respect to the cathodic peak can be observed in the calculated ratio, as shown in Fig. 3.8, suggesting that the presence of Au has a more pronounced impact on the anodic dissolution of Pt. The quantified total dissolution of Pt is summarised in Fig. 3.7d (red line). Overall, Pt dissolution in the case of 1.5 V_{RHE} UPL is suppressed by about 7, 27, and 67 % for PtAu5, PtAu10, and PtAu20, respectively, with respect to the monometallic Pt.

In contrast to 1.2 V_{RHE}, the 1.5 V_{RHE} UPL is sufficient to initiate also Au dissolution, as evidenced by the presence of Au dissolution peaks in Fig. 3.7c. Similar to Pt dissolution at 1.2 V_{RHE} UPL, the anodic and cathodic dissolution peaks of Au correlate together as one peak. The Au dissolution rate decreases with the decrease of Pt content, reaching its lowest point for monometallic Au (note that the dissolution rate here is normalized to the amount of Au on the surface). This behavior is probably

attributed to the fact that Au is less stable when alloyed with Pt, mainly because Pt itself is less stable.

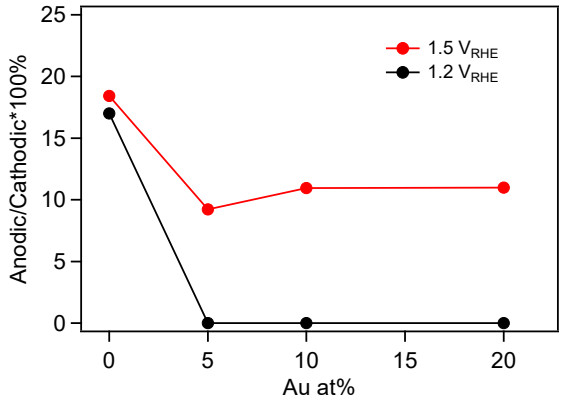

Fig. 3.8. *The ratio of anodic to cathodic Pt dissolution peaks for Pt–Au alloy catalysts at 1.2 and 1.5 V_{RHE} UPL.*

Overall, summarizing our experimental results, we can conclude the negative effect of Au on the ORR activity and a positive influence on the stabilization of Pt in terms of inhibiting its dissolution. The precise catalyst engineering and thorough characterization allowed us to investigate the composition–activity–ability relationship in detail. While stability was found to improve continuously with the increase of the amount of Au, the ORR activity exhibited threshold behavior, with the threshold falling somewhere between 10 and 20 at.% of Au. Below this value, Pt retains its activity, while above it, the activity experiences a significant drop. PtAu10 with 10 at.% of Au can be concluded as an optimal Pt–Au composition since it still shows acceptable activity, and its stability increased by almost 50 % at 1.2 V_{RHE} UPL and by almost 30 % at 1.5 V_{RHE} UPL.

The above conclusions are in good agreement with previously reported studies regarding the model Au/Pt system [104]. Lopes et al. found that Au coverage up to 0.2 ML on Pt(111) single-crystal surface shows significantly enhanced stability and a minimal impact on ORR activity [70], which was associated with the fact that Au atoms tend to preferentially locate at Pt(111) step-edge sites. Nevertheless, the ORR activity of the catalyst was found to decrease with a further increase in Au coverage as they started to occupy Pt terraces. Similar findings were reported by Kodama et al by modification of Pt single-crystal surface by depositing Au atoms selectively on (100) step sites [105].

Indeed, Pt atoms located in lower-coordinated positions, such as corner, edge, and step-edge, have weaker Pt-Pt binding strength due to reduced coordination number, which leads to atoms being more prone to dissolution than Pt atoms located in the higher-coordinated positions. For instance, it was reported that the dissolution rate trend follows Pt(110) > Pt(100) > Pt(111), corresponding to the coordination numbers 7, 8, and 9, respectively [101], indicating that Pt(111) has the highest stability among Pt(hkl) surfaces. On the other hand, ORR activity increases in the order Pt(100) ≪ Pt(111) ≈ Pt(110) [106]. Extrapolating the information provided above to our results, it can be suggested that Au atoms could preferentially be located at low-coordinated sites, as indicated by the CO-stripping results in Fig. 3.6b. When the amount of Au is sufficiently large, it begins to occupy Pt(111) sites, resulting in a significant drop in activity.

Monte Carlo (MC) simulations relying on density functional results were thus further applied to gain a further understanding of the composition-activity-stability relationship of the Pt–Au alloys under study. The Topological method (TOP) that combines Density functional theory (DFT) calculations of selected orderings with MC exploration of a huge configurational space of the possible ordering was applied [107, 108].

Fig. 3.9 depicts the lowest-energy topologies (atomic orderings) of 1463 atomic octahedral-like particles (estimated size about 4 nm) with the fcc structure calculated at temperature 300 K. The particles contain the increasing number of Au atoms on the surface: $Pt_{1434}Au_{29}$, $Pt_{1406}Au_{57}$, and $Pt_{1349}Au_{114}$, which refer to experimentally investigated compositions 5, 10, and 20, at.% Au in the surface layer. Additionally, we investigated the $Pt_{1291}Au_{172}$ particle, which corresponds to 30 at.% Au. The outermost atomic layer of corresponding particles contains 24 corners, 108 edges, and 440 (111) facet atoms. It is important to note that these simplified simulations do not take into account bulk Au atoms in the equilibrium chemical orderings of Au/Pt model particles.

On the one hand, Au atoms exhibit a pronounced energetic preference to be located in the outermost atomic layer of the particle only. On the other hand, they tend to favor corner and edge positions characterized by the lowest coordination numbers. Specifically, the Au atom is ≥ 0.5 eV more stable in the corner and edge than inside the particle, and they are approximately 0.3–0.4 eV more stable when located at the (111) terrace position than inside the particle. Based on the above, in the case of $Pt_{1434}Au_{29}$ particles corresponding to 5 % of Au atoms in the outermost layer, Au

occupies 4 of 24 corner positions and 25 of 108 edge positions at equilibrium. In the case of $Pt_{1406}Au_{57}$ particle with 10 % of Au atoms in the outermost layer, Au atoms also occupy exclusively low-coordinated Pt atoms in the corner and edge sites. Still, we did not observe any decrease in the number of active Pt atoms in (111) nanofacets. However, when Au surface content increased to 20 % ($Pt_{1349}Au_{114}$), we already observed the appearance of a few Au atoms in the (111) terraces. At 30 % of surface Au ($Pt_{1291}Au_{172}$), corner or edge sites are completely filled by Au atoms, and 40 Au atoms are already located in (111) terrace sites. Such a decrease of an active for ORR (111) Pt sites explains the detrimental effects of Au on the ORR activity of the Pt–Au system. The above modeling is almost in line with the experimental results and points to the existence of a threshold in Pt–Au composition, after which its ORR activity decreases notably.

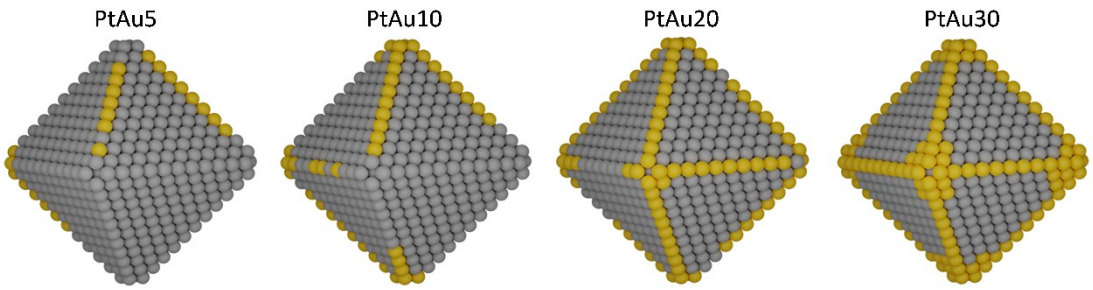

Fig. 3.9. *Equilibrium chemical orderings of ca. 4.4 nm large Pt–Au particles with Au content in the outer atomic shell for 5, 10, 20 and 30 at.% calculated at temperature 300 K: $Pt_{1434}Au_{29}$ (corner-4, edge-25, terrace-0), $Pt_{1406}Au_{57}$ (12, 45, 0), $Pt_{1349}Au_{114}$ (23, 89, 2) and $Pt_{1291}Au_{172}$ (24, 108, 40). Atom color coding: Pt – grey; Au – yellow.*

Additionally, DFT calculations were performed to determine the relative stability of Pt atoms placed at the corner, edge, and surface terrace positions in the case of the truncated-octahedral Pt_{405} particle using the protocol described in ref [109]. The results showed that Pt atoms placed at the inner (111) terrace are by almost 1 eV more stable than Pt atoms at corner sites and by 0.6–0.9 eV more stable than other surface Pt atoms placed outside the (111) terraces. These observations agree well with the ICP-MS results described above. The decrease of low-coordinated surface Pt atoms or their complete absence because of substitution by more inert metal Au atoms decreases Pt dissolution compared with monometallic Pt nanoparticles, which contain numerous exposed low-coordinated Pt atoms.

Nevertheless, the above theoretical results do not provide a complete description of our Pt–Au catalysts. Apart from the presence of Au atoms on the surface, it is essential to consider the electronic and geometric effects of Au atoms in the bulk, which have been quantified through SRPES and XRD measurements, since they are also reported to have a detrimental influence on the Pt–Au ORR activity. This can account for the disparity between the aforementioned modeling and earlier reports on the Au/Pt system, which suggested that ORR activity is maintained up to 20 % of Au on the Pt surface, whereas our results demonstrated a significant drop in activity at this level.

3.1.5. Activity and stability of Pt–Au alloy catalysts during potentiodynamic cycling in a half-cell.

The Pt dissolution behavior was further tested during continuous 500 potentiodynamic cycles using SFC-ICP-MS. Results from *in situ* mass spectroscopy are summarized in Fig. 3.10, where the Pt dissolution rate is plotted together with applied potential protocol as a function of time during potentiodynamic cycling from 0.05 to different UPL of 1, 1.2 and 1.5 V_{RHE} with 500 mV s^{-1} scan rate in N_2-saturated 0.1 M $HClO_4$ for all investigated samples. The dissolution data are normalized by the relative Pt concentration on the sample surface based on CO-stripping data in Fig. 3.6.

All Pt mass spectrograms, regardless of the UPL, contain a so-called contact dissolution peak, which usually occurs after contacting the sample with SFC prior to initiating cycling voltammetry. This peak is attributed to the dissolution of surface oxides present on the sample surface due to its exposure to air when it is transferred from the deposition chamber [110]. Notably, it can be already seen that this contact dissolution peak is much smaller for Pt–Au alloys than for monometallic Pt, which is in line with the results presented above. During potentiodynamic cycling to 1.0 $V_{RHE,}$ (Fig. 3.10a), almost no dissolution of Pt was detected because as mentioned above the resolution of ICP-MS is not enough for the detection of a very small amount of dissolved Pt expected at these conditions [111, 112]. When the upper potential limit was increased to 1.2 V_{RHE} (Fig. 3.10b), continuous Pt dissolution was observed throughout the entire cycling procedure. Moreover, a clear trend is evident in both the Pt dissolution rate and the increase in Au content in Pt–Au alloys i.e. the increase in Au content significantly suppresses the total Pt dissolution. At 1.5 V_{RHE} UPL

(Fig. 3.10c), the trend in Pt dissolution is similar, with only an overall higher dissolution rate.

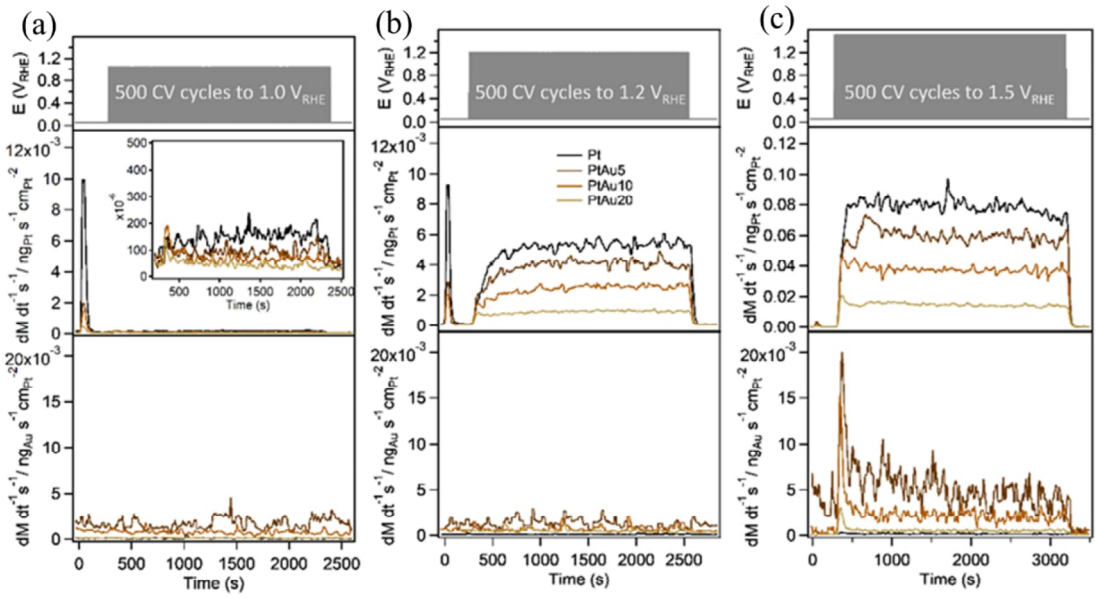

Fig. 3.10. *Applied potential protocol (upper row) together with representative platinum (middle row) and gold (bottom row) dissolution mass spectrograms taken from monometallic Pt and Pt–Au alloy catalysts during 500 potentiodynamic cycles to different upper potential limits: (a) 1.0 V_{RHE}, (b) 1.2 V_{RHE}, and (c) 1.5 V_{RHE}.*

Corresponding Au mass spectrograms did not show any dissolution when samples were cycled to 1 and 1.2 V_{RHE} UPL because these potentials are insufficient to initiate Au oxidation/dissolution (see Figs. 3.10a and b). At 1.5 V_{RHE} UPL Au dissolution was detected for all Pt–Au alloys (Fig. 3.10c). The most significant Au dissolution occurred at the initial stages of the cycling, although it persisted above the baseline until the end of the potential cycling. This dissolution behavior could indicate a preferential Au dissolution at the beginning of the cycling procedure, while Pt exhibited a more continuous dissolution throughout the entire process.

The stability of the Pt–Au catalysts was further evaluated in the half-cell RDE system during so-called accelerated degradation tests (ADT) consisting of 2000 CV cycles from 0.05 to 1 V_{RHE}, 1.2 V_{RHE} and 0.05 to 1.5 V_{RHE} with 500 mV s^{-1} scan rate in N_2-saturated 0.1 M $HClO_4$, denoted as ADT (1 V_{RHE}), ADT (1.2 V_{RHE}) and ADT (1.5 V_{RHE}), respectively. While the former simulates the normal conditions that the catalyst experiences in a real PEMFC device, the latter two simulate much harsher ones occurring during startup/shutdown cycles, as mentioned in the Introduction part.

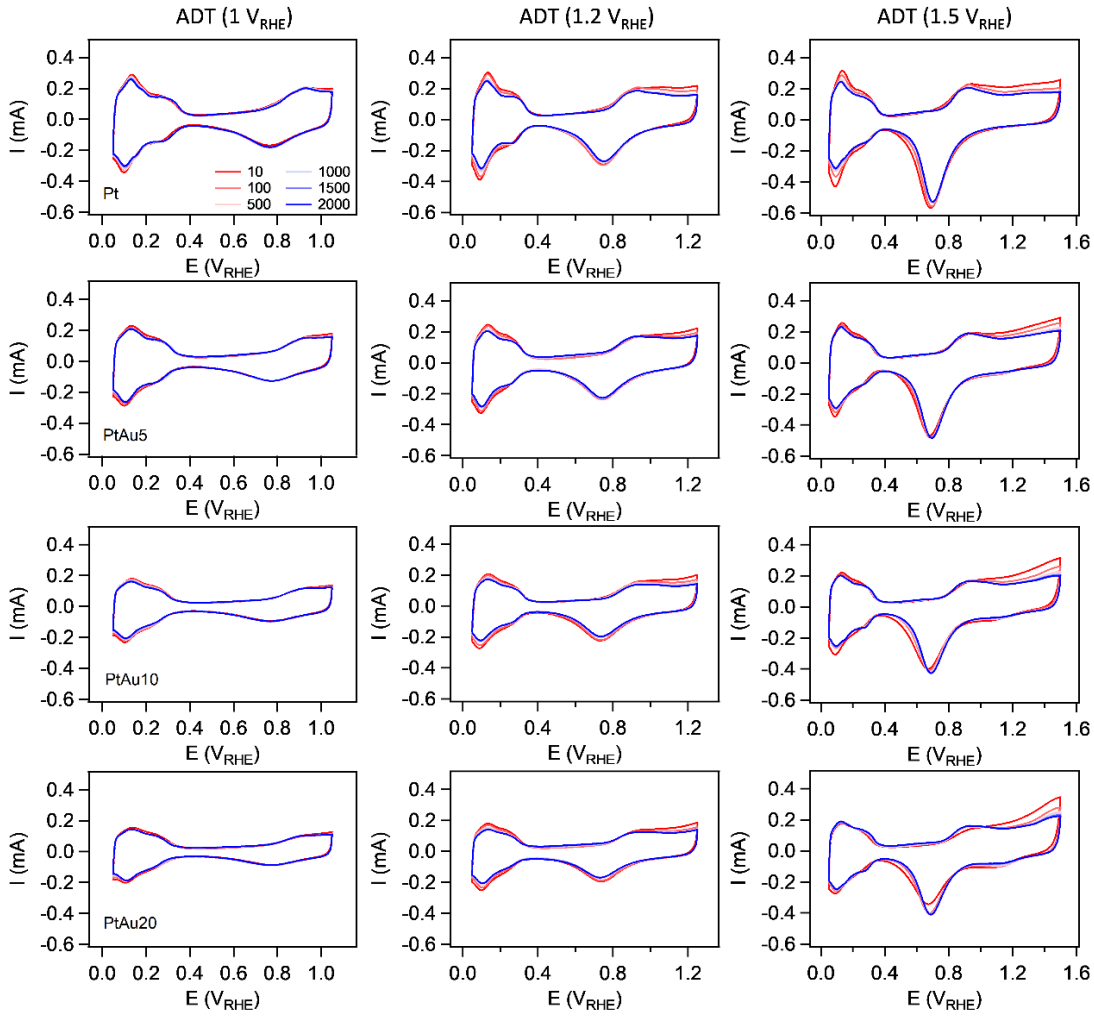

Fig. 3.11. *Selected CVs of monometallic Pt and Pt–Au alloy catalysts acquired during ADT (1 V_{RHE}) (left column), ADT (1.2 V_{RHE}) (middle column), and ADT (1.5 V_{RHE}) (right column).*

The sets of selected CVs for monometallic Pt and Pt–Au alloys under study during ADT (1 V_{RHE}), ADT (1.2 V_{RHE}), and ADT (1.5 V_{RHE}) are shown in Fig. 3.11. It can be qualitatively observed from corresponding CVs that they almost persist its shape during the entire ADT (1 V_{RHE}), indicating very low if any catalyst degradation at this protocol. In contrast, during ADT (1.2 V_{RHE}), cyclic voltammograms exhibit irreversible change with an increasing number of cycles, manifested by the decrease of H_{UPD}, which serves as direct evidence of the reduction in Pt active sites on the catalyst surface due to its coarsening. With a further increase of the upper potential to 1.5 V_{RHE}, the changes in CVs of the monometallic Pt become even more pronounced with respect to those obtained when the upper potential was set to 1.2 V_{RHE}. However, the CVs showed more stable behavior for Pt–Au alloys than for monometallic Pt.

The CO stripping charge calculated from CO-stripping voltammograms measured before and after each ADT (not shown herein) is shown in Fig. 3.12 and was further used to follow changes in active surface area during ADTs quantitatively.

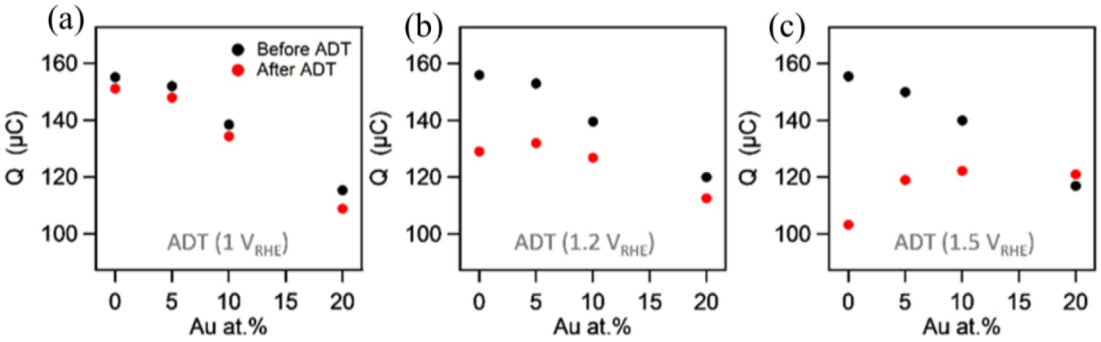

Fig. 3.12. *CO stripping charge values calculated for monometallic Pt and Pt–Au alloy catalysts before and after (a) ADT (1 V_{RHE}), (b) ADT (1.2 V_{RHE}), and (c) ADT (1.5 V_{RHE}).*

It can be seen that at ADT (1 V_{RHE}), there is no significant decrease in CO-stripping charge during the entire cycling procedure for all investigated samples except for the PtAu20 sample, where the decrease is more obvious (Fig. 3.12a). The CO-stripping charge decreased by about 3 % for Pt, PtAu5, PtAu10, and about 6 % for PtAu20. It is in line with SEM images in Fig 3.13, which do not show any substantial changes in morphology for all samples after ADT (1 V_{RHE}). In contrast, during ADT (1.2 V_{RHE}), the active surface area of monometallic Pt decreased significantly, reaching about 17 % loss (Fig. 3.12b). Nevertheless, Pt–Au samples exhibited much better stability. The degradation was less pronounced with an increasing amount of Au in Pt–Au alloys. The active surface area of PtAu5, PtAu10, and PtAu20 decreased by 14, 9, and 6 %, respectively.

The dramatic decrease of CO stripping charge for monometallic Pt occurred upon cycling to devastating 1.5 V_{RHE}, where it decreased by approximately 35 % (Fig. 3.12c). This substantial reduction can be attributed to the strong catalyst coarsening, as demonstrated in the SEM images presented in Fig. 3.13, and is in good agreement with the literature [26, 113]. Nevertheless, at ADT (1.5 V_{RHE}), the effect of Au in the stabilization becomes even more pronounced with respect to the one described above for ADT (1.2 V_{RHE}). It can be seen, even from SEM images, that an increase in the Au content results in less significant morphological changes on the catalyst surface

following ADT. The CO-stripping charge for PtAu5 and PtAu10 decreased by 20 % and 12 %, respectively. Interestingly, the PtAu20 sample even showed a slight increase of approximately 3 % in CO-stripping charge after ADT (1.5 V_{RHE}).

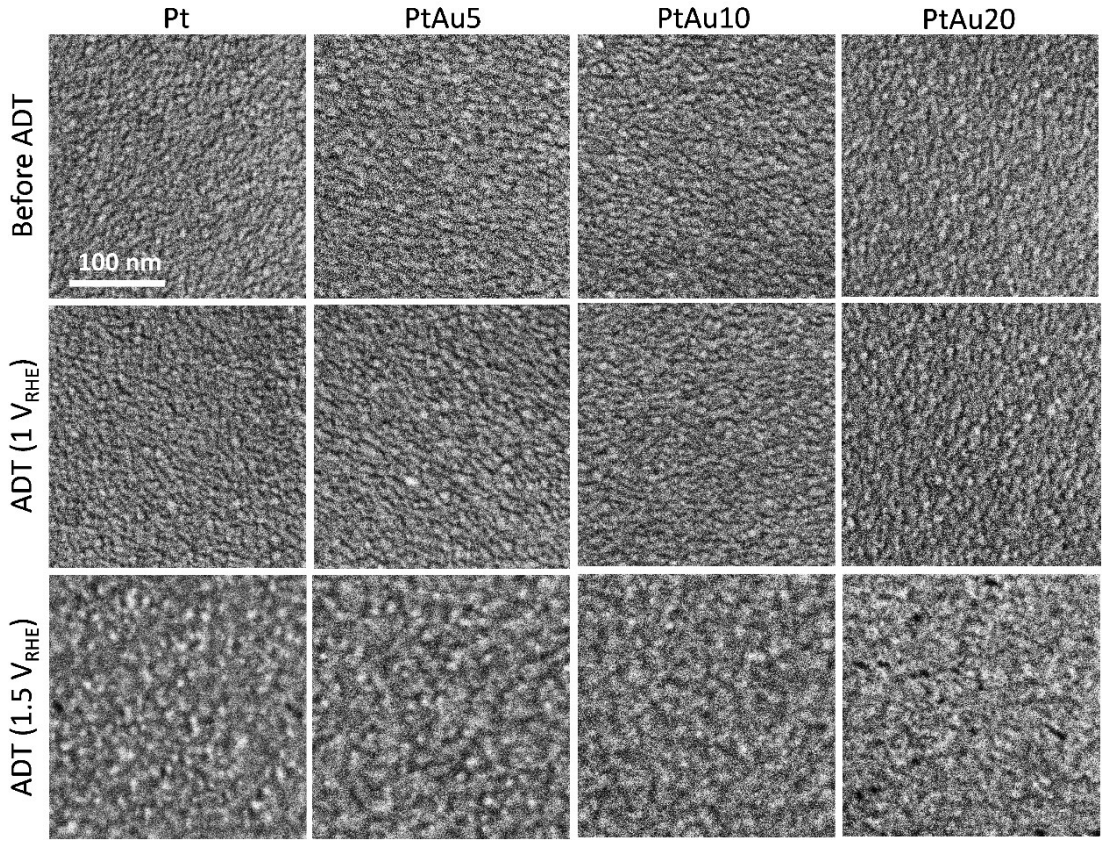

Fig. 3.13. *SEM images of monometallic Pt and Pt-Au alloy catalysts captured before (upper row) and after ADT (1 V_{RHE}) (middle row) and ADT (1.5 V_{RHE}) (bottom row).*

The observed increase in CO-stripping charge for the PtAu20 sample cycled to 1.5 V_{RHE} may indicate surface restructuring (Pt enrichment on the surface of the Pt–Au alloy) occurs alongside catalyst coarsening during ADT, which requires further investigation. As the most surface-sensitive technique, cyclic voltammograms can provide valuable qualitative information about the Pt–Au surface composition. Fig. 3.14 represents a comparison of CVs acquired before and after ADTs for all examined samples. In the case of ADT (1.5 V_{RHE}), all recorded CVs already exhibit Au and Pt reduction peaks, enabling the monitoring of surface compositional changes in the Pt–Au alloy. In turn, for ADT (1 V_{RHE}) and ADT (1.2 V_{RHE}), additional CVs with extended potential ranges (0.05–1.6 V_{RHE}) were recorded before and after cycling. It can be qualitatively observed from CVs in Fig 3.14 left and middle row that cycling

to 1 and 1.2 V_{RHE} leads to Au enrichment, indicated by an increase in the Au reduction peak and a decrease in the Pt reduction peak (highlighted by arrows). On the contrary, after ADT (1.5 V_{RHE}), clear Pt enrichment is evident, as the intensity of the CV peak representing Pt increases, while that of Au decreases (see Fig. 3.14 right row).

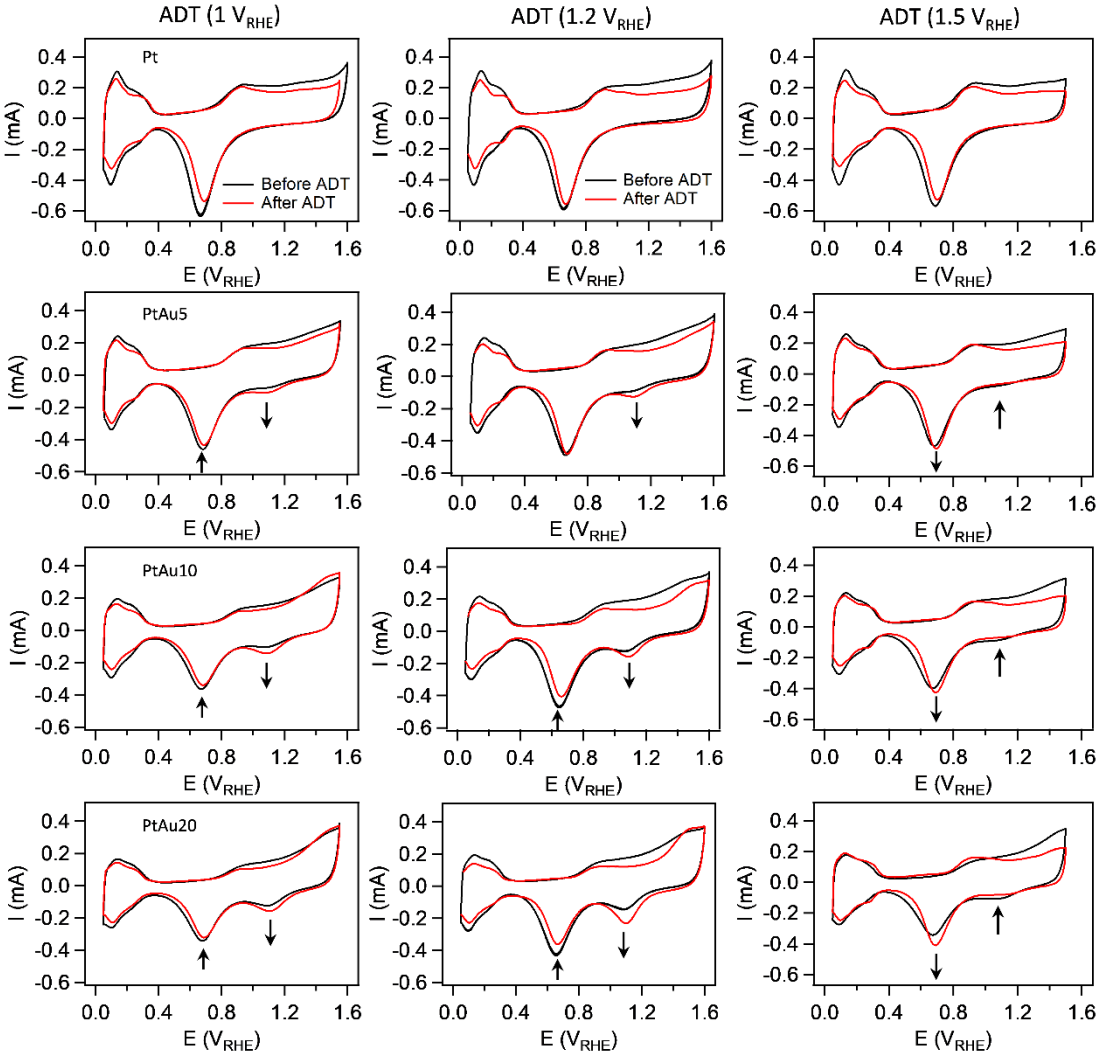

Fig. 3.14. *Cyclic voltammograms of monometallic Pt and Pt–Au alloy catalysts acquired before and after ADT (1 V_{RHE}) (left column), ADT (1.2 V_{RHE}) (middle column), and ADT (1.5 V_{RHE}) (right column).*

The surface compositional change observed on CVs was further confirmed using the SRPES technique for selected samples and ADTs. Fig. 3.15 shows the SRPES Au 4f and Pt 4f spectra captured before and after ADT (1 V_{RHE}) and ADT (1.5 V_{RHE}) for PtAu5 and PtAu10 samples. The spectra are normalized to Pt 4f core levels to better visualize changes in Au concentration. It can be observed that

ADT (1.5 V_{RHE}) leads to Pt enrichment on the surface of Pt–Au alloy for both samples, which is in line with CV results in Fig. 3.14. However, we did not observe an Au enrichment in the case of ADT (1 V_{RHE}). Probably at these conditions, restructuring occurs predominantly in the outermost layer of the alloy, and the SRPES technique with about 3 monoatomic layer information depth is not sensitive enough to capture those changes.

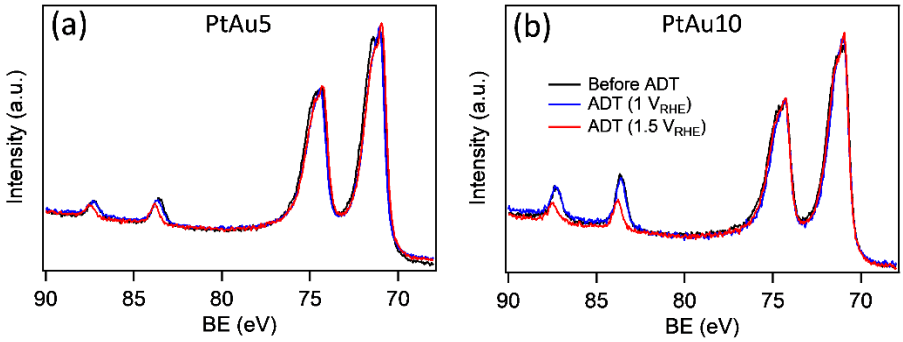

Fig. 3.15. *SRPES Pt 4f and Au 4f spectra of (a) PtAu5 and (b) PtAu10 samples acquired before and after ADT (1 V_{RHE}) and ADT (1.5 V_{RHE}).*

Several factors may contribute to the above enrichment behavior. Firstly, the significant difference in oxidation potentials between Pt and Au. Pt has a lower oxidation potential, and thus, Pt may preferentially dissolve during ADT (1 V_{RHE}) and ADT (1.2 V_{RHE}), leading to the exposure and enrichment of Au atoms on the alloy surface. This is substantiated by the results of ICP-MS shown in Fig. 3.10b, where we observed the dissolution of Pt upon cycling to 1.2 V_{RHE}, while Au did not dissolve. On the other hand, during ADT (1.5 V_{RHE}), dissolution of both Pt and Au occurs (Fig. 3.10c), but since the concentration of Au is much lower than Pt, it can lead to the exposure and enrichment of Pt atoms on the alloy surface. Indeed, in the Au dissolution spectrograms presented in Fig. 3.10c, we observed a more pronounced Au dissolution at the initial stages of the cycling, which then sharply decreased as the cycling continued.

However, in contrast to the SFC-ICP-MS setup where the solution is continuously pumped above the sample to ICP-MS to detect dissolved ions, in the RDE experiment, dissolved Pt and Au ions are known to redeposit back on the surface, which makes the above interpretation of Pt or Au enrichments on the surface of Pt–Au

alloys not so straightforward. The possibility of segregation phenomena cannot be ruled out as well.

At thermodynamic equilibrium, Au tends to segregate on the Pt surface in the case of Pt–Au alloy due to its lower surface energy [114]. However, it is important to note that this segregation behavior can be influenced by multiple other factors, including the initial alloy composition, specific electrochemical environment, applied potential, etc., that may further complicate the interpretation of this phenomenon [115-117]. Indeed, Papaefthimiou et al. using near-ambient-pressure photoelectron spectroscopy observed changes in the Pt and Au distribution in the near-surface region as a result of interface polarization [114]. It is important to note that both of these mechanisms are not straightforward, and second, they could co-occur during potentiodynamic cycling, which represents significant challenges in the interpretation of the Pt and Au enrichments discussed above. Further research and investigation are required to gain a deeper understanding of the processes involved and to provide more definitive insights into these enrichments.

The above-described surface restructuring during ADT may seriously influence the ORR activity of investigated Pt–Au alloys. To investigate that, ORR polarization curves were compared for all investigated samples before and after ADT (1 V_{RHE}) and ADT (1.5 V_{RHE}). The results are summarized in Fig. 3.16. Additionally, the values of kinetic current density and specific activity extracted from the corresponding voltammograms are summarized in Table 3.3. It can be observed that during ADT (1 V_{RHE}), both monometallic Pt and PtAu5 alloy did not experience a significant loss in their ORR activity. The kinetic current decreased by approximately 7% for both. A more pronounced decrease in the ORR activity was observed for the PtAu10 sample, manifested by a slight shift in the polarization curve to lower potentials and corresponding decrease of kinetic current by almost 20 %, from 4.62 to 3.71 $mA \cdot cm^{-2}_{geo}$. The PtAu20 sample exhibited a notable performance decrease, with the J_k value dropping by more than half. Considering that a decrease in ORR activity is not expected during 2000 CV cycles to 1 V_{RHE}, and indeed, we did not observe any catalyst coarsening in SEM images before and after ADT, we can assume that the slight decrease in ORR activity for PtAu10 and the significant decrease for the PtAu20 sample are solely related to surface Au enrichment, as observed in Fig. 3.16. This Au surface enrichment is also responsible for a slightly higher decrease in CO-stripping charge for the PtAu20 sample at ADT (1 V_{RHE}) shown in Fig. 3.12a.

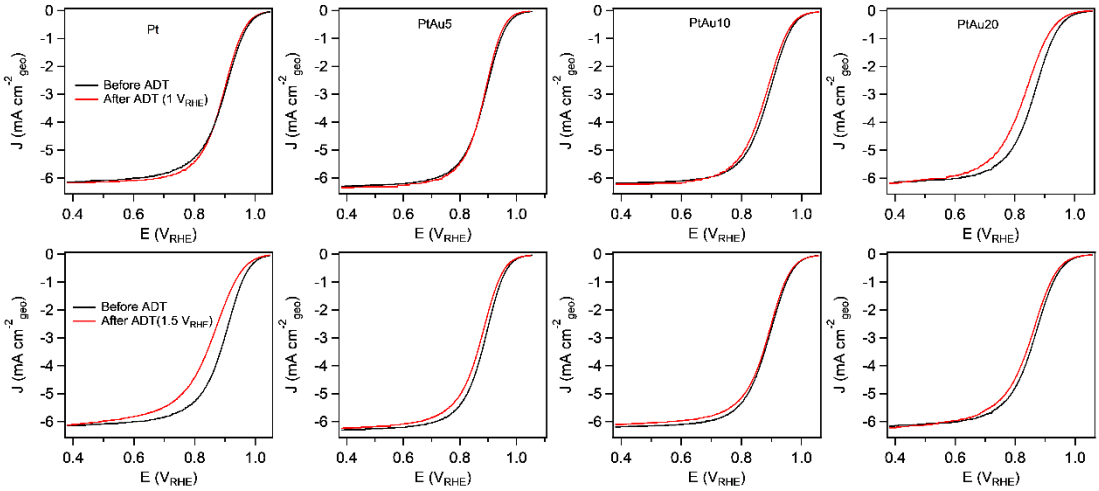

Fig. 3.16. *ORR polarization curves recorded over monometallic Pt and Pt–Au alloy catalysts in O_2-saturated 0.1M $HClO_4$ electrolyte at 1600 rpm rotating speed and 20 mV s^{-1} scan rate before and after ADT (1 V_{RHE}) (upper row) and ADT (1.5 V_{RHE}) (bottom row).*

Table. 3.3. *Kinetic parameters obtained from the ORR polarization curves after ADT.*

	J_k, 0.9 V (mA·cm$^{-2}_{geo}$)				SA, 0.9 V (mA·cm$^{-2}_{Pt}$)			
Sample	Pt	PtAu5	PtAu10	PtAu20	Pt	PtAu5	PtAu10	PtAu20
Before ADT	5.63	4.73	4.62	2.43	2.90	2.50	2.60	1.50
ADT (1 V_{RHE})	5.21	4.42	3.71	1.09	2.84	2.46	2.27	0.82
ADT(1.5 V_{RHE})	2.20	3.62	4.28	1.90	1.75	2.50	2.88	1.28

During ADT (1.5 V_{RHE}) the expected significant decrease in ORR activity was observed for monometallic Pt (60 % decrease in J_k), which coincides with the strong catalyst coarsening observed by SEM in Fig. 3.13. In the case of the Pt–Au catalysts, the decrease in ORR activity was significantly lower. The kinetic current value dropped by 23, 7 and 20 % for PtAu5, PtAu10 and PtAu20, respectively. Despite still relatively significant morphological changes during ADT (1.5 V_{RHE}) for PtAu5 and PtAu10 (see Fig. 3.13), we anticipate that the catalyst coarsening is counterbalanced by Pt enrichment discussed above, resulting in a lower decrease of ORR activity.

3.1.6. Activity and stability of Pt–Au alloy catalysts in PEMFC

Pt–Au catalysts prepared by magnetron sputtering were further tested in a single-cell. For testing in a real fuel cell device, monometallic Pt, as well as PtAu5, PtAu10, and PtAu20 catalysts with an identical thickness of approximately 50 nm,

were deposited onto a commercial nGDL electrode. The nGDL with the deposited catalyst layer was used as the cathode part, while a commercial catalyst with Pt loading of 0.3 mg·cm^{-2} was used as the anode part of PEMFC. Polarization curves, together with the power density (PD) characteristics of such a single cell, are presented in Fig. 3.17a for all investigated cathode catalysts.

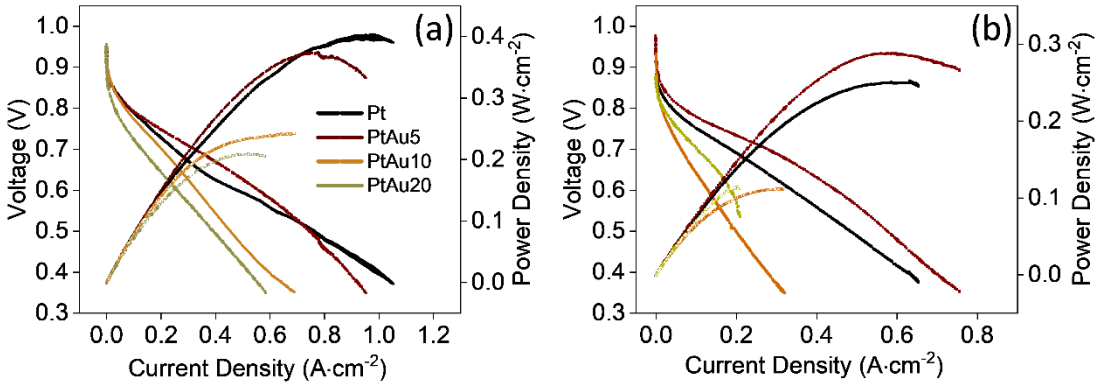

Fig. 3.17. *Single-cell performances of monometallic Pt and Pt–Au alloys as a cathode at 80 °C with fully humidified H_2 and O_2. Polarization curves (left Y-axis), together with the power density characteristics (right Y-axis) recorded (a) before and (b) after ADT.*

The PtAu5 catalyst shows a maximum power density of 0.37 W·cm^{-2}, which is comparable to that of Pt (0.4 W·cm^{-2}). Interestingly, PtAu10 and PtAu20 catalysts showed significantly lower maximum power densities of 0.24 and 0.2 W·cm^{-2}, respectively. The inconsistency with half-cell experiments could be explained by the transition from an idealized liquid-based half-cell configuration to the more complex real single-cell configuration where multiple factors can influence catalyst activity, such as the presence of solid polymers, working conditions including flow rate, humidity, pressure, and temperature, as well as break-in conditions, etc. Indeed, most of nowadays achievements have been focused on the RDE experiments in half-cells and significant discrepancies have been observed in the catalytic activities when measured in single-cells [118]. Recognizing the differences in the electrochemical performances between half-cells and full-cells as well as the adaptation of promising catalysts from half-cell experiments to membrane electrode assemblies in single-cells are thus of utmost importance in current research.

We further performed ADTs in a single-cell. The ADT protocol here followed the standard procedure according to the US Fuel Cell Council, which consisted of 30,000 potential cycles[78]. During each cycle, the potential was held at 0.6 V and 0.95 V for 3 seconds. Polarization curves, along with power density characteristics of such single-cells after ADT, are plotted in Fig. 3.17b for all investigated catalysts. After ADT, the PtAu5 catalyst exhibited a higher maximum power density (0.29 $W \cdot cm^{-2}$) than Pt (0.25 $W \cdot cm^{-2}$). Comparing the PD values before ADT, PtAu5 catalyst experienced approximately 20 % performance loss, while Pt showed about 38 % loss. At the same time, PtAu10 and PtAu20 experienced an unacceptable reduction in power density. Based on the above results in a single-cell configuration, the PtAu5 catalyst can be considered optimal in terms of the activity-stability relationship. However, the results obtained in single-cell tests differ from those in half-cell experiments, where $Pt_{90}Au_{10}$ was found to be the optimal Pt–Au composition in terms of activity and stability. It can be assumed that the complex conditions within a real PEMFC device may not only compromise catalyst activity, as mentioned earlier but also influence the restructuring behavior of the bimetallic alloy during ADT described in the previous chapter, which can further affect the overall performance of the PEMFC. Nevertheless, the results described in this chapter still confirm the significant stabilizing effect of Au within the Pt–Au alloy, showcasing the versatility of Au in enhancing the overall durability of the cathode catalyst not only in the idealized liquid-based half-cell configuration but in real-world PEMFC applications.

3.1.7. Conclusions

In this chapter, we reported a systematic study of the Pt–Au ORR catalysts with various compositions. $Pt_{95}Au_5$, $Pt_{90}Au_{10,}$ and $Pt_{80}Au_{20}$ alloys were prepared using a magnetron sputtering technique. Complementary characterization techniques, electrochemistry, and computational modeling were applied to gain a comprehensive understanding of the Pt–Au composition-activity-stability relationship.

It was shown that PtAu5 and PtAu10 catalysts retain the ORR activity of monometallic Pt, while the PtAu20 catalyst experienced a nearly twofold reduction in ORR activity. Considering stability, it was demonstrated that, compared to monometallic Pt, Pt dissolution decreased by 20 %, 45 % and 80 % for PtAu5, PtAu10, and PtAu20 samples, respectively, when using an upper potential limit of 1.2 V_{RHE}. Similarly, the suppression percentages were 10 %, 20 % and 65 % when

employing an upper potential limit of 1.5 V_{RHE}. Overall, the obtained results highlight Pt–Au catalyst with 10 % gold as the most suitable composition, retaining the activity of monometallic Pt while effectively suppressing Pt dissolution. Although PtAu20 demonstrates better stability, its poor ORR activity poses a limitation for practical applications.

The stability of Pt–Au alloys was further systematically monitored during ADTs involving potentiodynamic cycling to different upper potentials: 1 V_{RHE}, 1.2 V_{RHE} and 1.5 V_{RHE}, simulating diverse fuel cell operating conditions. Overall, Pt–Au alloys exhibited better stability than monometallic Pt. However, it was found that surface composition changes occur on the surface of Pt–Au alloys after ADT. Depending on the upper potential, surface enrichment of either Au (1 V_{RHE} and 1.2 V_{RHE}) or Pt (1.5 V_{RHE}) occurred. This phenomenon was linked to the preferential dissolution of certain elements at certain cycling conditions or the surface segregation of these elements. However, due to the complex nature of the behavior, determining the specific mechanism remains challenging and requires additional comprehensive studies.

Lastly, the results obtained in a half-cell were compared with those from a single cell. The overall findings indicated slight variations in the single cell compared to the half-cell. Specifically, Pt90Au10 was found to be the optimal Pt–Au composition in terms of activity and stability. The discrepancies with half-cell experiments were attributed to the transition from an idealized liquid-based half-cell configuration to the more complex real single-cell setup, potentially influencing catalyst activity. Nonetheless, the positive impact of Au on Pt stabilization was consistently demonstrated even in a real PEMFC device.

3.2. Ternary PtNi–Au alloy catalysts.

3.2.1. Introduction

As described in the previous chapter, the controlled addition of small amounts of Au into a Pt catalyst can effectively enhance its stability without compromising its ORR activity. Nevertheless, in the case of Pt–Au alloys, there is no overall improvement in ORR activity, nor is there a reduction in catalyst cost. Therefore, alternative strategies must be explored to concurrently address both cost-efficiency and stability concerns. As mentioned in Chapter 1.3 one of the most effective strategies for increasing the cost-efficiency of ORR catalysts involves alloying platinum with relatively inexpensive and abundant 3d transition metals. Thus, in the search for an active and stable catalyst for PEMFCs, combining the above two approaches can be beneficial. The use of transition metal alloying reduces the catalyst costs and increases ORR activity while the addition of Au contributes to increased stability.

Indeed, ternary Pt–Au–M catalysts have been acknowledged as promising catalysts for the ORR, demonstrating increased activity and stability, along with reduced costs. For example, Gatalo et al. demonstrated that decorating Pt–Cu electrocatalyst with less than 1 % gold significantly increased its stability. Specifically, the gold-enriched surface of $Pt_{25-x}Au_xCu_{75}$ exhibited lower Pt dissolution and noticeably reduced Cu dissolution [119]. Kang et al. reported the optimal balance of activity and durability in Pt–Ni–Au multimetallic systems as a result of the synergy between the stabilizing effect of subsurface Au and the modified electronic structure of surface Pt atoms by their interaction with subsurface Ni atoms [120]. Using the similar Pt–Ni–Au system Liu et al. showed that it exhibited superior mass and specific activity compared to the commercial Pt/C and increased long-term stability during accelerated degradation tests in both half-cell and single-cell [73]. Enhanced activity and durability were further shown for Pt–Co–Au alloys [121, 122].

In this chapter, we present findings on ternary PtNi–Au alloys with various compositions prepared through a magnetron sputtering technique using three individual targets (for more details refer to the experimental chapter). The Pt to Ni atomic ratio was maintained constant at about 50:50 for all samples, while Au concentration was adjusted. The selection of Au amounts was based on experiments detailed in the previous chapter. In total, six samples were prepared, including PtNiAu3, PtNiAu7 and PtNiAu15 with 3, 7 and 15 at.% of gold, respectively, as well

as reference PtNi and monometallic Pt and Au to investigate the composition-activity-stability relationship.

3.2.2. Characterization of PtNi–Au alloy catalysts

The SEM images of the as-deposited layers are presented in Fig. 3.18. Similar to Pt–Au catalysts, PtNi–Au alloys with different compositions did not exhibit any significant morphological variations. Furthermore, their morphology appears comparable to that of the Pt–Au alloys, suggesting that morphology will not significantly impact further activity and stability measurements.

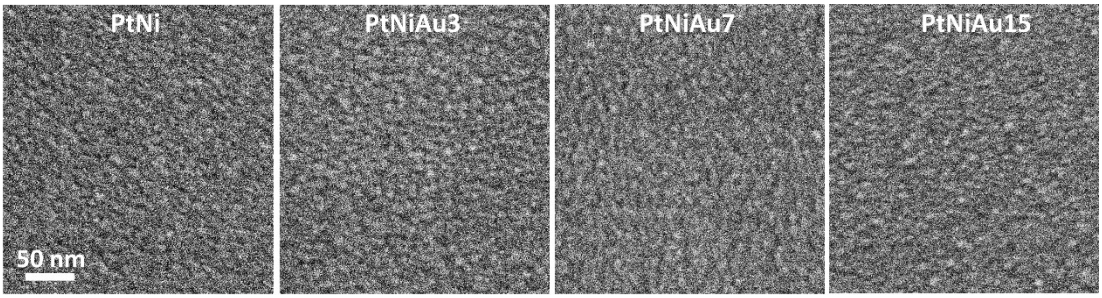

Fig. 3.18. *SEM images of the as-deposited PtNi and PtNi–Au alloy catalysts.*

The composition of the investigated PtNi–Au alloys was then verified using bulk-sensitive EDX and XPS techniques. The corresponding spectra are presented in Fig. 3.19. The EDX spectra in Fig. 3.19a were deconvoluted into three peaks at 7.48 keV, 9.44 keV and 9.71 keV, corresponding to Ni Kα, Pt Lα and Au Lα, respectively. The relative atomic composition of all investigated samples, quantified from their corresponding EDX spectra, is summarised in Table 3.4. It is evident that the measured compositions closely match the intended ones with only slight deviations.

The XPS spectra of PtNi–Au alloys, shown in Fig. 3.19b, are composed of three doublets at approximately 84 eV, 71 eV and 65 eV, corresponding to Au 4f, Pt 4f and Ni 3p, respectively [123, 124]. The Ni 3p core level was chosen for XPS spectra analysis because it emerges at a similar binding energy as Pt 4f and Au 4f, ensuring comparable kinetic energies of photoelectrons (probing depth) for all three elements. Table 3.4 provides the relative elemental compositions of PtNi–Au alloys quantified from the corresponding XPS spectra taking into account sensitivity factors, showing

only slight deviations from those obtained by EDX and demonstrating good agreement with the intended compositions.

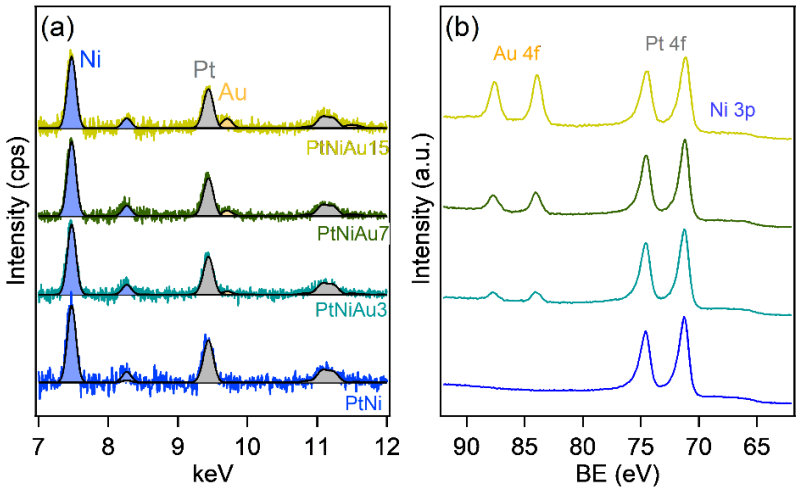

Fig. 3.19. *(a) EDX and (b) XPS spectra acquired for as-deposited PtNi–Au alloy catalysts.*

The surface-sensitive SRPES was further used to analyze the as-deposited PtNi–Au alloys. The Au 4f and Pt 4f together with Ni 3p SRPES spectra recorded over all investigated samples are depicted in Figs. 3.20a and b, respectively. The relative atomic compositions of the PtNi–Au alloys quantified from corresponding spectra taking into account sensitivity factors are $Pt_{48}Ni_{48}Au_4$, $Pt_{49}Ni_{44}Au_7$, $Pt_{47}Ni_{41}Au_{12}$ and $Pt_{55}Ni_{45}$ for the reference layer (see Table 3.4), which well correlate with the composition obtained by using bulk-sensitive EDX and XPS techniques highlighting homogeneous compositional profile in the PtNi–Au catalyst layers prepared by magnetron co-sputtering.

Same as for the Pt–Au bimetallic alloy we further took a closer look at the electronic structure of the ternary alloy. For better comparison, Fig. 3.20c summarises the position of Au $4f_{7/2}$, Pt $4f_{7/2}$ and Ni 3p peaks for all investigated samples. First, we analyzed the reference PtNi alloy catalyst. Compared with their monometallic spectra, the Pt 4f and Ni 3p spectra of the reference PtNi catalytic layer are significantly shifted. The Pt 4f upshifts from 70.95/74.25 eV for monometallic Pt to 71.1/74.4 eV for PtNi [124]. In turn, Ni 3p downshifts from 66 eV for monometallic Ni [125] to 65.7 eV for the PtNi alloy indicating strong modification of Pt and Ni electronic structures due to their alloying.

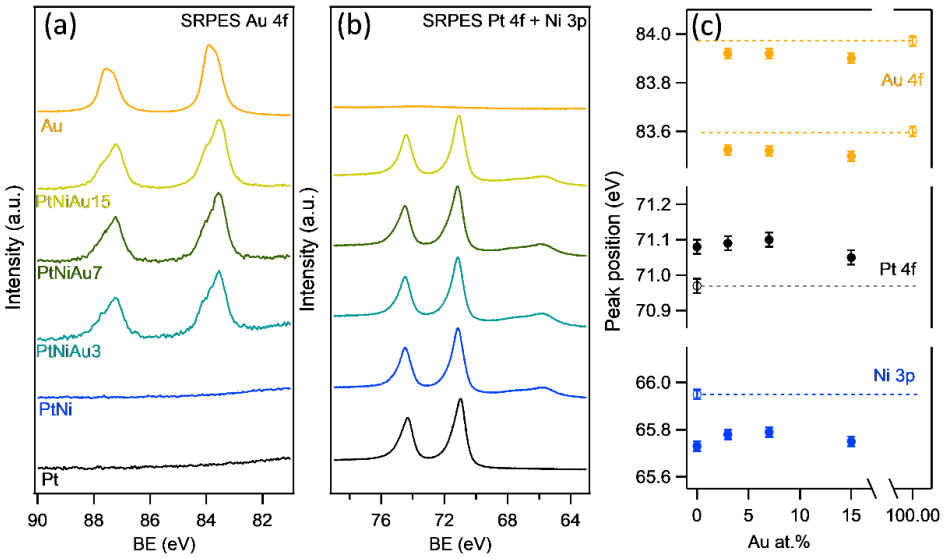

Fig. 3.20. *(a) SRPES Au 4f and (b) SRPES Pt 4f + Ni 3p spectra acquired for as-deposited PtNi–Au, PtNi and monometallic Pt catalysts at 180 eV excitation energy. (c) Evolution of Au $4f_{7/2}$, Pt $4f_{7/2}$ and Ni 3p peak positions with increasing Au content extracted from the spectra shown in (a) and (b).*

Table. 3.4. *Relative composition of as-deposited PtNi–Au alloys calculated using EDX, XPS and SRPES techniques.*

	SRPES	XPS	EDX
PtNi	$Pt_{55}Ni_{45}$	$Pt_{46}Ni_{54}$	$Pt_{55}Ni_{45}$
PtNiAu3	$Pt_{48}Ni_{48}Au_4$	$Pt_{44}Ni_{53}Au_3$	$Pt_{47}Ni_{50}Au_3$
PtNiAu7	$Pt_{49}Ni_{44}Au_7$	$Pt_{42}Ni_{50}Au_8$	$Pt_{45}Ni_{48}Au_7$
PtNiAu15	$Pt_{47}Ni_{41}Au_{12}$	$Pt_{39}Ni_{44}Au_{17}$	$Pt_{42}Ni_{43}Au_{15}$

In contrast to the Pt–Au bimetallic systems, the addition of Au to PtNi does not reveal a clear trend in the SRPES spectra as can be observed in Fig. 3.20c. This can be attributed to the fact that interpreting the photoelectron spectra of the ternary alloy presents a more complex scenario than that for a bimetallic alloy. The challenge arises from the overlapping effects of Pt–Au, Pt–Ni, and Au–Ni interactions within the ternary alloy. The intricate nature of these intermetallic interactions and their influence on binding energies thus creates a complex spectrum that does not distinctly reflect significant changes with increasing Au content. Consequently, drawing solid conclusions from the SRPES spectra of the PtNi–Au alloy becomes a challenging task. Nevertheless, it is important to mention that for all PtNi–Au alloys, the positions of Pt 4f, Au 4f, and Ni 3p remain distinct from those of the monometallic counterparts. Regarding the Pt 4f core level, its position consistently exhibits a higher binding energy

than that of monometallic Pt. This upshift generally leads to a downward shift of the Pt d-band center, consequently reducing the binding affinity between Pt and oxygen intermediates which is beneficial for the ORR [126-128].

3.2.3. Activity of ternary PtNi–Au alloy catalysts.

The electrochemical properties of the ternary PtNi–Au alloys were then analyzed in a half-cell system. The CVs of the as-deposited PtNi–Au catalysts, along with those for the PtNi alloy and monometallic Pt for ease of comparison, were captured in N_2-saturated 0.1 M $HClO_4$ solution. The results are presented in Fig. 3.21a.

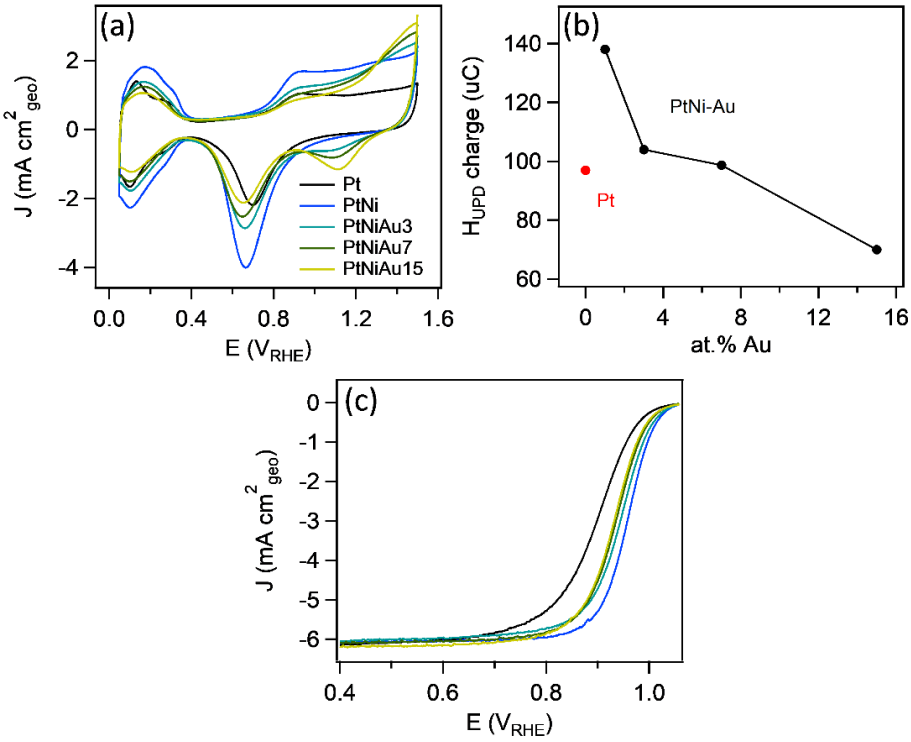

Fig. 3.21. *(a) Cyclic voltammograms of the as-deposited monometallic Pt and PtNi, as well as the PtNi–Au alloy catalysts recorded in N_2-saturated 0.1 M $HClO_4$ solution; (b) Evolution of H_{UPD} charge calculated from the voltammograms shown in (a); (c) ORR polarization curves of the as-deposited monometallic Pt and PtNi, as well as the PtNi–Au alloy catalysts recorded in O_2-saturated 0.1 M $HClO_4$ solution at 1600 rpm rotating speed and 20 mV s^{-1} scan rate.*

It can be observed that the voltammogram of the PtNi alloy (blue curve) closely resembles that of monometallic Pt (black curve) but overall exhibits much larger currents across the entire potential window. This behavior is attributed to the initial

leaching of Ni from the PtNi surface already upon contact with the electrolyte solution, resulting in the formation of a so-called Pt skeleton structure with an increased active area. This is evidenced by the increased H_{UPD} charge, as shown in Fig. 3.21b [129]. It is also important to note that Ni does not exhibit any oxidation/reduction peaks, as the standard reduction potential of Ni is –0.25 V_{RHE} [130], which is outside of this potential window. As Au was progressively added and its concentration increased in the PtNi alloy, a similar tendency was observed as described in the previous chapter for the Pt–Au bimetallic alloys. Specifically, all peaks associated with Pt started to decrease while shifting to the lower potentials, and all peaks associated with Au increased while shifting in the opposite direction which was attributed to the alloy formation. As the Pt peak decreases, there is a corresponding decrease in H_{UPD} charge (see Fig. 3.21b). Nevertheless, the samples containing 3 and 7 at.% of gold still exhibit a higher active area than monometallic Pt. Only the PtNiAu15 catalyst showed a lower H_{UPD} charge, indicating a lower active area. In contrast to the Pt–Au alloys, the leaching of Ni from the PtNi–Au surface eliminates the need to calculate the alloy composition on the surface based on cyclic voltammograms (CVs) in Fig 3.21a or CO-stripping experiments and compare it with that obtained by surface characterization techniques.

Table. 3.5. *Kinetic parameters obtained from the ORR polarization curves.*

Samples	$E_{1/2}$ (V_{RHE})	J_k at 0.9 V_{RHE} ($mA \cdot cm^{-2}_{geo}$)
Pt	0.90	5.6
PtNi	0.956	41.5
PtNiAu3	0.944	22.7
PtNiAu7	0.935	18.1
PtNiAu15	0.93	15.4

The ORR polarization curves of the ternary PtNi–Au catalysts, as well as the PtNi and monometallic layers, obtained in O_2-saturated 0.1M $HClO_4$ electrolyte, are presented in Fig. 3.21c. In turn, the half-wave potential and kinetic current values extracted from the corresponding polarization curves are summarized in Table 3.5. It is noteworthy that the PtNi catalyst exhibited significantly superior ORR activity compared to monometallic Pt which is in line with previous reports [131-133]. The stepwise introduction of Au to the PtNi alloy led to a gradual decrease in ORR activity.

However, the activity remained slightly better even for the sample containing the highest amount of Au, i.e., PtNiAu15, than that of monometallic Pt.

3.2.4. Stability of ternary PtNi–Au alloy catalysts.

After carefully analyzing the ORR activity of the PtNi–Au alloys, their stability was tested using an *in situ* SFC-ICP-MS device. Due to significant Ni dissolution even after contact with the solution given by its thermodynamic stability at these conditions [49, 134], a slightly different measuring protocol was applied than the one for the Pt–Au alloys. Specifically, it involved a so-called contact dissolution lasting 5 minutes prior to potential cycling. Subsequently, dissolution was measured during two identical cycles from 0.05 to 1.2 V_{RHE}. The same procedure was repeated for the other potential limit (1.5 V_{RHE}) on a fresh spot on the same sample.

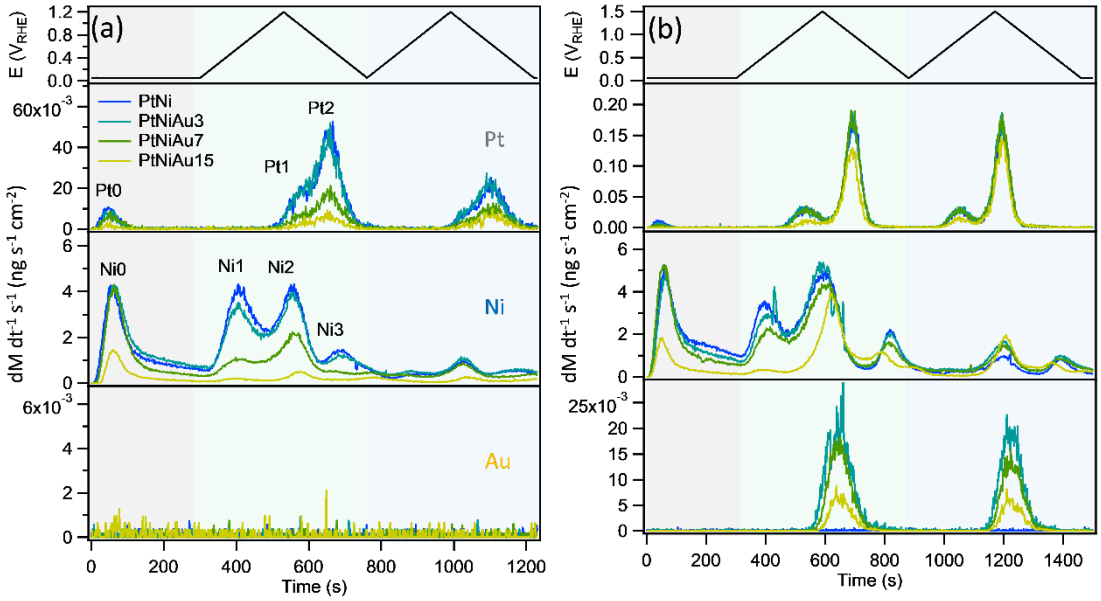

Fig. 3.22. *The applied potential protocol along with representative Pt, Ni, and Au dissolution mass-spectrograms taken from the PtNi–Au alloy catalysts, as well as the PtNi electrode, for (a) 1.2 V_{RHE} UPL and (b) 1.5 V_{RHE} UPL.*

Fig. 3.22 illustrates the mass spectrograms as a function of time for the analyzed elements for all investigated PtNi–Au compositions, as well as the reference PtNi alloy alongside the applied potential electrochemical protocol. The mass spectra were normalized by the amount of the respective element on the surface of the alloy, as determined through previous characterizations. For clarity, the contact dissolution

region is highlighted with a grey background, while the first and second cycles are highlighted with green and blue backgrounds, respectively.

When the UPL was set to 1.2 V_{RHE} (Fig. 3.22a), the Pt dissolution profile consisted of a contact dissolution peak (Pt0) followed by a dissolution peak in each cycle, encompassing both anodic (Pt1) and cathodic (Pt2) peaks. The appearance of a contact dissolution peak is usually attributed to platinum surface oxidation due to the sample exposure to air [101, 135]. The intensity of the dissolution peaks decreases as the Au concentration increases, suggesting that the addition of Au suppresses Pt dissolution. The quantified total dissolution of Pt obtained by integrating corresponding dissolution profiles for all investigated samples is summarised in Fig. 3.23a (green line). It can be observed that the overall Pt dissolution is suppressed by 13, 61 and 85 % for the PtNiAu3, PtNiAu7, and PtNiAu15 samples, respectively, with respect to the PtNi alloy.

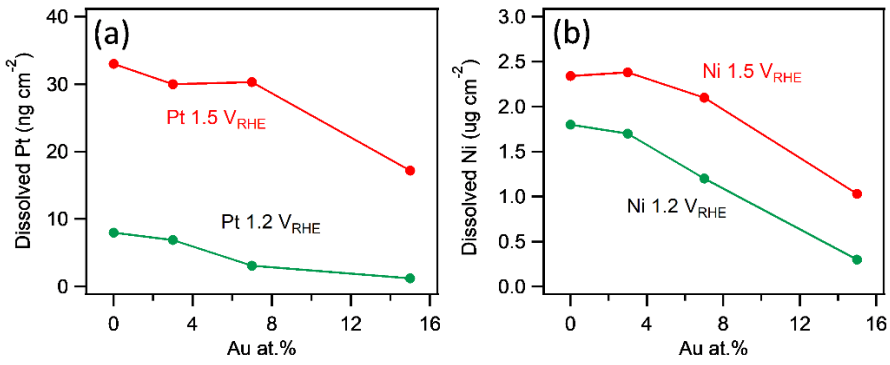

***Fig. 3.23**. Normalized total dissolution of (a) Pt and (b) Ni from the PtNi–Au alloys and PtNi reference sample obtained by integrating the corresponding mass-spectrograms shown in Fig. 3.22.*

The Ni dissolution spectrogram is more complex than that of Pt. It consists of multiple peaks, including a contact dissolution peak (Ni0), the anodic Ni dissolution (Ni1), and two additional peaks Ni2 and Ni3 that could be assigned to Ni dissolution stimulated by both anodic and cathodic dissolution of Pt, respectively. Interestingly, Ni dissolution is also slowed down as a function of Au concentration. The quantified total dissolution of Ni obtained by integrating corresponding dissolution profiles for all investigated samples is summarised in Fig. 3.23b (green line). Overall, Ni dissolution is suppressed by 5, 37 and 83 % for the PtNiAu3, PtNiAu7 and PtNiAu15 samples, respectively, with respect to the PtNi alloy. A similar effect was previously

observed for copper dissolution in the case of $Pt_{25-x}Au_xCu_{75}$ alloys and attributed to the faster surface diffusion of Au atoms that can better prevent the process of copper dealloying and pore formation than a pure Pt surface [119]. Regarding Au dissolution, it was not observed because, as mentioned in the previous chapter, the potential of 1.2 V_{RHE} is not sufficient to oxidize Au and initiate its dissolution.

When the UPL is set to 1.5 V_{RHE}, (see Fig. 3.22b) the Au stabilization effect was not as pronounced as for the 1.2 V_{RHE} UPL. Specifically, Pt dissolution with respect to the PtNi alloy was suppressed by only 9 % and 8 % for the PtNiAu3 and PtNiAu7 samples, respectively (see Fig 3.23a, red curve). A more significant decrease in Pt dissolution (48 %) was observed only for the PtNiAu15 sample. Regarding Ni dissolution, it was not suppressed at all for the PtNiAu3 sample as can be observed in Fig 3.23b (red curve). Nevertheless, for PtNiAu7, and PtNiAu15 samples Ni dissolution was suppressed by 10 and 53 %, respectively. Regarding Au dissolution, similar to the case of Pt–Au alloys, it consists of one dissolution peak that should include both anodic and cathodic peaks, and it increases with a decrease in the amount of Au.

The experimental results above highlight a parallel with the Pt–Au alloys described in the previous chapter, indicating, on the one hand, a detrimental impact of Au on PtNi–Au activity, and on the other hand, a positive effect on its stability. Extrapolating insights from the preceding chapter, these observations can be associated with the structure of the PtNi–Au alloys. Upon immersion in the electrolyte, Ni dissolves, as confirmed by ICP-MS analysis, generating numerous defects in the Pt surface structure. It can be anticipated that these defects are predominantly filled with Au, as indicated by a theoretical study in the previous chapter (unfortunately, theoretical studies on the PtNi–Au alloys were not conducted). However, not all defects can be filled with the amount of Au under study, leaving a relatively large amount of lower-coordinated Pt, particularly in the case of PtNiAu3 and PtNiAu7 samples. This accounts for the absence of a significant stabilization effect unless Au concentration in the PtNi–Au alloy reaches 15 at.% which corresponds to approximately 35 at.% of Au relative to Pt, considering the absence of Ni from the few outermost surface layers. For this catalitic layer stability has increased by almost 80 % at 1.2 V_{RHE} UPL and by nearly 50 % at 1.5 V_{RHE} UPL in terms of Pt dissolution. On the other hand, such a large amount of Au had a detrimental effect on the activity, as evidenced by a nearly 60 % decrease in kinetic current for PtNiAu15 compared to the

PtNi alloy. However, despite this decrease, the kinetic current still remained approximately 2.5 times higher for PtNiAu15 than for monometallic Pt, which can be attributed to the presence of Ni in the subsurface regions of the alloy.

3.2.5. Conclusions

In this chapter, a ternary PtNi–Au alloy catalyst with various compositions (3, 7, 15 at.% of Au, Pt:Ni = 50:50) prepared by magnetron co-sputtering was investigated, aiming to further enhance both the activity and stability of the ORR catalyst. Building upon the findings from the previous chapter, the composition-activity-stability relationship was thoroughly analyzed using complementary characterization techniques and electrochemistry.

It was observed that similar to Pt–Au catalysts the activity of PtNi–Au exhibited a decreasing trend as the Au concentration increased. However, despite the lower activity of PtNiAu15 alloy compared to PtNi alloy, it was still approximately three times higher than that of monometallic Pt. Regarding stability, the addition of Au into PtNi alloy showed a positive effect on the stabilization of both Pt and Ni, inhibiting significantly their dissolution over an extended potential range up to 1.5 V_{RHE}. Compared to PtNi alloy, the Pt and Ni dissolution from PtNiAu15 alloy were suppressed by 85 % and 83 %, respectively, during potential cycling to 1.2 V_{RHE}, and by 48 % and 53 % during potential cycling to 1.5 V_{RHE}.

3.3. Nanoporous Pt–C catalyst

3.3.1. Introduction

Another approach to significantly enhance the cost-efficiency of an ORR catalyst is to minimize its surface-to-bulk ratio. One of the possibilities to achieve this is to prepare a nanoporous catalyst that maximizes the active surface area of platinum, thereby enhancing its utilization and thus reducing the price of cathode catalyst [136]. Various methods can be employed to obtain nanoporous structures, including template-based techniques [137], hydrothermal growth [138], dealloying of multicomponent catalysts [139], etc. Dealloying, in particular, is the most straightforward approach and has been extensively studied for producing nanoporous materials for energy storage, sensing and catalytic applications [140].

Dealloying involves the selective chemical or electrochemical dissolution of the less noble metal from a bimetallic alloy, resulting in the formation of spongy catalyst, enriched or primarily composed of the more noble element, characterized by highly irregular pores, pits and voids in their interior [141, 142]. The structure of the resulting catalyst can be tuned by adjusting various preparation parameters, such as alloy composition, dealloying time, temperature, and electrochemical conditions. In terms of composition, the dealloying process is predominantly favorable if the concentration of the less noble metal exceeds a critical value, which is typically more than 50-60 at.%. For instance, Strasser et al. employed copper-rich $PtCu_3$ alloy catalysts to deliberately undergo selective electrochemical dealloying, creating a Pt-enriched particle architecture that showed an increase in mass activity [143]. Numerous other non-noble metal-rich bimetallic alloys, including Pt–Ni [132, 144] and Pt–Co [145] have been subjected to electrochemical dealloying, resulting in the formation of the nanoporous platinum catalyst with enhanced catalytic activity due to an increased active surface area [131, 143].

Building upon the aforementioned principles, in this chapter, we demonstrate the concept of electrochemical dealloying on ternary Pt–C–CeO_x compound, prepared by magnetron sputtering, with the aim of creating a highly porous Pt–C ORR catalyst. Here, carbon was added to stabilize platinum during a severe CeO_2 leaching process during the electrochemical activation procedure. Moreover, previous studies have indicated that Pt–C catalysts improve the performance and durability of methanol and hydrogen-fueled fuel cells [110, 146, 147]. The advantage of using CeO_2 lies in its

facile and selective dissolution in an electrochemical environment. Furthermore, if some residual ceria remains in the catalyst after the dealloying process, its negligible further dissolution during PEMFC operation poses no harm to the Nafion membrane. Indeed, ceria has demonstrated radical scavenging behavior within the membrane, contributing to its prolonged lifetime [148, 149].

3.3.2. Characterization of the as-deposited Pt–C–CeO_x layer

The samples were deposited on a Si (111) wafer precovered with a 10 nm carbon interlayer to mimic the carbon support utilized in the benchmarked Pt/C catalysts. The deposition was achieved through simultaneous co-sputtering of Pt, C, and CeO_2, as schematically illustrated in Fig. 3.24a. The total thickness of the deposited layer was measured to be approximately 70 nm. Fig. 3.24b and c present SEM and AFM images of the as-deposited Pt–C–CeO_x layer, respectively. The images reveal that the deposited layer consists of uniformly distributed grains with an average size of approximately 5–10 nm.

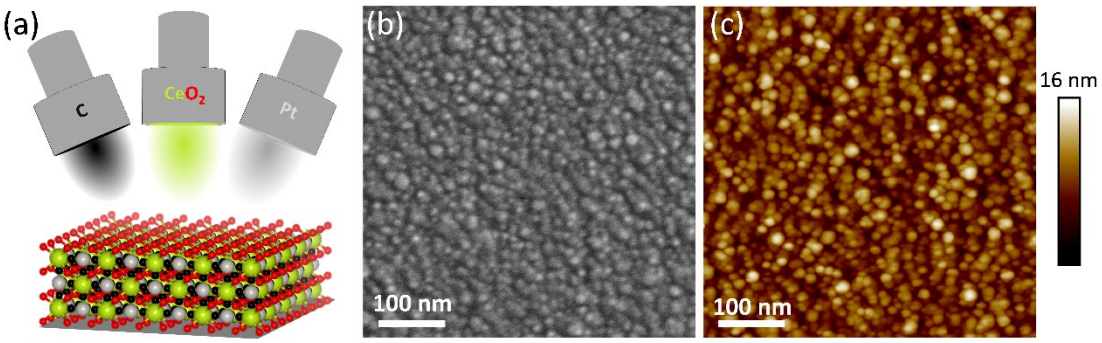

Fig. 3.24. *(a) Schematic illustration of Pt–C–CeO_x deposition process from three individual targets; (b) SEM and (c) AFM images of the as-deposited Pt–C–CeO_x layer.*

The structure of the Pt–C–CeO_x layer was further investigated using high-resolution transmission electron microscopy (HRTEM) and XRD. Fig. 3.25 presents the HRTEM cross-section image of the catalyst layer along with the corresponding fast Fourier transform (FFT) pattern (Fig 3.25a inset). Overall, the structure exhibits a slightly tilted columnar shape which is given by placing the Pt target at a 45° angle in relation to the substrate. A closer examination of the corresponding image reveals that the catalyst comprises randomly oriented crystallites, characteristic of a polycrystalline structure. This is supported by the FFT pattern, revealing a characteristic ring pattern.

The ring radii (interplanar spacing) extracted from the corresponding FFT pattern are 3.2, 2.75, 2.3, and 2.0 Å assigned to the interplanar spacing of CeO_2(111), CeO_2(200), Pt(111), and Pt(200), respectively [150, 151]. This suggests the coexistence of both Pt and CeO_2 crystalline phases.

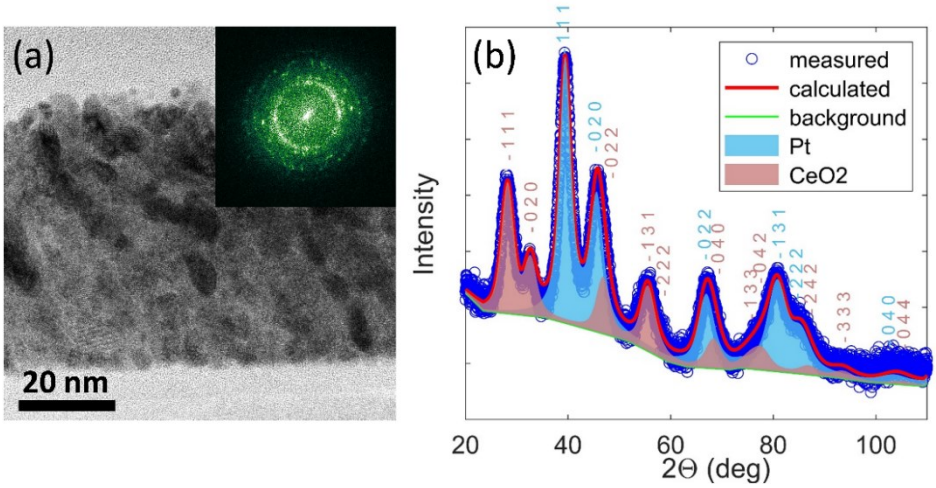

Fig. 3.25. *(a) cross-section HRTEM image (inset: a fast Fourier transformation (FFT) of the image in (a)) of the as-deposited Pt–C–CeO_x film; (b) Measured (blue circles) and fitted (red line) XRD diffractogram of the as-deposited Pt–C–CeO_x layer.*

The above results were further corroborated by XRD. Fig. 3.25b presents the measured Pt–C–CeO_x diffractogram. The face-centered cubic (fcc) Pt structure (space group Fm−3m), highlighted in blue, and the cubic fluorite CeO_2 structure (space group Fm−3m) highlighted in red, are clearly visible, which is in line with the results of FFT in Fig. 3.22a [152, 153]. Particularly, the most intense diffraction peaks observed at $2\theta = 28.6$, 33.1, 40.1, and 46.1 correspond to the (111) and (200) lattice planes of CeO_2 and Pt, respectively [154]. The crystallite size and lattice constant were further calculated from the corresponding diffractogram. The average crystallite size of Pt and CeO_2 was measured to be 4.78 ± 0.16 nm and 2.71 ± 0.1 nm, respectively. In turn, the lattice parameter for Pt and CeO_x were measured as 0.39402 ± 0.00018 nm and 0.54974 ± 0.00014 nm, respectively, which is slightly deviating from tabulated values (0.398 nm for Pt, 0.547 nm for CeO_2). This can be attributed to the significant fraction of crystal lattice defects present in the deposited layer.

EDX and XPS techniques were then employed to determine the chemical composition of the deposited Pt–C–CeO_x catalyst. Fig. 3.26a shows a background-free EDX spectrum of Pt–C–CeO_x. It can be straightforwardly concluded that the deposited

catalyst contains solely Pt Ce, C, and O elements. The relative Pt/Ce ratio calculated from the corresponding EDX spectrum is 1.4. It is noteworthy that due to the presence of a carbon interlayer and a native oxide layer on the Si(111) substrate, obtaining the precise chemical composition of the catalyst from the EDX spectrum is impossible due to the relatively high mean free path of characteristic X-rays.

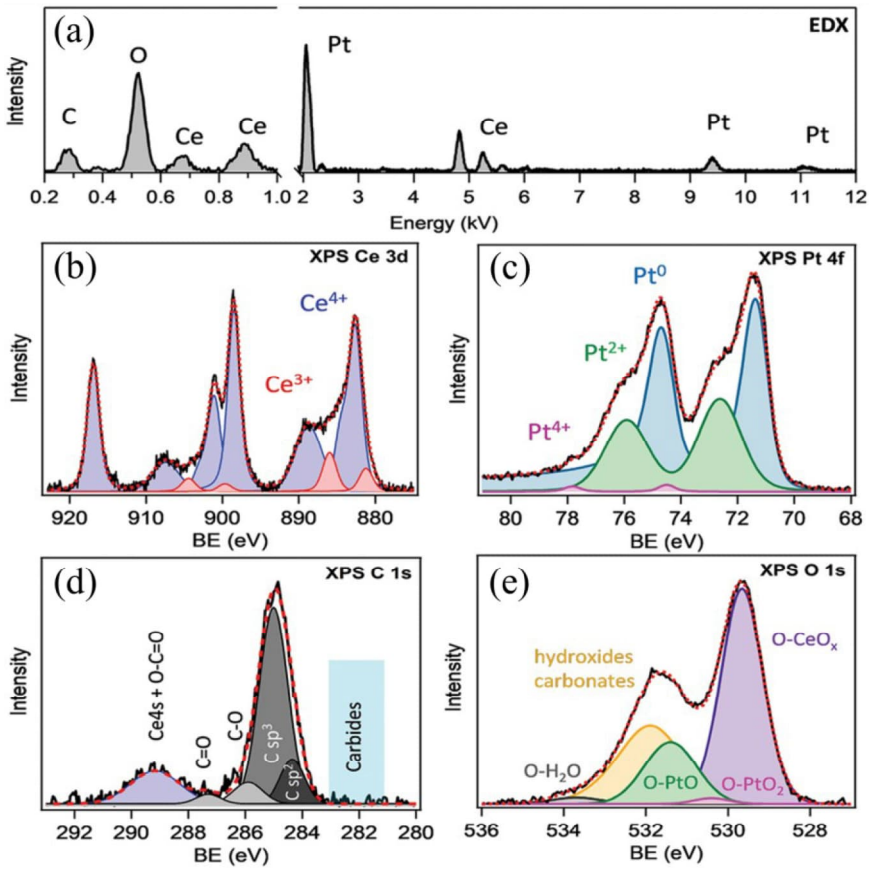

Fig. 3.26. *(a) Background-free EDX spectrum; (b) XPS Ce 3d spectrum; (c) XPS Pt 4f spectrum; (d) XPS C 1s spectrum and (e) XPS O 1s spectrum of the as-deposited Pt–C–CeO_x layer.*

Table. 3.6. *The relative atomic composition of the as-deposited Pt–C–CeO_x catalyst layer calculated from XPS spectra.*

Element	at.%
Pt	14
Ce	11
C	32
O	43

Therefore, the more surface-sensitive XPS technique was employed to determine both the chemical composition of the catalyst layer and the chemical state of its constituent elements. Fig. 3.26(b) – (e) presents the high-resolution XPS spectra of Ce 3d, Pt 4f, C 1s and O 1s core levels. The Ce 3d spectrum was deconvoluted into three spin-orbit-split doublets characteristic of the Ce^{4+} states and two spin-orbit-split doublets characteristics of the Ce^{3+} states, evidencing partial reduction of cerium oxide [155].

The Pt 4f XPS spectra were fitted using three doublets as shown in Fig. 3.26c. The predominant doublet, with 57 % contribution at a binding energy of 71.3/74.6 eV, corresponds to metallic platinum (Pt^0) [156]. The doublet at 72.5/75.8 eV, with a 41 % contribution, can be attributed to Pt^{2+} oxidation states [157], while the less intense doublet, accounting for only 2 % at 74.5/77.8 eV, could be assigned to Pt^{4+} oxidation states. The partial formation of Pt^{2+} and Pt^{4+} oxidation states is consistent with previous studies on magnetron-sputtered Pt–CeO_x systems containing very low Pt amounts. In those studies, Pt^{2+} contribution was attributed to single Pt atoms which are stabilized inside square oxygen pocket sites at the surface of CeO_x, while Pt^{4+} states were related to Pt atoms that substitute Ce atoms in the bulk [61, 157, 158].

The corresponding C1s spectrum is shown in Fig. 3.26d. It contains a dominant peak at about 285 eV, which can be deconvoluted into two contributions. The first at 284.8 eV could be attributed to sp^3-bonded carbon, and the second at 284.3 eV could be assigned to sp^2-bonded carbon [159]. The small peaks at 285.9 and 287.3 eV correspond to C–O and C=O groups, respectively [160], while the peak at 289 eV originates from the overlapped contribution of Ce 4s core levels from cerium oxide [156] and the O–C=O surface group [161].

The O1s spectrum (Fig. 3.26e) consists of multiple contributions. The peak at 529.6 eV is associated with lattice oxygen in CeO_x [162], while peaks at 530.3 and 531.4 eV correspond to oxygen from PtO_2 and PtO, respectively [163]. In turn, the peak at 532 eV indicates the presence of hydroxyl groups and carbonates [164], and the last peak at 533.7 eV is associated with water molecules adsorbed on the surface of the catalyst layer [165].

The relative atomic composition of the Pt–C–CeO_x catalyst, determined using the corresponding XPS spectra and taking into account the sensitivity factors, can be found in Table 3.6. Specifically, the analysis reveals that the catalyst layer contains 14 at.% of Pt, corresponding to an approximate Pt loading of 20 μg cm^{-2} when

accounting for the 70 nm thickness of the layer. The relative Pt to Ce ratio calculated from XPS results is approximately 1.3, closely matching that obtained with EDX analysis (1.4) and indicating a homogeneous composition profile in the magnetron-sputtered Pt–C–CeO_x layer.

3.3.3. Characterization of Pt–C–CeO_x layer during electrochemical activation procedure

The Pt–C–CeO_x catalyst was then deposited onto a glassy carbon electrode to undergo the electrochemical activation procedure in a half-cell configuration. This procedure involved 30 potentiodynamic cycles from 0.05 to 1.2 V_{RHE} in an N_2-saturated 0.5 M H_2SO_4 solution. The captured cyclic voltammograms during the activation procedure are presented in Fig. 3.27a. It is noticeable that, with an increasing cycle number, the detected currents rose across the entire potential window, indicating an increase in ECSA. Moreover, within the H_{UPD} region, two sharp peaks emerged during cycling, which is a fingerprint of polycrystalline platinum surfaces. The above observations suggest the continuous leaching of cerium oxide from the Pt–C–CeO_x thin film at the early stages of cycling. At later stages, the CV stabilized, which could be associated with complete leaching of cerium oxide.

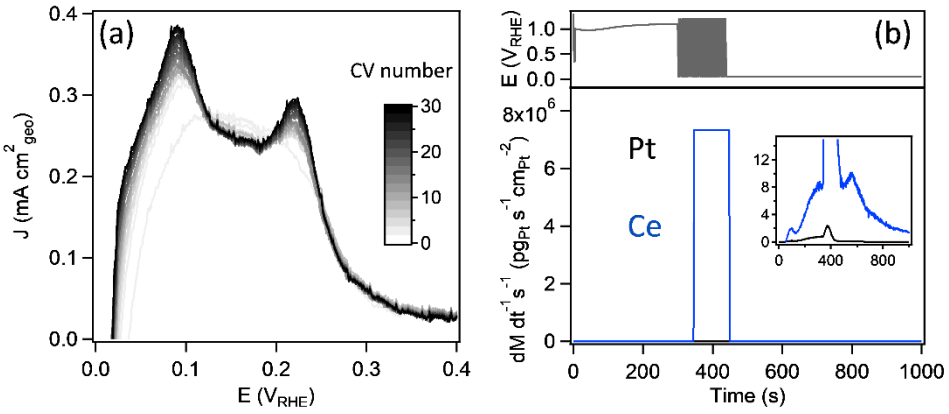

Fig. 3.27. *(a) Highlighted H_{UPD} region from 30 CV curves recorded in N_2 statured 0.5 M H_2SO_4 electrolyte during electrochemical activation of the as-deposited Pt–C–CeO_x layer; (b) Pt (black curve) and Ce (blue curve) dissolution mass spectrograms recorded during electrochemical activation of the as-deposited Pt–C–CeO_x layer (Inset: zoomed Pt and Ce dissolution mass spectrograms).*

Indeed, cerium oxide leaching is anticipated at the above conditions according to the Pourbaix diagram [49]. This was further substantiated by *in situ* SFC-ICP-MS. Fig. 3.27b presents the mass spectrogram recorded during potentiodynamic cycling and illustrates the dissolution rate of both Pt (black curve) and Ce (blue curve), along with the applied potential protocol (grey curve). It is evident that Ce dissolution significantly increases after starting the cycling process, even surpassing the detection limit of the ICP-MS device, and it stays at this level up until the end of cycling. In parallel a small amount of Pt dissolution was observed, which is most likely attributed to substantial CeO_x leaching. From the zoomed Pt and Ce dissolution profiles in the inset of Fig 3.27b, it can be observed that Ce starts dissolving even prior to initiating the cycling procedure, and continues shortly thereafter until it drops almost to zero. These results align well with the CV results above and provide clear evidence that a significant amount, if not all of CeO_x, is leached during the electrochemical activation procedure, which should lead to the formation of a high surface area Pt–C catalyst.

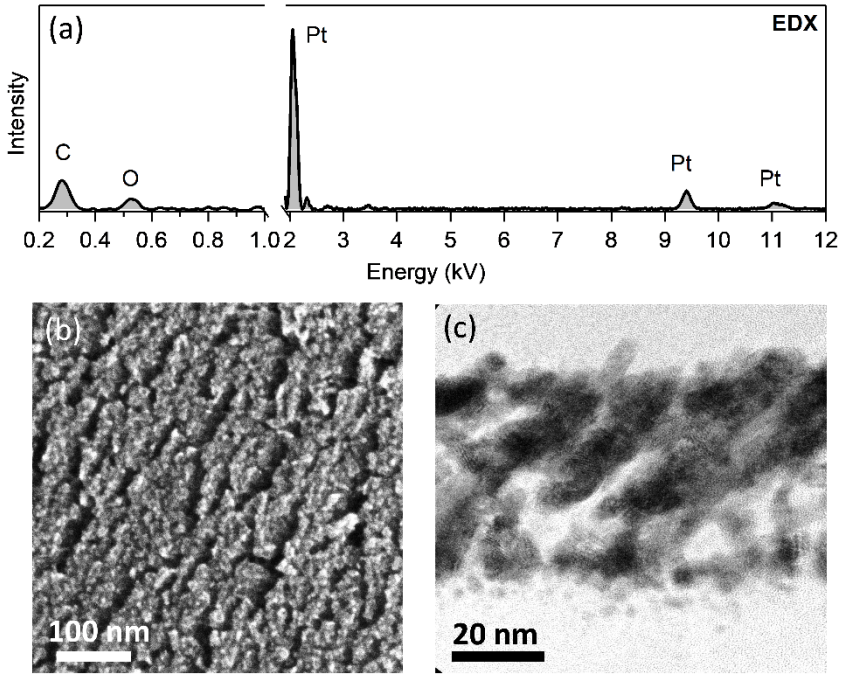

Fig. 3.28. *(a) Background-free EDX spectrum; (b) SEM image and (c) HRTEM cross-section image of the Pt–C–CeO_x layer after electrochemical activation procedure.*

The EDX, SEM, and TEM techniques were then employed to investigate the composition and morphology of the catalyst layer after the electrochemical activation procedure. The background-free EDX spectrum in Fig. 3.28a confirms the above

results, showing that Ce has completely vanished from the catalyst layer. The SEM image in Fig. 3.28b further confirms the formation of narrow and slit pores on the surface as a result of CeO_x leaching. In turn, the cross-section HRTEM image in Fig. 3.28c reveals the presence of highly irregular pores, pits, and voids in the layer interior. Overall, we can conclude that electrochemical pretreatment of the Pt–C–CeO_x layer leads to the formation of a high surface area Pt–C catalyst as a result of cerium oxide leaching.

3.3.4. Activity and stability of Pt–C catalyst during potentiodynamic cycling in a half-cell

The electrochemical properties of the Pt–C–CeO_x catalyst (hereafter denoted as Pt–C) were further analyzed in the half-cell system and compared with a reference monometallic Pt layer with an identical loading of platinum (20 $\mu g \cdot cm^{-2}$). The reference sample was prepared by depositing a Pt layer with a thickness of 10 nm using the magnetron sputtering technique. Fig 3.29a compares the CVs of the Pt–C and Pt catalysts captured in an N_2-saturated 0.5 M H_2SO_4 solution.

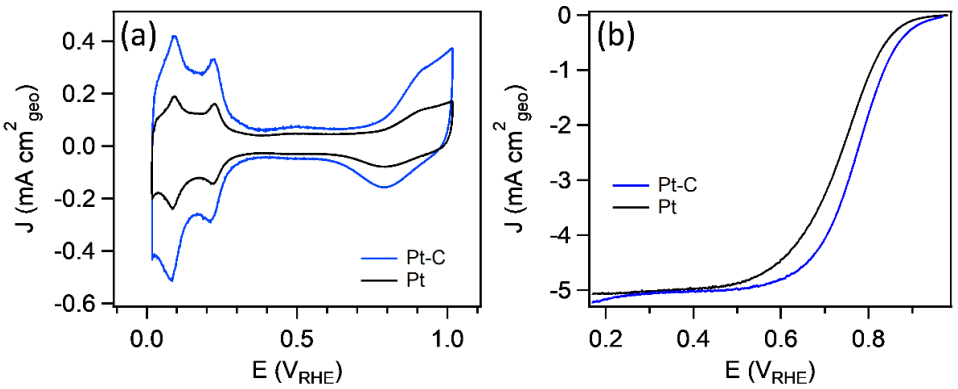

Fig. 3.29. *(a) CVs of the Pt–C and monometallic Pt catalysts recorded in N_2-saturated 0.5 M H_2SO_4 solution; (b) ORR polarization curves of the Pt–C and Pt catalysts recorded in O_2-saturated 0.5 M H_2SO_4 solution at 1600 rpm rotation speed and 20 mV s^{-1} scan rate.*

It can be observed that the CV of the Pt–C catalyst shows significantly larger currents across the entire potential window than that for the monometallic Pt, indicating a higher surface area of the Pt–C catalyst. This observation corresponds well to the findings discussed in the previous chapter. The ECSA values calculated from

the corresponding voltammograms can be found in Table 3.7 and indicate a 2.5-fold increase in ECSA for Pt–C compared to the monometallic Pt catalyst.

The ORR polarization curves of the Pt–C and Pt catalysts obtained in O_2-saturated 0.5 M H_2SO_4 solution are presented in Fig 3.29b. In turn, the $E_{1/2}$ values extracted from the corresponding polarization curves are summarized in Table 3.7. Notably, the $E_{1/2}$ for Pt–C is shifted by nearly 30 mV towards higher potentials compared to that of monometallic Pt, indicating a significant increase in ORR activity. Note that a direct comparison of the ORR activity measured in this chapter with that in the previous chapters of the present thesis is not feasible due to the in general significantly lower electrocatalytic activity in sulfuric acid-based electrolytes compared to perchloric acid-based one. Nevertheless, by comparing the activity of Pt–C and monometallic Pt under identical conditions, we were able to clearly observe the significantly higher activity of the porous Pt–C catalyst.

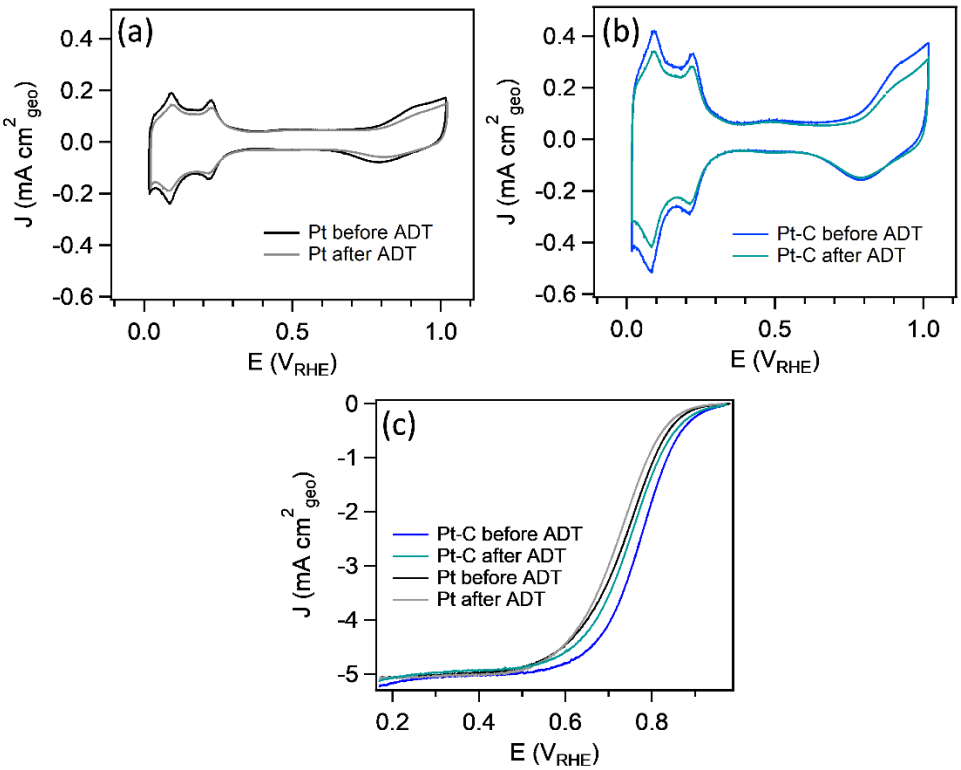

Fig. 3.30. *CVs of (a) monometallic Pt and (b) Pt–C catalyst recorded in N_2-saturated 0.5 M H_2SO_4 solution before and after ADT; (c) ORR polarization curves of monometallic Pt and Pt–C catalyst recorded in O_2-saturated 0.5 M H_2SO_4 solution at 1600 rpm rotating speed and 20 mV s^{-1} scan rate before and after ADT.*

Table. 3.7. *The electrochemical performance of the catalyst layer in a half-cell.*

Sample	Pt loading (μg cm^{-2})	ECSA (m^2 g^{-1})	$E_{1/2}$ (V_{RHE})
Pt before ADT	20	10.5	0.75
Pt after ADT		8.3	0.72
Pt–C before ADT	~20	26.5	0.78
Pt–C after ADT		22.6	0.76

The Pt–C and monometallic Pt catalysts were further subjected to ADT in the half-cell RDE system consisting of 2000 CV cycles from 0.05 to 1 V_{RHE}, with 500 mV s^{-1} scan rate in N_2-saturated 0.5 M H_2SO_4 solution. The CVs recorded before (1st CV) and after ADT (2000th CV) for both the reference monometallic Pt and Pt–C catalysts are presented in Fig. 3.30a and b, respectively. In turn, the comparison of the ORR polarization curves recorded before and after ADT can be found in Fig. 3.30c. The ECSA, calculated from the corresponding CVs, was employed to investigate the impact of ADT on the morphology of the investigated catalysts, while the half-wave potential, calculated from the corresponding ORR polarization curves, was used to assess the impact of ADT on the activity of the investigated catalysts. All relevant values are summarized in Table 3.7.

The quantified ECSA loss during the entire ADT procedure was measured to be 21 % for monometallic Pt and 15 % for the Pt–C catalyst, suggesting a slightly higher stability of the latter. Notably, even after ADT, the ECSA of the Pt–C catalyst remains more than two times higher than that for Pt measured before ADT. Regarding ORR activity, the $E_{1/2}$ of Pt–C and monometallic Pt decrease by 26 and 25 mV, respectively. Nevertheless, the $E_{1/2}$ of Pt–C after ADT procedure remains about 10 mV higher than for Pt measured before ADT.

The Pt–C sample was further characterized after ADT to assess potential morphological, chemical, and structural changes induced by the testing. SEM and HRTEM cross-section images, presented in Fig. 3.31a and b, respectively, reveal that the Pt–C catalyst exhibits no significant changes in morphology after ADT compared to its pre-ADT state.

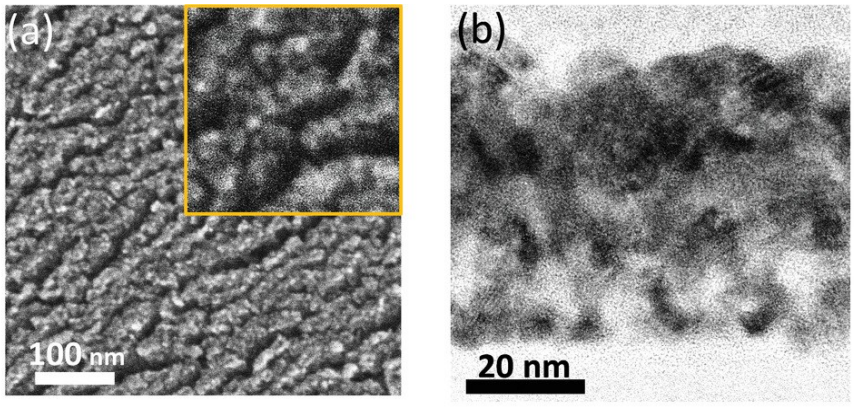

Fig. 3.31. *(a) SEM image (inset: enlarged SEM image) and (b) cross-section HRTEM image of Pt–C catalyst after ADT.*

The post-ADT Pt–C catalyst was then characterized with XRD. The diffraction pattern presented in Fig. 3.32a reveals only one phase of fcc Pt (space group Fm−3m), as all cerium oxide was already leached during the activation procedure. The Pt crystallite size calculated from the corresponding diffraction pattern was 5.68 ± 0.08 nm, which is slightly higher than the one measured from the deposited catalyst layer (4.78 ± 0.16 nm). The observed increase in the average nanoparticle size, which was not discernible with more localized SEM and HRTEM techniques, indicates catalyst coarsening during ADT. According to the literature, this phenomenon is usually associated with coalescence and/or Ostwald ripening processes, contributing to a slight decrease in the ECSA and the activity of the Pt–C catalyst after ADT [56].

The Pt–C catalyst after ADT was further characterized using the XPS technique. As expected, no ceria signal was detected in the Ce 3d spectrum, as shown in Fig. 3.32b. The Pt 4f core-level spectrum in Fig. 3.32c contained mostly metallic contribution at 71.3/74.6 eV. Nevertheless, a small doublet at 72.1/75.4 eV was observed, denoted to $Pt^{\delta+}$ states. This oxidation state slightly differs from Pt^{2+} in an as-deposited catalyst (72.5/75.8 eV) and might be attributed to Pt alloyed with carbon [166] or partially oxidized Pt due to sample exposure to air. The latter case seems to be most probable, as we did not observe any contribution from metal carbides in the C 1s spectra at 281-283 eV (see Fig. 3.30d).

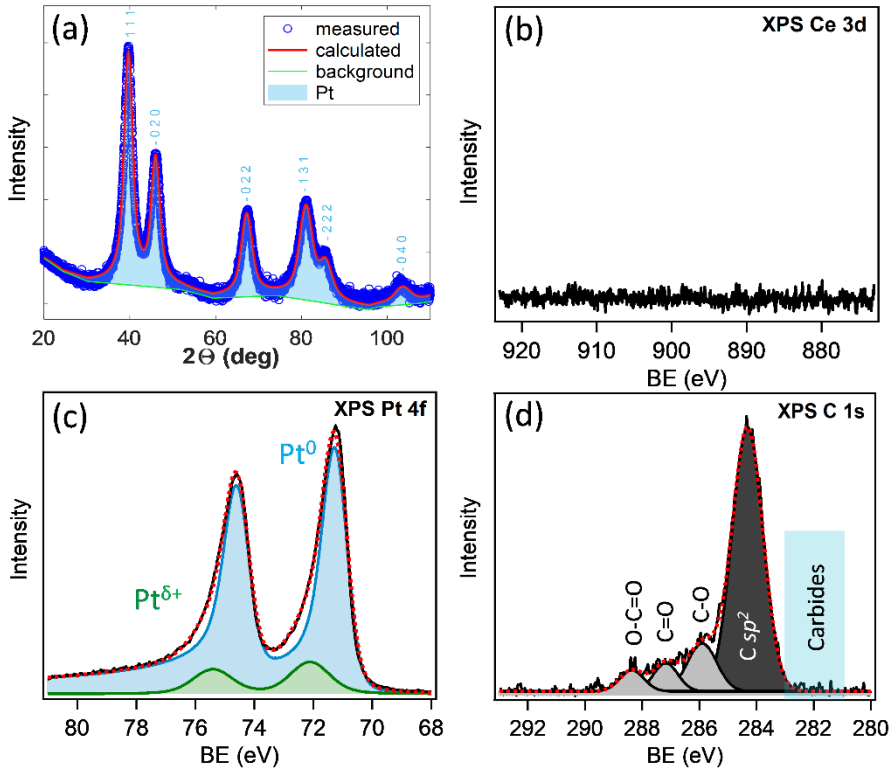

Fig. 3.32. *(a) Measured (blue circles) and fitted (red line) XRD diffractogram; (b) XPS Ce 3d spectrum; (c) XPS Pt 4f spectrum and (d) XPS C 1s spectrum of the Pt–C catalyst after ADT.*

3.3.5. Activity and stability of Pt–C catalyst in PEMFC

The Pt–C and monometallic Pt catalysts were further tested in a single-cell configuration. For testing in a real fuel cell device, the layers were deposited onto a commercial nGDL electrode. The nGDL with the deposited catalyst layer was used as the cathode part, while a commercial catalyst with Pt loading of 0.3 mg cm^{-2} was used as the anode part of the PEMFC device. It is anticipated that similar to the electrochemical activation in the half-cell, all CeO_x will be leached away during the single-cell break-in procedure. Polarization curves, along with the power density characteristics of such a single cell, are presented in Fig. 3.33 and compared with those for a magnetron-sputtered monometallic Pt cathode containing an identical amount of Pt. Fig. 3.33 also includes polarization curves and power density characteristics of such a single cell after accelerated durability testing (ADT), consisting of 4000 voltage sweeps at a 500 mV s^{-1} scan rate from 0.05 to 1.0 V_{RHE}.

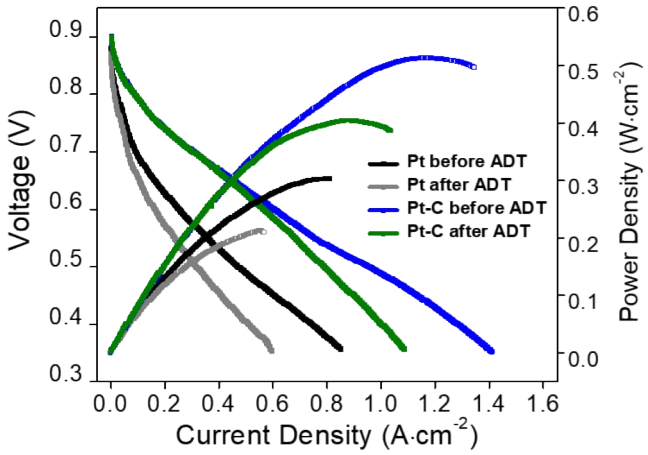

Fig. 3.33. *Polarization curves (left Y-axis), together with power density characteristics (right Y-axis) of the monometallic Pt and Pt–C catalysts as cathode at 80 °C with fully humidified H_2 and O_2 measured before and after ADTs.*

Table. 3.8. *Electrochemical parameters retrieved from the single-cell measurements.*

Sample	Current density at 0.65 V (A cm^{-2})	Maximum power density (W cm^{-2})
Pt before ADT	0.16	0.31
Pt after ADT	0.10	0.21
Pt–C before ADT	0.45	0.51
Pt–C after ADT	0.44	0.40

The results show that the maximum power density measured for Pt–C is two times higher than for monometallic Pt before ADT. Moreover, the power density loss of the Pt–C catalyst during the entire ADT process reached 22 %, while monometallic Pt lost 32 % of its initial activity. The current density at 0.65 V cell voltage was chosen for further comparison of the activity of the investigated catalysts. As shown in Table 3.8, the Pt–C catalyst demonstrated good stability with only a 3 % loss in the current density during ADT, while the monometallic Pt suffered from a 36 % loss in the current density. Overall, the results obtained in a single-cell configuration are very similar to the half-cell measurement.

3.3.6. Conclusions

In this chapter, we presented the concept of selective dealloying for the synthesis of a novel class of electrocatalysts for ORR. Specifically, a highly efficient Pt–C catalyst layer was derived from the electrochemical leaching of CeO_2 from a Pt–C–CeO_x ternary compound initially fabricated through simultaneous magnetron sputtering of Pt, C, and CeO_2.

The rapid leaching of CeO_2 during the electrochemical activation procedure consisting of voltammetric cycling in acidic electrolyte led to the formation of the carbon-stabilized highly porous Pt catalyst. The catalyst demonstrated an approximately threefold increase in electrochemically active surface area compared to monometallic Pt with identical loading. Moreover, it also exhibited enhanced activity and increased stability in the half-cell configuration. Specifically, the $E_{1/2}$ for Pt–C is shifted by nearly 30 mV towards higher potentials compared to that of monometallic Pt. During ADT, the quantified ECSA loss was measured to be 21% for monometallic Pt and 15% for the Pt–C catalyst. Notably, despite comparable ORR activity and ECSA loss during ADT, Pt–C maintained more than two times higher ECSA and about 10 mV higher $E_{1/2}$ than Pt measured even before ADT.

Lastly, the activity and stability of the Pt–C catalyst were investigated in a single cell. Overall, the results in single cell were comparable with those obtained in a half-cell. Specifically, when employed as the cathode catalyst in the PEMFC device, the Pt–C displayed three times higher maximum power density than monometallic Pt both before and after the degradation test.

4. Summary

This thesis presents a comprehensive investigation into the development, characterization and performance of advanced ORR catalysts prepared by magnetron sputtering with the aim of enhancing the cost-efficiency and stability of PEMFCs cathode catalyst. Significant progress has been made through systematic investigations of composition-activity-stability relationship of bimetallic Pt–Au and ternary PtNi–Au alloy catalysts, as well as the highly porous Pt–C catalysts prepared by electrochemical dealloying of Pt–C–CeO_x layer.

In the first chapter, Pt–Au catalysts with tailored composition (5, 10 and 20 at.% of Au) were investigated to determine the optimal balance between catalyst ORR activity and stability. Based on the electrochemical properties tested using RDE and SFC-ICP-MS techniques in a half-cell configuration, it was observed that Au had a detrimental effect on the activity of Pt but significantly suppressed its dissolution, thereby contributing to increased stability. Among tested samples, PtAu10 emerged as the most promising one, as it retains the activity of monometallic Pt while effectively suppressing Pt dissolution. Despite PtAu20 catalyst exhibited even better stability, its reduced ORR activity poses limitations for practical applications. The results were supported by multiple surface and bulk characterization techniques as well as computational modeling, which helped to gain better understanding of the above composition-activity-stability behaviour of Pt–Au alloy catalysts.

Pt–Au alloy catalysts were further tested during ADT comprising 500 potentiodynamic cycles to various upper potentials (1 V_{RHE}, 1.2 V_{RHE}, and 1.5 V_{RHE}), which aimed to simulate the diverse operational conditions of PEMFCs. The obtained results confirmed the stabilization of Pt catalyst caused by Au doping. Nevertheless, like any multimetallic system, the Pt–Au alloy exhibited surface compositional changes. Specifically, cycling to 1 V_{RHE} and 1.2 V_{RHE} resulted in surface enrichment of Au, while cycling to 1.5 V_{RHE} manifested in Pt enrichment, impacting Pt–Au activity during long-term operation. This behaviour however requires further investigation as it remains unclear whether these compositional changes are caused by preferential dissolution or surface segregation processes.

In the second chapter, the results obtained in the first chapter were applied to further enhance the activity and stability of the ORR catalyst. Specifically, Au doping was utilized to increase the activity-to-stability ratio of the PtNi catalyst, which is

known to be more active but less stable than monometallic Pt. The ternary PtNi–Au alloys with tailored compositions (3, 7 and 15 at.% of Au, Pt:Ni = 50:50) were investigated to determine the optimal balance between catalyst ORR activity and stability. The results showed that the dissolution of both Pt and Ni slows down as a function of Au concentration. At the same time ORR activity decreased. The PtNiAu15 sample exhibited the most stable composition, while its activity, although lower than that of PtNi, was still approximately three times higher than that of monometallic Pt.

In the third chapter, we presented the concept of selective dealloying of the Pt–C–CeO_x ternary compound prepared by magnetron sputtering for the synthesis of a highly porous Pt–C catalysts for ORR. Our findings revealed that following the electrochemical activation procedure, all CeO_x was leached from the Pt–C–CeO_x compound, and the remaining Pt–C catalysts exhibited superior ORR activity and enhanced stability compared to monometallic Pt.

Overall, the investigations described in the thesis reinforce the complexity of multielement alloy catalyst design, emphasizing the importance of understanding its composition-activity-stability relationship for providing valuable insights for future novel catalyst design strategies. Our findings contribute to the ongoing efforts aimed at enhancing the stability of ORR catalysts while increasing or at least maintaining their cost-efficiency which is crucial for the advancement of fuel cell technology toward sustainable energy solutions.

References

[1] C. Roman-Palacios and J. J. Wiens, Recent responses to climate change reveal the drivers of species extinction and survival. *Proc Natl Acad Sci USA,* **117**, 2020, 4211-4217.

[2] L. J. Gregor Erbach, Fit for 55 package. *European Council,* 2022. Available: https://www.europarl.europa.eu/RegData/etudes/BRIE/2022/733513/EPRS_BRI(2022)733513_EN.pdf

[3] I. Staffell, D. Scamman, A. V. Abad *et al.*, The role of hydrogen and fuel cells in the global energy system. *Energy Environ Sci,* **12**, 2019, 463-491.

[4] Z. Wang, Z. Liu, L. Fan *et al.*, Application progress of small-scale proton exchange membrane fuel cell. *Energy Rev,* **2**, 2023, 100017.

[5] B. Wu, M. Matian, and G. J. Offer, Hydrogen PEMFC system for automotive applications. *Int J Low-Carbon Technol,* **7**, 2012, 28-37.

[6] Y. Wang, D. F. R. Diaz, K. S. Chen *et al.*, Materials, technological status, and fundamentals of PEM fuel cells - A review. *Mater Today,* **32**, 2020, 178-203.

[7] J. H. Wee, Applications of proton exchange membrane fuel cell systems. *Renew Sust Energ Rev,* **11**, 2007, 1720-1738.

[8] B. P. Systems, Ballard's hydrogen fuel cells provide flexible, modular and highly reliable products for stationary power generation and backup applications. *Ballard,* 2023. Available: https://www.ballard.com/fuel-cell-solutions/fuel-cell-power-products/backup-power-systems

[9] Air-cooled fuel cell. *Horizon Fuel Cell Technologies,* 2023. Available: https://www.horizonfuelcell.com/%E5%89%AF%E6%9C%AC-fuel-cell-systems

[10] T. Wilberforce, A. Alaswad, A. Palumbo *et al.*, Advances in stationary and portable fuel cell applications. *Int J Hydrogen Energy,* **41**, 2016, 16509-16522.

[11] S. Hardman and G. Tal, Who are the early adopters of fuel cell vehicles?. *Int J Hydrogen Energy,* **43**, 2018, 17857-17866.

[12] B. G. Pollet, S. S. Kocha, and I. Staffell, Current status of automotive fuel cells for sustainable transport. *Curr Opin Electrochem,* **16**, 2019, 90-95.

[13] T. Yoshida and K. Kojima, Toyota MIRAI Fuel Cell Vehicle and Progress Toward a Future Hydrogen Society. *Electrochem Soc Interface,* **24**, 2015, 45-49.

[14] The world's 1st hydrogen powered passenger train. *Alstom Coradia iLint,* 2018. Available: https://www.alstom.com/solutions/rolling-stock/alstom-coradia-ilint-worlds-1st-hydrogen-powered-passenger-train

[15] B. James, J. Huya-Kouadio, C. Houchins *et al.*, Mass Production Cost Estimation of Direct H_2 PEM Fuel Cell Systems for Transportation Applications: 2018 Update. *U.S. Department of Energy,* Arlington VA, 2018.

[16] R. C. Samsun, L. Antoni, M. Rex *et al.*, Deployment Status of Fuel Cells in Road Transport: 2021. *V. Forschungszentrum Jülich GmbH Zentralbibliothek,* Jülich, 2021. Available: https://juser.fz-juelich.de/record/894093

[17] G. Reverdiau, A. Le Duigou, T. Alleau *et al.*, Will there be enough platinum for a large deployment of fuel cell electric vehicles?. *Int J Hydrogen Energy,* **46**, 2021, 39195-39207.

[18] Mineral commodity summaries 2022. *United States Geological Survey,* Reston, VA, 2022. Available: https://pubs.usgs.gov/publication/mcs2022

[19] U. D. Partnership, Fuel Cell Technical Team Roadmap. *U.S. Department of Energy,* 2017. Available: https://www.energy.gov/sites/default/files/2017/11/f46/FCTT_Roadmap_Nov_2017_FINAL.pdf

[20] H. A. Gasteiger, S. S. Kocha, B. Sompalli *et al.*, Activity benchmarks and requirements for Pt, Pt-alloy, and non-Pt oxygen reduction catalysts for PEMFCs. *Appl Catal B,* **56**, 2005, 9-35.

[21] J. K. Norskov, J. Rossmeisl, A. Logadottir *et al.*, Origin of the overpotential for oxygen reduction at a fuel-cell cathode. *J Phys Chem B,* **108**, 2004, 17886-17892.

[22] A. Kongkanand and M. F. Mathias, The Priority and Challenge of High-Power Performance of Low-Platinum Proton-Exchange Membrane Fuel Cells. *J Phys Chem Lett,* **7**, 2016, 1127-1137.

[23] O. Gröger, H. A. Gasteiger, and J.-P. Suchsland, Review—Electromobility: Batteries or Fuel Cells?. *J Electrochem Soc,* **162**, 2015, A2605.

[24] S. C. Liu, S. Y. Hua, R. Lin *et al.*, Improving the performance and durability of low Pt-loaded MEAs by adjusting the distribution positions of Pt particles in cathode catalyst layer. *Energy,* **253**, 2022, 124201.

[25] P. Gazdzicki, J. Mitzel, A. M. Dreizler *et al.*, Impact of Platinum Loading on Performance and Degradation of Polymer Electrolyte Fuel Cell Electrodes Studied in a Rainbow Stack. *Fuel Cells,* **18**, 2018, 270-278.

[26] J. C. Meier, C. Galeano, I. Katsounaros *et al.*, Degradation Mechanisms of Pt/C Fuel Cell Catalysts under Simulated Start-Stop Conditions. *ACS Catal,* **2**, 2012, 832-843.

[27] M. K. Debe, Electrocatalyst approaches and challenges for automotive fuel cells. *Nature,* **486**, 2012, 43-51.

[28] P. Lang, N. N. Yuan, Q. Q. Jiang *et al.*, Recent Advances and Prospects of Metal-Based Catalysts for Oxygen Reduction Reaction. *Energy Technol,* **8**, 2020, 1900984.

[29] R. G. Ma, G. X. Lin, Y. Zhou *et al.*, A review of oxygen reduction mechanisms for metal-free carbon-based electrocatalysts. *Npj Comput Mater,* **5**, 2019, 2102261.

[30] A. M. Gomez-Marin, J. M. Feliu, and E. Ticianelli, Oxygen Reduction on Platinum Surfaces in Acid Media: Experimental Evidence of a CECE/DISP Initial Reaction Path. *ACS Catal,* **9**, 2019, 2238-2251.

[31] X. M. Zhang, Z. Z. L. Xia, Y. Z. Huang *et al.*, Shape-Controlled Synthesis of Pt Nanopeanuts. *Sci Rep,* **6**, 2016, 31404.

[32] M. Nesselberger, S. Ashton, J. C. Meier *et al.*, The Particle Size Effect on the Oxygen Reduction Reaction Activity of Pt Catalysts: Influence of Electrolyte and Relation to Single Crystal Models. *J Am Chem Soc,* **133**, 2011, 17428-17433.

[33] S. P. Lin, K. W. Wang, C. W. Liu *et al.*, Trends of Oxygen Reduction Reaction on Platinum Alloys: A Computational and Experimental Study. *J Phys Chem C,* **119**, 2015, 15224-15231.

[34] Y. J. Wang, N. N. Zhao, B. Z. Fang *et al.*, Carbon-Supported Pt-Based Alloy Electrocatalysts for the Oxygen Reduction Reaction in Polymer Electrolyte Membrane Fuel Cells: Particle Size, Shape, and Composition Manipulation and Their Impact to Activity. *Chem Rev,* **115**, 2015, 3433-3467.

[35] J. K. Norskov, F. Abild-Pedersen, F. Studt *et al.*, Density functional theory in surface chemistry and catalysis. *Proc Natl Acad Sci USA,* **108**, 2011, 937-943.

[36] X. B. Yang, Y. Y. Wang, X. L. Tong *et al.*, Strain Engineering in Electrocatalysts: Fundamentals, Progress, and Perspectives. *Adv Energy Mater,* **12**, 2022.

[37] J. Greeley, I. E. L. Stephens, A. S. Bondarenko *et al.*, Alloys of platinum and early transition metals as oxygen reduction electrocatalysts. *Nat Chem,* **1**, 2009, 552-556.

[38] V. R. Stamenkovic, B. Fowler, B. S. Mun *et al.*, Improved oxygen reduction activity on $Pt_3Ni(111)$ via increased surface site availability. *Science,* **315**, 2007, 493-497.

[39] M. H. Xie, Z. H. Lyu, R. H. Chen *et al.*, Pt-Co@Pt Octahedral Nanocrystals: Enhancing Their Activity and Durability toward Oxygen Reduction with an Intermetallic Core and an Ultrathin Shell. *J Am Chem Soc,* **143**, 2021, 8509-8518.

[40] Z. Y. Li, R. Zeng, L. G. Wang *et al.*, A simple strategy to form hollow Pt_3Co alloy nanosphere with ultrathin Pt shell with significant enhanced oxygen reduction reaction activity. *Int J Hydrogen Energy,* **41**, 2016, 21394-21403.

[41] C. Wang, H. Daimon, Y. Lee *et al.*, Synthesis of monodisperse Pt nanocubes and their enhanced catalysis for oxygen reduction. *J Am Chem Soc,* **129**, 2007, 6974-6975.

[42] M. F. Li, Z. P. Zhao, T. Cheng *et al.*, Ultrafine jagged platinum nanowires enable ultrahigh mass activity for the oxygen reduction reaction. *Science,* **354**, 2016, 1414-419.

[43] G. Y. Shi, T. Tano, D. A. A. Tryk *et al.*, Pt nanorods oriented on Gd-doped ceria polyhedra enable superior oxygen reduction catalysis for fuel cells. *J Catal,* **407**, 2022, 300-311.

[44] X. L. Tian, X. Zhao, Y. Q. Su *et al.*, Engineering bunched Pt-Ni alloy nanocages for efficient oxygen reduction in practical fuel cells. *Science,* **366**, 2019, 850-856.

[45] L. Z. Bu, N. Zhang, S. J. Guo *et al.*, Biaxially strained PtPb/Pt core/shell nanoplate boosts oxygen reduction catalysis. *Science,* **354**, 2016, 1410-1414.

[46] J. J. Zhao, Z. K. Tu, and S. H. Chan, Carbon corrosion mechanism and mitigation strategies in a proton exchange membrane fuel cell (PEMFC): A review. *J Power Sources,* **488**, 2021, 229434.

[47] R. Makharia, S. Kocha, P. Yu *et al.*, Durable PEM Fuel Cell Electrode Materials: Requirements and Benchmarking Methodologies. *ECS Trans,* **1**, 2006, 3.

[48] J. Sim, M. Kang, K. Min *et al.*, Effects of carbon corrosion on proton exchange membrane fuel cell performance using two durability evaluation methods. *Renewable Energy,* **190**, 2022, 959-970.

[49] G. W. Murphy, Pourbaix,M - Atlas of Electrochemical Equilibria in Aqueous Solutions. *Science,* **154**, 1966, 1537.

[50] H. Imai, K. Izumi, M. Matsumoto *et al.*, In Situ and Real-Time Monitoring of Oxide Growth in a Few Monolayers at Surfaces of Platinum Nanoparticles in Aqueous Media. *J Am Chem Soc,* **131**, 2009, 6293-6300.

[51] Z. H. Gu and P. B. Balbuena, Absorption of atomic oxygen into subsurfaces of Pt(100) and Pt(111): Density functional theory study. *J Phys Chem C,* **111**, 2007, 9877-9883.

[52] Z. H. Gu and P. B. Balbuena, Chemical environment effects on the atomic oxygen absorption into Pt(111) subsurfaces. *J Phys Chem C,* **111**, 2007, 17388-17396.

[53] J. Nikolic, E. Exposito, J. Iniesta *et al.*, Theoretical concepts and applications of a rotating disk electrode. *J Chem Educ,* **77**, 2000, 1191-1194.

[54] A. A. Topalov, S. Cherevko, A. R. Zeradjanin *et al.*, Towards a comprehensive understanding of platinum dissolution in acidic media. *Chem Sci,* **5**, 2014, 631-638.

[55] J. C. Meier, C. Galeano, I. Katsounaros *et al.*, Design criteria for stable Pt/C fuel cell catalysts. *Beilstein J Nanotechnol,* **5**, 2014, 44-67.

[56] S. Cherevko, N. Kulyk, and K. J. J. Mayrhofer, Durability of platinum-based fuel cell electrocatalysts: Dissolution of bulk and nanoscale platinum. *Nano Energy,* **29**, 2016, 275-298.

[57] A. C. C. Tseung and S. C. Dhara, Loss of Surface-Area by Platinum and Supported Platinum Black Electrocatalyst. *Electrochim Acta,* **20**, 1975, 681-683.

[58] U.S. DRIVE Fuel Cell Tech Team Cell Component Accelerated Stress Test and Polarization Curve Protocols for PEM Fuel Cells. *U.S. Department of Energy,* 2013. Available: https://www.energy.gov/eere/fuelcells/articles/fuel-cell-tech-team-accelerated-stress-test-and-polarization-curve

[59] M. Lukaszewski, M. Soszko, and A. Czerwinski, Electrochemical Methods of Real Surface Area Determination of Noble Metal Electrodes - an Overview. *Int J Electrochem Sci,* **11**, 2016, 4442-4469.

[60] Y. J. Li, Y. J. Li, E. B. Zhu *et al.*, Stabilization of High-Performance Oxygen Reduction Reaction Pt Electrocatalyst Supported on Reduced Graphene Oxide/Carbon Black Composite. *J Am Chem Soc,* **134**, 2012, 12326-12329.

[61] M. Vorokhta, I. Khalakhan, I. Matolinova *et al.*, Nanostructured Pt-CeO_2 thin film catalyst grown on graphite foil by magnetron sputtering. *Appl Surf Sci,* **267**, 2013, 119-123.

[62] A. Kongkanand, S. Kuwabata, G. Girishkumar *et al.*, Single-wall carbon nanotubes supported platinum nanoparticles with improved electrocatalytic activity for oxygen reduction reaction. *Langmuir,* **22**, 2006, 2392-2396.

[63] X. X. Wang, Z. H. Tan, M. Zeng *et al.*, Carbon nanocages: A new support material for Pt catalyst with remarkably high durability. *Sci Rep,* **4**, 2014, 4437.

[64] M. Karuppannan, Y. Kim, S. Gok *et al.*, A highly durable carbon-nanofiber-supported Pt-C core-shell cathode catalyst for ultra-low Pt loading proton exchange membrane fuel cells: facile carbon encapsulation. *Energy Environ Sci,* **12**, 2019, 2820-2829.

[65] W. J. Lee, S. Bera, H. Woo *et al.*, In Situ Engineering of a Metal Oxide Protective Layer into Pt/Carbon Fuel-Cell Catalysts by Atomic Layer Deposition. *Chem Mater,* 2022, 5949-5959.

[66] C. Li, N. C. S. Selvam, and J. Y. Fang, Shape-Controlled Synthesis of Platinum-Based Nanocrystals and Their Electrocatalytic Applications in Fuel Cells. *Nano Micro Lett,* **15**, 2023, 83.

[67] J. W. Zhang, Y. L. Yuan, L. Gao *et al.*, Stabilizing Pt-Based Electrocatalysts for Oxygen Reduction Reaction: Fundamental Understanding and Design Strategies. *Adv Mater,* **33**, 2021, 2006494.

[68] Z. An, H. Q. Li, X. M. Zhang *et al.*, Structural Evolution of a PtRh Nanodendrite Electrocatalyst and Its Ultrahigh Durability toward Oxygen Reduction Reaction. *ACS Catal,* **12**, 2022, 3302-3308.

[69] Y. Z. Lu, Y. Y. Jiang, and W. Chen, PtPd porous nanorods with enhanced electrocatalytic activity and durability for oxygen reduction reaction. *Nano Energy,* **2**, 2013, 836-844.

[70] P. P. Lopes, D. G. Li, H. F. Lv *et al.*, Eliminating dissolution of platinum-based electrocatalysts at the atomic scale. *Nat Mater,* **19**, 2020, 1207-1214.

[71] J. Zhang, K. Sasaki, E. Sutter *et al.*, Stabilization of platinum oxygen-reduction electrocatalysts using gold clusters. *Science,* **315**, 2007, 220-222.

[72] V. Beermann, M. Gocyla, E. Willinger *et al.*, Rh-Doped Pt-Ni Octahedral Nanoparticles: Understanding the Correlation between Elemental Distribution, Oxygen Reduction Reaction, and Shape Stability. *Nano Lett,* **16**, 2016, 1719-1725.

[73] F. Liu, K. Sun, Z. Y. Rui *et al.*, Highly Durable and Active Ternary Pt-Au-Ni Electrocatalyst for Oxygen Reduction Reaction. *Chemcatchem,* **10**, 2018, 3049-3056.

[74] X. Wang, L. J. Zhang, H. Y. Gong *et al.*, Dealloyed PtAuCu electrocatalyst to improve the activity and stability towards both oxygen reduction and methanol oxidation reactions. *Electrochim Acta,* **212**, 2016, 277-285.

[75] M. P. Seah and W. A. Dench, Quantitative electron spectroscopy of surfaces: A standard data base for electron inelastic mean free paths in solids. *Surf Interface Anal,* **1**, 1979, 2-11.

[76] C. D. Wagner, L. E. Davis, M. V. Zeller *et al.*, Empirical Atomic Sensitivity Factors for Quantitative-Analysis by Electron-Spectroscopy for Chemical-Analysis. *Surf Interface Anal,* **3**, 1981, 211-225.

[77] J. Wang, C. X. Zhao, J. N. Liu *et al.*, Quantitative kinetic analysis on oxygen reduction reaction: A perspective. *Nano Materials Science,* **3**, 2021, 313-318.

[78] Single cell test protocol. *US Full Cell Council,* Washington, D.C, 2006. Available:http://www.members.fchea.org/core/import/PDFs/Technical%20Resources/MatComp%20Single%20Cell%20Test%20Protocol%2005-014RevB.2%20071306.pdf

[79] S. Cherevko and K. J. J. Mayrhofer, On-Line Inductively Coupled Plasma Spectrometry in Electrochemistry: Basic Principles and Applications. *Elsevier,* Oxford, 2018, 326-335. ISBN 978-0-12-809894-3.

[80] O. Kasian, S. Geiger, K. J. J. Mayrhofer *et al.*, Electrochemical On-line ICP-MS in Electrocatalysis Research. *Chemical Record,* **19**, 2019, 2130-2142.

[81] S. Takahashi, H. Chiba, T. Kato *et al.*, Oxygen reduction reaction activity and structural stability of Pt-Au nanoparticles prepared by arc-plasma deposition. *PCCP,* **17**, 2015, 18638-18644.

[82] S. Cherevko, G. P. Keeley, N. Kulyk *et al.*, Pt Sub-Monolayer on Au: System Stability and Insights into Platinum Electrochemical Dissolution. *J Electrochem Soc,* **163**, 2016, I1228-I1233.

[83] J. Luo, M. M. Maye, V. Petkov *et al.*, Phase properties of carbon-supported gold-platinum nanoparticles with different bimetallic compositions. *Chem Mater,* **17**, 2005, 3086-3091.

[84] M. J. Prieto, E. A. Carbonio, R. Landers *et al.*, Promotion Effect of Platinum on Gold's Reactivity: A High-Resolution Photoelectron Spectroscopy Study. *J Phys Chem C,* **120**, 2016, 10227-10236.

[85] P. Heimann, J. F. Vanderveen, and D. E. Eastman, Structure-Dependent Surface Core Level Shifts for the Au(111), (100), and (110) Surfaces. *Solid State Commun,* **38**, 1981, 595-598.

[86] D. N. Wang, X. Y. Cui, Q. F. Xiao *et al.*, Electronic behaviour of Au-Pt alloys and the 4f binding energy shift anomaly in Au bimetallics- X-ray spectroscopy studies. *Aip Advances,* **8**, 2018, 065210.

[87] F. F. Ren, C. Y. Zhai, M. S. Zhu *et al.*, Facile synthesis of PtAu nanoparticles supported on polydopamine reduced and modified graphene oxide as a highly active catalyst for methanol oxidation. *Electrochim Acta,* **153**, 2015, 175-183.

[88] W. J. Zhou, M. Li, L. Zhang *et al.*, Supported PtAu catalysts with different nano-structures for ethanol electrooxidation. *Electrochim Acta,* **123**, 2014, 233-239.

[89] D. Tongsakul, S. Nishimura, and K. Ebitani, Platinum/Gold Alloy Nanoparticles-Supported Hydrotalcite Catalyst for Selective Aerobic Oxidation of Polyols in Base-Free Aqueous Solution at Room Temperature. *ACS Catal,* **3**, 2013, 2199-2207.

[90] W. P. Davey, Precision Measurements of the Lattice Constants of Twelve Common Metals. *Phys Rev,* **25**, 1925, 753-761.

[91] N. C. Röttcher, Y. P. Ku, M. Minichova *et al.*, Comparison of methods to determine electrocatalysts' surface area in gas diffusion electrode setups: a case study on Pt/C and PtRu/C. *JPhys Energy,* **5**, 2023, 024007.

[92] S. Rudi, C. H. Cui, L. Gan *et al.*, Comparative Study of the Electrocatalytically Active Surface Areas (ECSAs) of Pt Alloy Nanoparticles Evaluated by H and CO-stripping voltammetry. *Electrocatalysis,* **5**, 2014, 408-418.

[93] S. Yang and H. Lee, Atomically Dispersed Platinum on Gold Nano-Octahedra with High Catalytic Activity on Formic Acid Oxidation. *ACS Catal,* **3**, 2013, 437-443.

[94] I. J. McPherson, P. A. Ash, L. Jones *et al.*, Electrochemical CO Oxidation at Platinum on Carbon Studied through Analysis of Anomalous in Situ IR Spectra. *J Phys Chem C Nanomater Interfaces,* **121**, 2017, 17176-17187.

[95] P. Urchaga, S. Baranton, C. Coutanceau *et al.*, Electro-oxidation of CO(chem) on Pt nanosurfaces: solution of the peak multiplicity puzzle. *Langmuir,* **28**, 2012, 3658-63.

[96] S. Brimaud, S. Pronier, C. Coutanceau *et al.*, New findings on CO electrooxidation at platinum nanoparticle surfaces. *Electrochem Commun,* **10**, 2008, 1703-1707.

[97] S. Brimaud, Z. Jusys, and R. J. Behm, Shape-selected nanocrystals for in situ spectro-electrochemistry studies on structurally well defined surfaces under controlled electrolyte transport: A combined in situ ATR-FTIR/online DEMS investigation of CO electrooxidation on Pt. *Beilstein J Nanotechnol,* **5**, 2014, 735-46.

[98] M. Arenz, K. J. J. Mayrhofer, V. Stamenkovic *et al.*, The Effect of the Particle Size on the Kinetics of CO Electrooxidation on High Surface Area Pt Catalysts. *J Am Chem Soc,* **127**, 2005, 6819-6829.

[99] Q. Zhang, R. Yue, F. Jiang *et al.*, Au as an efficient promoter for electrocatalytic oxidation of formic acid and carbon monoxide: a comparison between Pt-on-Au and PtAu alloy catalysts. *Gold Bulletin,* **46**, 2013, 175-184.

[100] B. C. Du and Y. Y. Tong, A coverage-dependent study of Pt spontaneously deposited onto Au and Ru surfaces: Direct experimental evidence of the ensemble effect for methanol electro-oxidation on Pt. *J Phys Chem B,* **109**, 2005, 17775-17780.

[101] D. J. S. Sandbeck, O. Brummel, K. J. J. Mayrhofer *et al.*, Dissolution of Platinum Single Crystals in Acidic Medium. *Chemphyschem,* **20**, 2019, 2997-3003.

[102] S. Cherevko, A. A. Topalov, I. Katsounaros *et al.*, Electrochemical dissolution of gold in acidic medium. *Electrochem Commun,* **28**, 2013, 44-46.

[103] M. Smiljanić, M. Bele, L. J. Moriau *et al.*, Suppressing Platinum Electrocatalyst Degradation via a High-Surface-Area Organic Matrix Support. *ACS Omega,* **7**, 2022, 3540-3548.

[104] Y. W. Ma, H. M. Zhang, H. X. Zhong *et al.*, High active PtAu/C catalyst with core-shell structure for oxygen reduction reaction. *Catal Commun,* **11**, 2010, 434-437.

[105] K. Kodama, R. Jinnouchi, N. Takahashi *et al.*, Activities and Stabilities of Au-Modified Stepped-Pt Single-Crystal Electrodes as Model Cathode Catalysts in Polymer Electrolyte Fuel Cells. *J Am Chem Soc,* **138**, 2016, 4194-4200.

[106] P. P. Lopes, D. Strmcnik, D. Tripkovic *et al.*, Relationships between Atomic Level Surface Structure and Stability/Activity of Platinum Surface Atoms in Aqueous Environments. *ACS Catal,* **6**, 2016, 2536-2544.

[107] S. M. Kozlov, G. Kovacs, R. Ferrando *et al.*, How to determine accurate chemical ordering in several nanometer large bimetallic crystallites from electronic structure calculations. *Chem Sci,* **6**, 2015, 3868-3880.

[108] G. Kovacs, S. M. Kozlov, and K. M. Neyman, Versatile Optimization of Chemical Ordering in Bimetallic Nanoparticles. *J Phys Chem C,* **121**, 2017, 10803-10808.

[109] N. Danielis, L. Vega, G. Fronzoni *et al.*, AgPd, AuPd, and AuPt Nanoalloys with Ag- or Au-Rich Compositions: Modeling Chemical Ordering and Optical Properties. *J Phys Chem C,* **125**, 2021, 17372-17384.

[110] A. Ostroverkh, M. Dubau, V. Johánek *et al.*, Efficient Pt-C MEA for PEMFC with Low Platinum Content Prepared by Magnetron Sputtering. *Fuel Cells,* **18**, 2018, 51-56.

[111] S. Cherevko, G. P. Keeley, S. Geiger *et al.*, Dissolution of Platinum in the Operational Range of Fuel Cells. *Chemelectrochem,* **2**, 2015, 1471-1478.

[112] T. Dukic, L. J. Moriau, L. Pavko *et al.*, Understanding the Crucial Significance of the Temperature and Potential Window on the Stability of Carbon Supported Pt-Alloy Nanoparticles as Oxygen Reduction Reaction Electrocatalysts. *ACS Catal,* **12**, 2022, 101-115.

[113] N. Hodnik, M. Zorko, B. Jozinović *et al.*, Severe accelerated degradation of PEMFC platinum catalyst: A thin film IL-SEM study. *Electrochem Commun,* **30**, 2013, 75-78.

[114] V. Papaefthimiou, M. Diebold, C. Ulhaq-Bouillet *et al.*, Potential-Induced Segregation Phenomena in Bimetallic PtAu Nanoparticles: An In Situ Near-Ambient-Pressure Photoelectron Spectroscopy Study. *Chemelectrochem,* **2**, 2015, 1519-1526.

[115] C.-E. Kim, D.-H. Lim, J. H. Jang *et al.*, Effect of gold subsurface layer on the surface activity and segregation in Pt/Au/Pt_3M (where M = 3d transition metals) alloy catalyst from first-principles. *J Chem Phys,* **142**, 2015, 034707.

[116] S. Zafeiratos, S. Piccinin, and D. Teschner, Alloys in catalysis: phase separation and surface segregation phenomena in response to the reactive environment. *Catal Sci Technol,* **2**, 2012, 1787-1801.

[117] L. Deng, W. Y. Hu, H. Q. Deng *et al.*, Surface Segregation and Structural Features of Bimetallic Au-Pt Nanoparticles. *J Phys Chem C,* **114**, 2010, 11026-11032.

[118] C. Y. Ahn, J. E. Park, S. Kim *et al.*, Differences in the Electrochemical Performance of Pt-Based Catalysts Used for Polymer Electrolyte Membrane Fuel Cells in Liquid Half- and Full-Cells. *Chem Rev,* **121**, 2021, 15075-15140.

[119] M. Gatalo, P. Jovanovic, G. Polymeros *et al.*, Positive Effect of Surface Doping with Au on the Stability of Pt-Based Electrocatalysts. *ACS Catal,* **6**, 2016, 1630-1634.

[120] Y. J. Kang, J. Snyder, M. F. Chi *et al.*, Multimetallic Core/Interlayer/Shell Nanostructures as Advanced Electrocatalysts. *Nano Lett,* **14**, 2014, 6361-6367.

[121] J. D. Cao, H. H. Cao, F. H. Wang *et al.*, Fully ordered L1-PtCoAu electrocatalyst derived from PtAu@CoO precursor with enhanced performance for oxygen reduction reaction. *Electrochim Acta,* **384**, 2021, 138266.

[122] L. M. Guo, D. F. Zhang, and L. Guo, Structure Design Reveals the Role of Au for ORR Catalytic Performance Optimization in PtCo-Based Catalysts. *Adv Funct Mater,* **30**, 2020, 2001575.

[123] I. Khalakhan, L. Vega, M. Vorokhta *et al.*, Irreversible structural dynamics on the surface of bimetallic PtNi alloy catalyst under alternating oxidizing and reducing environments. *Appl Catal B,* **264**, 2020, 118476.

[124] X. X. Xie, V. Briega-Martos, R. Farris *et al.*, Optimal Pt-Au Alloying for Efficient and Stable Oxygen Reduction Reaction Catalysts. *ACS Appl Mater Interfaces,* 2022, 1192-1200.

[125] X. X. Xie, A. L. M. Sandhya, L. Piliai *et al.*, Surface compositional dynamics in a PtNi bimetallic alloy under simulated operational conditions: Electrochemical and NAP-XPS Study. *Appl Catal B,* **325**, 2023, 122328.

[126] V. Stamenkovic, B. S. Mun, K. J. J. Mayrhofer *et al.*, Changing the activity of electrocatalysts for oxygen reduction by tuning the surface electronic structure. *Angew Chem Int Ed,* **45**, 2006, 2897-2901.

[127] M. X. Gong, Z. P. Deng, D. D. Xiao *et al.*, One-Nanometer-Thick PtNi Bimetallic Alloy Nanowires Advanced Oxygen Reduction Reaction: Integrating Multiple Advantages into One Catalyst. *ACS Catal,* **9**, 2019, 4488-4494.

[128] C. Lim, A. R. Fairhurst, B. J. Ransom *et al.*, Role of Transition Metals in Pt Alloy Catalysts for the Oxygen Reduction Reaction. *ACS Catal,* **13**, 2023, 14874-14893.

[129] V. R. Stamenkovic, B. S. Mun, K. J. J. Mayrhofer *et al.*, Effect of Surface Composition on Electronic Structure, Stability, and Electrocatalytic Properties of Pt-Transition Metal Alloys: Pt-Skin versus Pt-Skeleton Surfaces. *J Am Chem Soc,* **128**, 2006, 8813-8819.

[130] S. G. Bratsch, Standard Electrode Potentials and Temperature Coefficients in Water at 298.15 K. *J Phys Chem Ref Data,* **18**, 1989, 1-21.

[131] P. Mani, R. Srivastava, and P. Strasser, Dealloyed binary PtM_3 (M = Cu, Co, Ni) and ternary $PtNi_3M$ (M = Cu, Co, Fe, Cr) electrocatalysts for the oxygen reduction reaction: Performance in polymer electrolyte membrane fuel cells. *J Power Sources,* **196**, 2011, 666-673.

[132] L. Gan, M. Heggen, S. Rudi *et al.*, Core-Shell Compositional Fine Structures of Dealloyed PtNi Nanoparticles and Their Impact on Oxygen Reduction Catalysis. *Nano Lett,* **12**, 2012, 5423-5430.

[133] J. Gu, G. M. Zhang, R. Yao *et al.*, High Oxygen Reduction Activity of Pt-Ni Alloy Catalyst for Proton Exchange Membrane Fuel Cells. *Catalysts,* **12**, 2022, 250.

[134] I. Khalakhan, M. Bogar, M. Vorokhta *et al.*, Evolution of the PtNi Bimetallic Alloy Fuel Cell Catalyst under Simulated Operational Conditions. *ACS Appl Mater Interfaces,* **12**, 2020, 17602-17610.

[135] S. Cherevko, Electrochemical dissolution of noble metals native oxides. *J Electroanal Chem,* **787**, 2017, 11-13.

[136] F. Cao, R. Ding, Z. Y. Rui *et al.*, Advances in Low Pt Loading Membrane Electrode Assembly for Proton Exchange Membrane Fuel Cells. *Molecules,* **28**, 2023, 773.

[137] F. Iskandar, T. Iwaki, T. Toda *et al.*, High coercivity of ordered macroporous FePt films synthesized via colloidal templates. *Nano Lett,* **5**, 2005, 1525-1528.

[138] L. Chen and G. X. Lu, Hydrothermal synthesis of size-dependent Pt in Pt/MWCNTs nanocomposites for methanol electro-oxidation. *Electrochim Acta,* **53**, 2008, 4316-4323.

[139] R. J. Cui, L. Mei, G. J. Han *et al.*, Facile Synthesis of Nanoporous Pt-Y alloy with Enhanced Electrocatalytic Activity and Durability. *Sci Rep,* **7**, 2017, 41826.

[140] Z. Lu, C. Li, J. H. Han *et al.*, Three-dimensional bicontinuous nanoporous materials by vapor phase dealloying. *Nat Commun,* **9**, 2018, 276.

[141] B. H. Han, C. E. Carlton, A. Kongkanand *et al.*, Record activity and stability of dealloyed bimetallic catalysts for proton exchange membrane fuel cells. *Energy Environ Sci,* **8**, 2015, 258-266.

[142] J. Erlebacher, M. J. Aziz, A. Karma *et al.*, Evolution of nanoporosity in dealloying. *Nature,* **410**, 2001, 450-453.

[143] M. Oezaslan, M. Heggen, and P. Strasser, Size-Dependent Morphology of Dealloyed Bimetallic Catalysts: Linking the Nano to the Macro Scale. *J Am Chem Soc,* **134**, 2012, 514-524.

[144] L. Gan, C. H. Cui, S. Rudi *et al.*, Core-Shell and Nanoporous Particle Architectures and Their Effect on the Activity and Stability of Pt ORR Electrocatalysts. *Top Catal,* **57**, 2014, 236-244.

[145] M. Oezaslan and P. Strasser, Activity of dealloyed PtCo and PtCu nanoparticle electrocatalyst for oxygen reduction reaction in polymer electrolyte membrane fuel cell. *J Power Sources,* **196**, 2011, 5240-5249.

[146] A. A. Nechitaĭlov, T. K. Zvonareva, A. D. Remenyuk *et al.*, Catalytic properties of composite amorphous carbon-platinum layers in fuel cells. *Semiconductors,* **42**, 2008, 1249-1254.

[147] O. Alekseeva, A. Mikhalev, E. Lutikova *et al.*, Structural and Electrocatalytic Properties of Platinum and Platinum-Carbon Layers Obtained by Magnetron-Ion Sputtering. *Catalysts,* **8**, 2018, 665.

[148] D. Shin, M. Han, Y. G. Shul *et al.*, Analysis of cerium-composite polymer-electrolyte membranes during and after accelerated oxidative-stability test. *J Power Sources,* **378**, 2018, 468-474.

[149] M. Zaton, J. Rozière, and D. J. Jones, Current understanding of chemical degradation mechanisms of perfluorosulfonic acid membranes and their mitigation strategies: a review. *Sustain Energy Fuels,* **1**, 2017, 409-438.

[150] Y. Y. Chu, Z. B. Wang, Z. Z. Jiang *et al.*, A Novel Structural Design of a Pt/C-CeO Catalyst with Improved Performance for Methanol Electro-Oxidation by β-Cyclodextrin Carbonization. *Adv Mater,* **23**, 2011, 3100-3104.

[151] L. Feng, D. T. Hoang, C. K. Tsung *et al.*, Catalytic Properties of Pt Cluster-Decorated CeO Nanostructures. *Nano Res,* **4**, 2011, 61-71.

[152] K. Deori, D. Gupta, B. Saha *et al.*, Introducing nanocrystalline CeO_2 as heterogeneous environmental friendly catalyst for the aerobic oxidation of para-xylene to terephthalic acid in water. *J Mater Chem A,* **1**, 2013, 7091-7099.

[153] T. Y. Kardash, E. A. Derevyannikova, E. M. Slavinskaya *et al.*, Pt/CeO_2 and Pt/$CeSnO_x$ Catalysts for Low-Temperature CO Oxidation Prepared by Plasma-Arc Technique. *Front Chem,* **7**, 2019, 114.

[154] L. Li, M. K. Wang, N. Cui *et al.*, CeO_2 doped Pt/C as an efficient cathode catalyst for an air-cathode single-chamber microbial fuel cell. *RSC Adv,* **6**, 2016, 25877-25881.

[155] T. Skala, F. Sutara, K. C. Prince *et al.*, Cerium oxide stoichiometry alteration via Sn deposition: Influence of temperature. *J Electron Spectrosc Relat Phenom,* **169**, 2009, 20-25.

[156] J. F. Moulder, W. F. Stickle, P. E. Sobol *et al.*, Handbook of X-ray Photoelectron Spectroscopy *Perkin-Elmer Corporation Physical Electronics Division,* Minnesota 1981, ISBN 0-9627026-2-5.

[157] V. Matolín, I. Khalakhan, I. Matolínová *et al.*, Pt^{2+}, Pt^{4+} ions in CeO_2 rf-sputtered thin films. *Surf Interface Anal,* **42**, 2010, 882-885.

[158] A. Bruix, Y. Lykhach, I. Matolinova *et al.*, Maximum Noble-Metal Efficiency in Catalytic Materials: Atomically Dispersed Surface Platinum. *Angew Chem Int Ed,* **53**, 2014, 10525-10530.

[159] M. K. Rabchinskii, A. T. Dideikin, D. A. Kirilenko *et al.*, Facile reduction of graphene oxide suspensions and films using glass wafers. *Sci Rep,* **8**, 2018, 14154.

[160] A. Fujimoto, Y. Yamada, M. Koinuma *et al.*, Origins of sp^3C peaks in C_{1s} X-ray Photoelectron Spectra of Carbon Materials. *Anal Chem,* **88**, 2016, 6110-6114.

[161] E. Munoz-Sandoval, J. L. Fajardo-Diaz, R. Sanchez-Salas *et al.*, Two Sprayer CVD Synthesis of Nitrogen-doped Carbon Sponge-type Nanomaterials. *Sci Rep,* **8**, 2018, 2983.

[162] T. Duchoň, F. Dvořák, M. Aulická *et al.*, Ordered Phases of Reduced Ceria As Epitaxial Films on Cu(111). *J Phys Chem C,* **118**, 2013, 357-365.

[163] V. Johanek, M. Vaclavu, I. Matolinova *et al.*, High low-temperature CO oxidation activity of platinum oxide prepared by magnetron sputtering. *Appl Surf Sci,* **345**, 2015, 319-328.

[164] D. R. Mullins, P. M. Albrecht, T.-L. Chen *et al.*, Water Dissociation on CeO_2(100) and CeO_2(111) Thin Films. *J Phys Chem C,* **116**, 2012, 19419-19428.

[165] M. Peuckert and H. P. Bonzel, Characterization of Oxidized Platinum Surfaces by X-Ray Photoelectron-Spectroscopy. *Surf Sci,* **145**, 1984, 239-259.

[166] Y. Lou, H. L. Wu, and J. Y. Liu, Nanocarbon-Edge-Anchored High-Density Pt Atoms for 3-nitrostyrene Hydrogenation: Strong Metal-Carbon Interaction. *Iscience,* **13**, 2019, 190-198.

List of Figures

List of Tables

List of Abbreviations

GC	Glassy carbon
MC	Monte Carlo
SA	Specific activity
PD	Power density
MA	Mass activity
FCBs	Fuel cell buses
DC	Direct current
RF	Radiofrequency
FCV	Fuel cell vehicle
AFC	Alkaline fuel cells
SOFC	Solid oxide fuel cells
MFC	Microbial fuel cells
XRD	X-ray Diffraction
WE	Working electrode
CE	Counter electrode
SE	Secondary electrons
RE	Reference electrode
AE	Auger electrons
TOP	Topological method
CV	Cyclic voltammetry
FFT	Fourier transformation
FCC	Face-centered-cubic
GDL	Gas diffusion electrode
AFM	Atomic force microscopy
SEM	Scanning electron microscopy
PEM	Polymer electrolyte membrane
BSE	Backscattered electrons
UHV	Ultrahigh vacuum
RDE	Rotating disc electrode
RHE	Reversible hydrogen electrode
UPL	Upper potential limit

DFT	Density functional theory
ORR	Oxygen reduction reaction
ADT	Accelerated degradation test
MEA	Membrane electrode assembly
HOR	Hydrogen oxidation reaction
CHP	Combined heat and power
PES	Photoelectron spectroscopy
XPS	X-ray photoelectron spectroscopy
IMFP	Inelastic mean free path
RSFs	Relative sensitivity factors
H_{UPD}	Hydrogen underpotential deposition
ECSA	Electrochemically active surface area
PEMFC	Proton exchange membrane fuel cell
EDX	Energy-dispersive X-ray spectroscopy
GAXRD	Glancing angle X-ray diffraction
SRPES	Synchrotron radiation photoelectron spectroscopy
HRTEM	High-resolution transmission electron microscopy
SFC-ICP-MS	Scanning flow cell combined with inductively coupled mass spectrometer